

**Assembly and Application of an Instrument for**

**Attosecond-Time-Resolved  
Ionization Chronoscopy**

Dissertation  
zur Erlangung des Doktorgrades  
der Fakultät für Physik  
der Universität Bielefeld

vorgelegt von  
**Thorsten Uphues**  
aus Verl, Deutschland

November 2006





**Assembly and Application of an Instrument for**

**Attosecond-Time-Resolved  
Ionization Chronoscopy**

Dissertation  
zur Erlangung des Doktorgrades  
der Fakultät für Physik  
der Universität Bielefeld

vorgelegt von  
**Thorsten Uphues**  
aus Verl, Deutschland

November 2006



---

”Physics is like sex: sure, it may give some practical results, but that’s not why we do it.”

- *Richard P. Feynman* \*1918, †1988

---

---

Gutachter: Prof. Dr. M. Drescher  
Prof. Dr. D. Anselmetti

Tag der Disputation: 01.03.2007

---

---

Parts of this thesis are published in:

**Attosecond real-time observation of electron tunnelling and multi-electron dynamics in atoms** M. Uiberacker, Th. Uphues, M. Schultze, A.J. Verhoef, V. Yakovlev, M.F. Kling, J. Rauschenberger, N.M. Kabachnik, H. Schröder, M. Lezius, K.L. Kompa, M.J.J. Vrakking, S. Hendel, U. Kleineberg, U. Heinzmann, M. Drescher and F. Krausz, *Nature* (submitted)

Further publications related to the manufacturing of the XUV mirrors and/or using the new experimental setup or the phase stabilized laser system:

**Design, fabrication, and analysis of chirped multilayer mirrors for reflection of extreme-ultraviolet attosecond pulses** A. Wonisch, U. Neuhäusler, N. M. Kabachnik, T. Uphues, M. Uiberacker, V. Yakovlev, F. Krausz, M. Drescher, U. Kleineberg and U. Heinzmann, *APPLIED OPTICS*, **45** 4147-4156 (2006)

**Control of Electron Localization in Molecular Dissociation** M. F. Kling, Ch. Siedschlag, A. J. Verhoef, J. I. Khan, M. Schultze, Th. Uphues, Y. Ni, M. Uiberacker, M. Drescher, F. Krausz, M. J. J. Vrakking, *Science*, **312**, 246-248 (2006)

**Few cycle carrier envelope phase dependent stereo detection of electrons** A. J. Verhoef, A. Fernandez, M. Lezius, K. O'Keeffe, M. Uiberacker and F. Krausz, *Opt. Lett.* (submitted)

**Carrier-envelope phase-stabilized amplifier system** J. Rauschenberger, T. Fuji, M. Hentschel, A.-J. Verhoef, T. Udem, C. Gohle, T.W. Hänsch, and F. Krausz, *Laser Phys. Lett.*, **3** 37-42 (2006)

---

---

---



## Acknowledgements

It was in winter 1998 when I first met *Prof. Ulrich Heinzmann* and *Prof. Markus Drescher* attending a lecture on *EUV- and X-ray optics*. In October 2000 *Prof. Markus Drescher* invited me to the *Institute of Photonics* at the *TU-Wien* for a practical training participating in a project in collaboration with *Prof. Ferenc Krausz* whom I met there for the first time. In those days they were doing the first steps towards attosecond physics.

I finished my diploma in June 2003 and *Prof. Drescher* and *Prof. Heinzmann* offered me the opportunity to start a PhD thesis in collaboration with *Prof. Krausz* in the field of attosecond physics and in the framework of a project funded by the Volkswagen Foundation.

After a short stay in the former laboratories of *Prof. Krausz* in Vienna in the beginning of 2004 I finally joined his new group at the Max Planck Institute of Quantum Optics in Garching in September 2004. In the end of 2004 *Prof. Krausz* offered my colleagues and me the opportunity to develop and setup up a new attosecond experiment in Garching and in January 2005 the planning began. I owe *Prof. Heinzmann*, *Prof. Drescher* and *Prof. Krausz* gratitude for the opportunities and freedom they gave me during this thesis. I really enjoyed the times in Garching.

During my stay in Garching I met *Dipl. Phys. Martin Schultze* with whom I worked closely together designing and setting up the new experimental vacuum system and performing the presented experiments. It has been a great pleasure to work with him. I rarely experienced better cooperation than with him and finally this resulted in a new attosecond beamline within six month starting from scratch. Even if it has been a hard work we had a lot of fun in the lab. Furthermore, I would like to thank *Dipl. Phys. Aart J. Verhoef* setting up and operating the new 3 kHz laser system which is the driving horse for this setup.

Since I was nearly two and a half years in Garching living from the suitcase like

---

a peregrine physicist my special thanks go to Monika Wild for organizing my airport transfers, accommodations and everything else that made this situation more comfortable.

From my recent point of view it is unbelievable that we built the whole experiment in six month starting from scratch with an absolute empty laboratory, without any drawings and even without tools in January 2005, having the first 90 eV harmonic light in June 2005. According to this, I really have to thank the workshops in Bielefeld and Garching for constructing the parts we designed. I want to thank *Wolfgang Gronemeyer* and his coworkers in Bielefeld and *Thomas Strobl* and his coworkers in Garching. Sometimes I felt guilty to annoy them with my constructions and forcing them to manufacture all those things as fast as possible. *Martin Schultze* and I always got the best support we could desire. Finally all the results our team achieved are part of their work as well! Furthermore, the extended insights to "Bavarian Lifestyle" given by the members of the workshop in Garching made it easy to relax sometimes.

I thank *Prof. Ulf Kleineberg* and *Dipl. Phys. Stefan Hendel* to support me with information on the XUV mirror characteristics.

Setting up the system it has been necessary to send parts between Bielefeld and Garching by mail. I really thank *Dipl. Phys. Martin Michelswirth* for his patience packing and sending me a lot of packets to Garching and for his support with optical simulations using ZEMAX.

I thank *Dr. Matthias Kling* and *Dr. Vladislav Yakovlev* for their work regarding the data analysis and computations that were necessary for interpretation and furthermore, for some nice times in Garching and Szeged.

In August 2005 and in the framework of a different project I worked together with *Dr. Adrian L. Cavalieri* setting up an attosecond solid state experiment. I really enjoyed working with him and we had some fun besides working in the laboratory and even there. I want to thank him reading and correcting my thesis in terms of my English writing.

Moreover, I like to thank *Jens Rauschenberger* for his last-minute support in terms of complicated routes to get access to some papers in the middle of the night.

My special thanks go to *Prof. Nikolay Kabachnik* for his support and a lot of fruitful discussions related to the interpretation of our experimental data and

---

the preparation of the level diagrams.

I would like to thank all members of the working group "*Molekül- und Oberflächenphysik*" in Bielefeld. Most importantly *Karin Wisotzky* and *Kay Lofthouse* for their remote support on any kind of *bureaucratic* problems. The student assistant *Patrick Rüdiger* for his support in any kind of work that needed to be coordinated in Bielefeld when I was already back on my way to Garching.

Furthermore big thanks go to all members of the working group "*Attosecond and High-Field Physics*" in Garching. Especially *Dr. Hartmut Schröder* for a lot of interesting discussions and insights into laser ionization experiments and *Dr. Reinhard Kienberger* for "strategic" afterwork meetings.

For their assistance my great thanks go to my family and to *Hedi* and *Rainer* for their support during the last year of my PhD thesis as well as *Julia* reading and correcting grammar in parts of this thesis.

Most importantly, my greatest thanks go to *Barbara* for her patience wasting our living room with papers and books writing this thesis and her extensive encouragement during my thesis in the last years without questioning anything.

THANK YOU!

---



---

# Contents

<b>Acknowledgements</b>	<b>i</b>
<b>1 Introduction</b>	<b>1</b>
<b>2 Theoretical Background</b>	<b>5</b>
2.1 Interaction of atoms with strong laser fields . . . . .	6
2.1.1 The Keldysh Approach . . . . .	7
2.1.2 ADK Theory . . . . .	10
2.1.3 Multiphoton regime . . . . .	12
2.1.4 Tunneling regime . . . . .	13
2.1.5 High Harmonic Generation . . . . .	15
2.2 Inner-shell Processes in atoms . . . . .	18
2.2.1 Excitation, Shake-Up, Shake-Off . . . . .	18
2.2.2 Auger and Resonant Auger decay . . . . .	19
2.2.3 Nature of decay cascades . . . . .	21
2.3 Atomic Lifetimes . . . . .	22
2.4 Few-cycle laser and isolated attosecond pulses . . . . .	24
2.4.1 Femtosecond laser pulses - a mathematical description . . . . .	24
2.4.2 Optical elements of a few-cycle laser system . . . . .	25
2.4.3 Generating few-cycle laser pulses . . . . .	27
2.4.4 Generation of isolated attosecond pulses . . . . .	29
2.5 Principle of time resolved pump-probe measurements . . . . .	32
<b>3 Experimental Setup</b>	<b>37</b>
3.1 Laser System and Diagnostics . . . . .	39
3.2 Vacuum Layout and Vibration Control . . . . .	40
3.3 Vacuum System and Diagnostics . . . . .	41
3.3.1 High Harmonic Generation . . . . .	41
3.3.2 Differential pumping and XUV detection . . . . .	42
3.3.3 Experimental Chamber . . . . .	43
3.4 Experimental Environment . . . . .	47

---

---

3.4.1	Data Acquisition . . . . .	48
3.4.2	Beamline Automation . . . . .	49
3.4.3	Reflectron ion mass spectrometer . . . . .	50
<b>4</b>	<b>Characterization measurements</b>	<b>53</b>
4.1	CEP few-cycle Laser System . . . . .	53
4.2	High Harmonic Beam characterization . . . . .	55
4.2.1	Measurement of the focus size . . . . .	59
4.2.2	Calculation of the effective partial XUV cross-sections . . . . .	61
4.2.3	Resolution of the Reflectron ion mass spectrometer . . . . .	63
<b>5</b>	<b>Attosecond time-resolved observation of ionization processes</b>	<b>65</b>
5.1	Tunneling ionization dynamics in Neon . . . . .	69
5.2	Multi-electron ionization dynamics in Krypton . . . . .	74
5.3	Multi-electron ionization dynamics in Xenon . . . . .	79
<b>6</b>	<b>Conclusions and outlook</b>	<b>85</b>
	<b>Appendix A - Vacuum Layout</b>	<b>89</b>
	<b>Appendix B - "Soft" - Knife Edge</b>	<b>91</b>
	<b>Appendix C - <math>\gamma</math> parameter neon</b>	<b>93</b>
	<b>Appendix D - Data analysis</b>	<b>95</b>
	<b>Appendix E - Measurement and Automation Software</b>	<b>99</b>
	<b>Bibliography</b>	<b>103</b>

---

# Chapter 1

## Introduction

The interaction of light and matter is one of the most historically rich fields of atomic physics. In the beginning of the last century Albert Einstein discovered and described the *photoelectric effect* [1] by studying the emission of electrons produced by photons interacting with matter. Only twenty years later Pierre Auger observed the emission of more than one electron under the influence of light with a characteristic behavior dependent on the material which is known as the *Auger effect* [2]. In one century of investigation of the interaction of light with matter there are still open questions that give rise to further investigations like the ones in this thesis.

In the mid-1940's *synchrotron radiation* became the light source for investigations into these interactions due to good tunability in the desired wavelength range [3, 4]. Even nowadays next generation of synchrotrons are existing and deliver most of the experimental results regarding these fields of atomic physics.

Nearly at the same time synchrotron sources became available for a large user community, the independent development of the laser began. In 1960 Theodore Maiman and Nikolai Basov built the first working ruby-laser and from this point the rapid development of pulsed laser sources of ever shorter pulse durations began. Figure 1.1 shows the development of the laser pulse duration over the years, starting with the ruby-laser in 1960 denoting the milestones in laser development.

Only twenty years ago in 1985 Mourou *et al.* proposed and demonstrated the technique of *Chirped Pulse Amplification (CPA)* [5]. With this technique the intensity of a laser pulse could be increased by orders of magnitude overcoming the damage threshold problem of gain media.

In 1991 Sibbet *et al.* demonstrated the principle of Kerr-Lens Modelocking

---

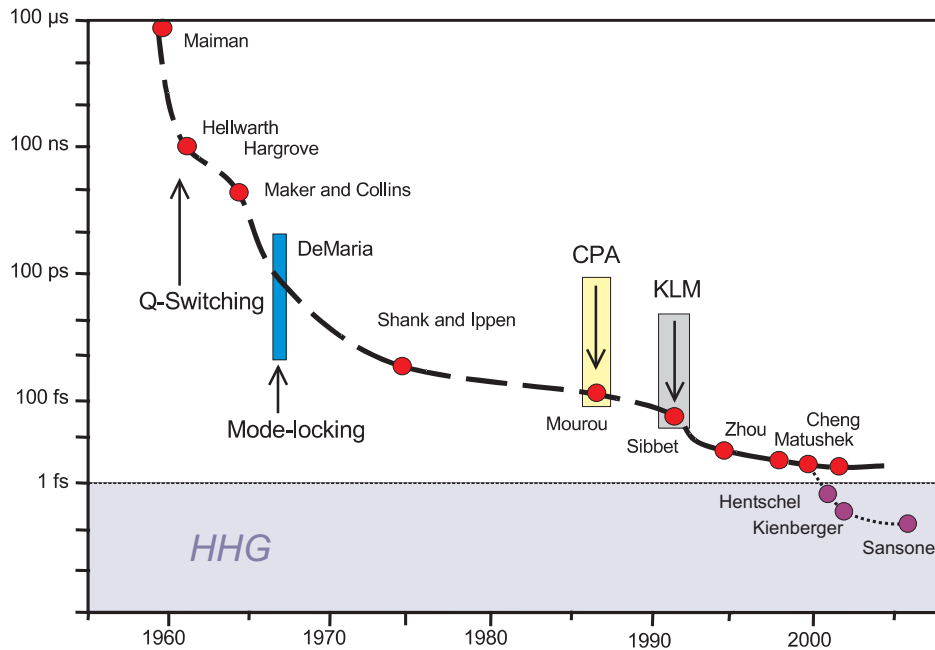


Figure 1.1: Development of the pulse duration over the last 50 years from [6] and updated.

(KLM) leading to ever shorter pulses and in combination with the technique of *Chirped Pulse Amplification (CPA)* to high energetic pulses. From the beginning of the new century these ultra-short pulse sources have been used to produce pulses in the soft x-ray range (XUV) as multiple harmonics of the fundamental laser radiation and opened up the door for attosecond physics [7, 8, 9, 10, 11, 12].

Figure 1.2 compares the new High Harmonic sources with some synchrotron facilities and the Free-Electron-Laser FLASH currently under development at DESY in Hamburg. The pulses produced by High Harmonic sources are much shorter, therefore the peak Brilliance of these sources is comparable. Since the generated harmonics are produced in the XUV range these sources can serve for the same experiments as synchrotron sources do. The main difference is based on the fact that an XUV pulse from an ultra-short laser driven High Harmonic source is in the attosecond regime and therefore much shorter than the typical duration of a synchrotron pulse. For this reason it became possible in recent years to perform comparable experiments that were carried out in the energy domain with synchrotron radiation in the time domain using High Harmonic sources to observe dynamics in atomic rearrangement in real time.

In the framework of this thesis a new setup for attosecond time-resolved



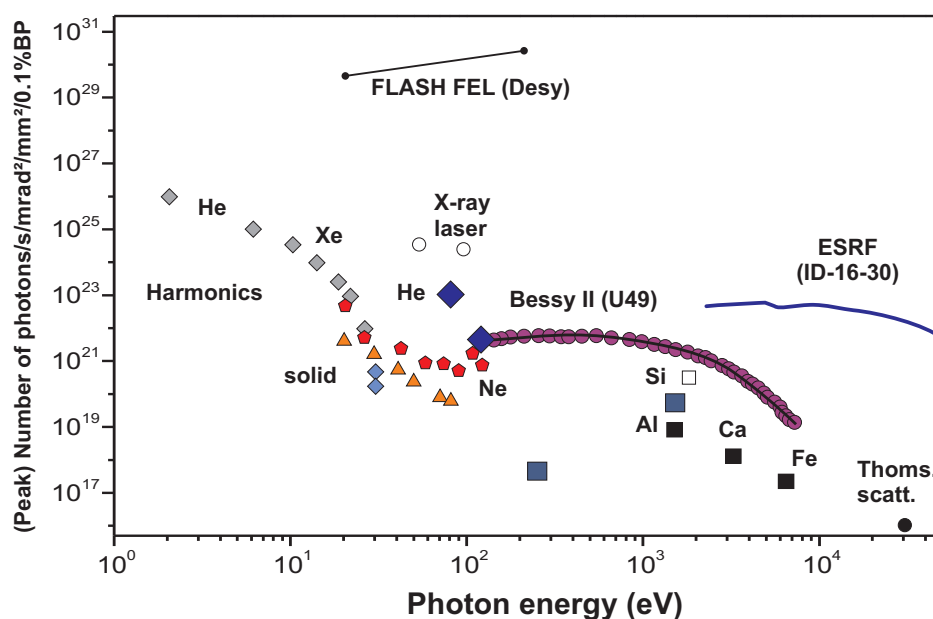


Figure 1.2: Peak brilliance of various short pulse x-ray sources (harmonics x-ray laser, laser-produced plasmas, synchrotrons) compared to the FLASH Facility in Hamburg [13]

measurements has been built and observation of ionization dynamics in rare gas atoms have been made. This new technique presented in this thesis is entitled *Ionization Chronoscopy* and gives further evidence that time-resolved experiments in the attosecond regime will become a powerful tool for investigations in atomic physics.

In the first part of this thesis a general outline of the interaction of strong laser fields with matter will be given followed by the description of inner-shell processes in atoms with respect to the atomic systems under observation in these experiments.

When discussing attosecond time-resolved studies of ionization dynamics it becomes necessary to explain the principles of *few-cycle laser pulse generation*, *carrier envelope phase stabilization* and *High Harmonic Generation (HHG)* as the fundamental concepts to the generation and application of *pump-probe* experiments with isolated attosecond pulses, which is covered in the second half of this section. According to studies in the time domain the principle of pump-probe experiments is the key technique to perform these studies. It will be covered theoretically and with respect to the experimental part of the thesis.

Since a major part of was the development and setup of a new attosecond experimental system, the second part will describe the realized concepts under the focus of design restrictions defined in the beginning of the development. Essentially data acquisition and computer controlled measurements in closed loop arrangements are a very important part of this work concerning the necessity of adjustment of all optical parts in vacuum and partly on a sub-micrometer scale. Furthermore, monitoring and diagnostics are important for the proper establishment of identical experimental situations in day-to-day operation.

In the third part the experimental apparatus will be characterized by means of focus sizes, divergence and size of the harmonic beam. The resolution of the detector used in the current experiments will be demonstrated. Comparison will be made with respect to synchrotron measurements leading to the main part of this thesis regarding pump-probe measurements of ionization dynamics in rare gas atoms.

Time-resolved measurements of neon, krypton and xenon will be presented and discussed regarding strong field tunnel ionization and inner-shell decays to show the main differences of these experiments with respect to comparable measurements in the energy domain and the theoretical basis discussed in the first part.

In conclusion, the achieved result will be summarized and future prospects for applications of attosecond pump probe experiments will be given.

---

## Chapter 2

# Theoretical Background

Attosecond time-resolved measurements of ionization processes in excited atomic states with a strong field few-cycle laser pulse are related to several different fields of physics regarding the interaction of atoms with strong laser fields: *inner-shell excitation* and *ionization* with the related inner atomic relaxation processes, concepts and techniques of few-cycle laser pulse generation and the principles of pump-probe measurements that will be covered in this theoretical introduction.

The theories of the interaction of light with atoms cover a wide range of processes on its own. The most important to this specific work are the principles of *High Harmonic Generation (HHG)* and *strong field ionization* on one side and *inner-shell processes* induced by the interaction of the atom with an ultrashort XUV pulse ionizing a core electron on the other side. Furthermore, the decay of the inner-shell vacancy created by the XUV pulse can cause secondary processes like *Auger decay*, *electron shake-up/shake-off* and further *excitation* of bound electrons in the remaining atomic ion, which becomes of importance with respect to the experiments that are discussed in chapter 5.

Since the recent developments in the field of attosecond physics begin to utilize the techniques developed during the last years, the interest in inner-shell processes increases again due to the fact, that the energy of the incident XUV photons is comparable to the photon energies used in synchrotron experiments studying inner-shell processes in the energy domain. As will be shown throughout this thesis, under certain experimental conditions attosecond time-resolved studies are a unique tool to measure time constants of sequential decay channels in atoms that are not directly accessible in the energy domain. Moreover the intensity-dependent ionization yield of dedicated levels becomes observable by means of tunnel ionization intensities.

---

Even though the development of new laser sources with pulse durations approaching the single-cycle limit and increasing intensities [14, 15, 16] are of main interest. These sources are utilized to generate ultra broadband isolated single attosecond pulses [17] down to the few-cycle regime. Also new techniques for the generation of isolated attosecond pulses are under development [18] striving for the establishment of attosecond physics.

In this chapter the basic theoretical descriptions of ionization in strong fields will be covered as well as inner-shell processes in atoms in relation to the lifetimes of the atomic states involved.

To become familiar with the experimental concepts the generation of *few-cycle laser pulses* and *single isolated attosecond pulses* by use of the principles of *HHG* will be discussed.

Connecting all the described theories and techniques finally lead to the main principle of *time-resolved pump-probe measurements* which is explained with respect to the attosecond time scale in chapter 5.

## 2.1 Interaction of atoms with strong laser fields

In discussing the electronic dynamics of an atom exposed to a strong laser field, it becomes necessary to define what is really meant by a strong field with respect to the Coulomb potential. For demonstrative purposes let us use the hydrogen atom.

The strength of the Coulomb potential experienced by an electron in the first Bohr orbit of atomic hydrogen is given by

$$\mathcal{E}_a = \frac{e}{(4\pi\epsilon_0)a_0^2} = 5.14221 \times 10^9 \text{V/cm} \quad (2.1)$$

Furthermore, the relation between intensity and field strength of the laser electric field is given by

$$I = \frac{1}{2}\epsilon_0 c E^2 \quad (2.2)$$

If  $I$  is expressed in  $\text{W cm}^{-2}$  and  $E$  in  $\text{V cm}^{-1}$  Eq. (2.2) can be written more simply as

---

$$I = 1.33 \times 10^{-3} E^2 \quad (2.3)$$

$$E = 27.4\sqrt{I} \quad (2.4)$$

Using Eq. (2.1) the field intensity corresponds to  $3.51 \times 10^{16} \text{ W cm}^{-2}$  which is an intensity that can easily be achieved. Even for moderate intensities of about  $10^{15} \text{ W cm}^{-2}$ , which are easily achievable with laser sources commercially available today, the field strength is about 30% of the Coulomb field.

If the field strength is found to be in this regime the description of the interaction in terms of perturbation theory is not valid anymore because the perturbation of the Coulomb potential cannot be treated as weak (see 2.1.3). A strong and time varying potential applied to an atom competes with the Coulomb binding potential. Thus the dynamics of the ionization process of a bound electron inside the potential is strongly determined by the instantaneous strength of the applied electric field. For these intensities *Tunnel Ionization (TI)* and *Over the Barrier Ionization (OTBI)* are the dominating processes that cause an atom to ionize. Especially for the case of *Carrier Envelope Phase (CEP) stabilized few-cycle pulses* this becomes of major importance (see 2.5). The process of *High Harmonic Generation (HHG)* is the key process for generation of attosecond XUV pulses and is related to the propagation of a free electron in a strong linear polarized electromagnetic field which will be discussed in 2.1.5. Regarding field strength much weaker than this, the interaction of an atom with the laser field can be treated in terms of perturbation theory and processes like *Multi Photon Ionization (MPI)* or *Above-Threshold Ionization (ATI)* can be explained.

## 2.1.1 The Keldysh Approach

Assuming the interaction of an atom with a time varying electric field, the instantaneous field strength changes by order of magnitude within a half cycle of the period  $T$ . In relation to the main aim of this thesis to resolve ionization dynamics on an attosecond time scale, it is necessary to determine the nature of the ionization process with respect to the field strength.

One of the most important approaches was published in 1965 by L. V. Keldysh [19]. Keldysh derived a model to determine the ionization probability of an atom in the field of a strong electromagnetic wave that connects continuously the two limiting cases of *MPI* and *OTBI*. Furthermore, the effect of resonant excitation of an atom is included which explains the increase of the ionization

---

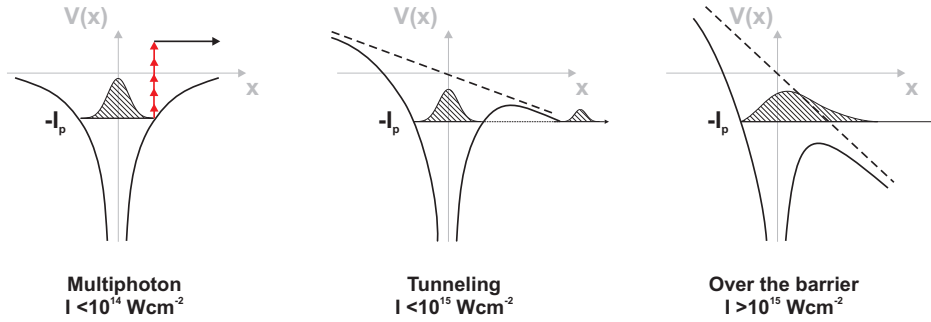


Figure 2.1: Schematic diagram showing the three possible mechanisms for ionization [20]. The probability of the process depends on the intensity  $I$

cross-section by orders of magnitude in the vicinity of a resonance.

Figure 2.1 shows the three cases mentioned above. For low laser intensities  $I < 10^{14} \text{ W cm}^{-2}$  the ionization is dominated by the multiphoton ionization process. Via intermediate states the electron wave packet is lifted to the continuum (*vertical channel* [21]).

For higher intensities the Coulomb potential starts to be perturbed by the electric field and  $TI$  starts to dominate. The Coulomb potential is suppressed so strongly that it becomes probable for the electron wave packet to appear in the continuum by tunneling through the barrier (*horizontal channel*). For even higher intensities the Coulomb barrier is suppressed completely and the wave packet can evolve in the continuum directly.

Once the electron is free it experiences a quiver motion by the laser electric field. This energy is called the ponderomotive energy  $U_p$  given by

$$U_p [\text{eV}] = \frac{e^2 \mathcal{E}_0^2}{4 m \omega_L^2} = 9.33 \times 10^{14} I [\text{W/cm}^2] \lambda^2 [\mu\text{m}] \quad (2.5)$$

where  $m$  is the mass of the electron,  $e$  the charge and  $\mathcal{E}_0$  the field strength.

The benefit of the Keldysh approximation is to derive the nature of ionization processes in a quasi-static model. The two boundaries are defined by the interaction of the atom with a weak high frequency field in the case of *MPI* and a very strong, low frequency field in the case of *TI* or *OTBI*. The transition from *multiphoton* to *tunneling* regime is determined by the Keldysh adiabatic parameter  $\gamma$  that will be expressed below.

For simplicity Keldysh assumes a classical particle with binding energy  $I_p$ . Regarding the tunneling case in Fig. 2.1, once the Coulomb potential is suppressed sufficiently that the electron has a certain probability to tunnel out of the atom, it will need a certain time to penetrate through the barrier with a thickness  $l$  determined by the binding energy and the applied field strength

$$l = \frac{I_p}{e \mathcal{E}_0} \quad (2.6)$$

Thus a tunneling time<sup>1</sup>  $\tau$  for the particle penetrating through a triangular barrier created by a constant electric field can be associated with

$$\tau = \frac{\sqrt{2mI_p}}{e \mathcal{E}_0} \quad (2.7)$$

Multiplying Eq. (2.7) with the frequency of the laser field  $\omega_L$  we obtain the definition of the Keldysh adiabatic parameter  $\gamma$  as the ratio of the laser and tunneling frequencies to be

$$\begin{aligned} \gamma = \tau \omega_L &= \omega_L \frac{\sqrt{2mI_p}}{e \mathcal{E}_0} \\ &= \sqrt{\frac{I_p}{2U_P}} \end{aligned} \quad (2.8)$$

The Keldysh parameter  $\gamma$  distinguishes between the ionization processes in the limiting cases  $\gamma \gg 1$  for *multi photon ionization (MPI)* and  $\gamma \ll 1$  for *tunneling ionization (TI)*.

Looking at Eq. (2.7) again we see that the value of  $\tau$  is determined by the frequency of the laser field. Regarding high frequencies for the applied field there should appear a frequency dependent tunneling probability. Moreover, assuming a time varying ponderomotive potential  $U_p(t)$ , Eq. (2.9) defines a time varying relation for either the *MPI* or *TI* regime to dominate the ionization process. At this point it needs to be emphasized that the  $\gamma$  parameter should be interpreted in terms of the dominance of one process in respect to the other [21]. With regard to the *Strong Field Approximation (SFA)* covered by the works of *Faisal* [24] and *Reiss* [25] the interpretation could be misleading in that for  $\gamma > 1$  everything is purely *MPI*. This is not the case because *SFA* excludes

---

<sup>1</sup>the definition of an appropriate tunneling time is one of the most affected problems in theory. The classical treatment as a particle is one of the commonly used definitions to avoid a formulation in the wave packet picture and is suitable for most of the problems under investigation. For a more detailed review on the discussions and models see [22, 23]

the possibility that an electron absorbs energy while moving under the barrier. For this reason most interpretations of *ATI* rely on interpretations in terms of *MPI* with a virtually modified binding potential, as will be discussed in 2.1.3.

Finally the Keldysh interpretation allows calculation of ionization probabilities of atomic bound states in strong laser fields including excitations and resonances and even the dependence on the time evolution of the laser field in the *Quasi-Static-Approximation (QSA)*, taking ultrashort pulses in the few-cycle regime into account.

The ionization probability is given by

$$W_K = \frac{\sqrt{6}\pi}{4} \frac{I_p}{\hbar} \sqrt{1 - \frac{e\mathcal{E}_0\hbar}{m^{1/2}I_p^{3/2}}} \times \exp \left[ -\frac{4}{3} \frac{\sqrt{2m} I_p^{3/2}}{e\hbar\mathcal{E}_0} \left( 1 - \frac{m\omega^2 I_p}{5e^2\mathcal{E}_0^2} \right) \right] \quad (2.9)$$

The most obvious limitation of the Keldysh approximation is given by the fact that Keldysh makes a low-frequency approximation for the applied electric field. Furthermore, the final state of the electron is a free electron oscillating in the laser field, which is known as a final nonperturbative Volkov state. The developments in *SFA* and even recent improvements of the original Keldysh theory tend to resolve a fully quantum mechanical treatment of the problem to overcome these limitations<sup>2</sup>. Generally, the Keldysh approach does not include any kind of species dependence in the ionization rate calculation.

## 2.1.2 ADK Theory

Twenty years after *Keldysh* published his work on ionization in the field of a strong electromagnetic wave *Ammosov, Delone and Krainov* developed a theory (*ADK*) [29] based on the earlier work of *Perelomov et al.* [30] and was extended to describe the ionization of complex atoms and atomic ions in arbitrary states.

The ionization rate equation in atomic units is given by

$$W_{mADK} = |C_{n^*l^*}|^2 f_{lm} I_p \sqrt{\frac{6}{\pi}} \left( \frac{2(2I_p)^{3/2}}{\mathcal{E}} \right)^{2n^* - |m| - 3/2} \times \exp \left( -\frac{2(2I_p)^{3/2}}{3\mathcal{E}} \right) \quad (2.10)$$

---

<sup>2</sup>see [26, 27]; for a detailed comparison [28]



with the factors  $f_{lm}$  and  $|C_{n^*l^*}|^2$

$$f_{lm} = \frac{(2l+1)(l+|m|)!}{2^{|m|}|m|!(l-|m|)!} \quad (2.11)$$

$$|C_{n^*l^*}|^2 = \frac{2^{2n^*}}{n^*\Gamma(n^*+l^*+1)\Gamma(n^*-l^*)} \quad (2.12)$$

where  $n^*$  is the effective principal quantum number,  $m$  the magnetic quantum number and  $l$  the angular momentum respectively.  $I_P$  is the atomic ionization potential and  $\mathcal{E}$  the electric field strength of the laser.

For ionization rate calculation the ground state values for  $n^*$  and  $l$  are mainly used, which leads to  $l^* = n^* - 1$ .

Averaging over all magnetic quantum numbers gives the complete ionization rate

$$W_{ADK} = \frac{1}{2l+1} \sum_{m=-l}^l W_{mADK} \quad (2.13)$$

Considering a gaussian laser pulse, the electric field is expressed in the form

$$\mathcal{E}(t) = \mathcal{E}_0 \exp\left(-\frac{2 \ln 2 t^2}{\tau_{in}}\right) \cos(\omega_0 t) \quad (2.14)$$

where  $\omega_0$  is the central frequency,  $\tau_{in}$  is the *full width at half maximum (FWHM)* of the pulse. Integrating Eq. (2.13) in the form

$$\widetilde{W}_{frac} = \int_t^{+\infty} W_{ADK}(\mathcal{E}(t')) dt' \quad (2.15)$$

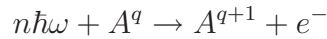
gives the total number of ions created within a subfraction of the laser pulse starting to act on the atom at time  $t'$ . Note that this definition differs from the expression included in the definition of the ion yield (e. g. [31]). The integration is given in the limits  $t \rightarrow +\infty$  in Eq. (2.15). Usually the limits are  $-\infty \rightarrow t$  (compare Eq. (2) in [31]). This difference reflects the experimental fact that the main interest is focused on the ions created starting at a certain point  $t$  with a defined field strength inside the pulse and getting information on the integrated ionization rate for the remaining part of the pulse.

With respect to Eq. (2.11) and assuming that a selected state is created at some point  $\tau_D$  inside the envelope of the laser pulse, it is obvious that a time dependent dynamic can be observed in the ionization rate defined by Eq. (2.15). This is important for the main ideas of the experiments described in 2.5 and the subsequent discussion on results.

### 2.1.3 Multiphoton regime

Regarding the Keldysh parameter the regime of multiphoton ionization is treated as the absorption of  $n$  quanta of energy  $\hbar\omega$  to eject a bound electron into the continuum.

Generally, the process for *MPI* follows the reaction:



for  $\gamma \gg 1$ . In this limiting case the  $n$ -photon ionization rate is given by

$$\Gamma_n = \sigma_n I^n \quad (2.16)$$

where  $n$  is the minimum number of photons needed for ionization,  $\sigma_n$  is the generalized cross-section and  $I$  the intensity of the incident light. With increasing intensity this scaling breaks down due to the fact that for a given pulse duration, there is a maximum intensity above which no more ionization can occur since the state to be ionized is depleted and all atoms are ionized. This value of intensity is known as the *saturation intensity*  $I_{sat}$ .

#### Above-threshold ionization (ATI)

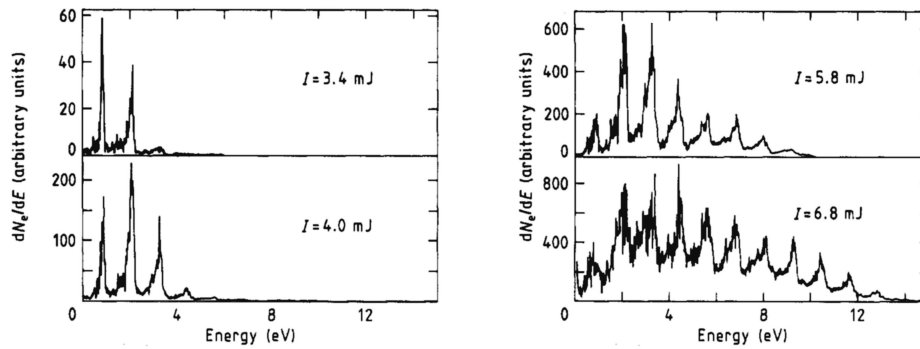


Figure 2.2: Electron spectra of eleven-photon *MPI* at 1064 nm for different pulse energies (adapted from [32])

When the ponderomotive potential  $U_p$  starts to perturb the Coulomb potential, Eq. (2.16) is no longer sufficient to describe the ionization rate.

In Fig. 2.2 photoelectron spectra of xenon taken at different intensities in the case of eleven-photon absorption *MPI* at 1064nm are shown. With increasing intensity the number of photoelectron peaks separated by the energy of a single photon quantum can be observed. Furthermore, for the highest energies the first peak in the spectrum is suppressed and a background of equally distributed electrons blurs the spectrum. This behavior can be addressed to the absorption of more photons than required to overcome the binding potential of the atom. This case is called *ATI*. For *ATI* in a first instance the ionization rate is given by

$$\Gamma_n \propto I^{n+s} \quad (2.17)$$

with the electron kinetic energy distribution expressed by

$$E_{kin} = (n + s)\hbar\omega - E_b \quad (2.18)$$

where  $n$  is the minimum number of photons needed to ionize the electron with the ionization potential  $E_b$  and  $s$  the number of excess photons absorbed.

This description can only be addressed to the lowest intensity shown in Fig. 2.2. For higher intensities we see a peak-switching for the maximum electron count rate that can be assigned to the increasing influence of the ponderomotive potential on the binding potential of the atom. This leads to an "up-shift" of the effective ionization potential of the atom by  $U_p$  thus the ionization by absorption of a smaller number of photons becomes unfavorable. In this case Eq. (2.18) becomes

$$E_{kin} = (n + s)\hbar\omega - (E_b + U_p) \quad (2.19)$$

In the cases of *MPI* and *ATI* the processes can be treated quantum mechanically with perturbation theory which results in the same final equation for the position of the peaks appearing in the electron spectrum given by Eq. (2.19) [20]. This treatment includes the *Stark shift* and depletion of the initial state.

For the highest intensity shown in Fig. 2.2 the tunneling process starts to mix with *ATI* which is indicated by the smooth background rising under the low energy peaks.

## 2.1.4 Tunneling regime

In the quasi-static limit and with respect to the *Keldysh approximation* [19], an electron wave packet in its ground state has a non zero probability to tunnel

---

through the potential well at every time the potential barrier is sufficiently suppressed by the instantaneous potential of the laser field. The ionization rate can then be calculated [33]:

$$\Gamma_{QS}(t) = 4 \frac{(2I_p)^{5/2}}{\mathcal{E}(t)} \times \exp \left[ -\frac{2(2I_p)^{3/2}}{3\mathcal{E}(t)} \right] \quad (2.20)$$

where  $I_p$  is the ionization potential of the atom,  $\mathcal{E}(t)$  the laser electric field as defined in Eq. (2.14), and the suffix  $QS$  stands for quasi-static.

The ionization rate has a highly nonlinear dependence on the instantaneous value of the electric field. At the zero-crossings of the oscillating laser field the atomic potential is unperturbed hence the ionization rate is zero. This adiabatic assumption of the ionization process is only justified if the tunneling time defined in Eq. (2.7) is significantly smaller than the laser period and the maximum field strength of the laser electric field is insufficient for complete barrier suppression of a given bound state. This condition is known as *tunneling ionization (TI)* revealing a Keldysh parameter  $\gamma \ll 1$ .

For noble gases and for laser wavelengths in the visible and near infrared, the intermediate regime where the *Keldysh parameter*  $\gamma \sim 1$  is related to the *Over the Barrier Ionization (OTBI)* [31]. For field strengths  $\mathcal{E} > \mathcal{E}_{bs}$  where the barrier of the Coulomb potential becomes suppressed by the electric field, the electron escapes directly from the potential well without tunneling through a barrier as shown in the right part of Fig. 2.1. A critical laser intensity  $I_c$  can be defined describing the intensity at which the Coulomb barrier starts to be suppressed [20]

$$\begin{aligned} I_c [W/cm^2] &= \frac{\pi^2 c \epsilon^3 I_p^4}{2Z^2 e^6} \\ &= 4 \times 10^9 I_p^4 [eV] Z^2 \end{aligned} \quad (2.21)$$

where  $Z$  is the charge of the relevant atom or ion and  $I_p$  the ionization potential.

Obviously all the described processes are coexisting in the ionization process, since the maximum intensity of a laser electric field exceeds the critical intensity  $I_c$  varies from zero to its maximum value inside the pulse envelope. Therefore, the corresponding routes to ionization are all present in the evolution of the laser field with respect to a discrete state. Finally the evolution of the electric field and the maximum strength determine how rapidly one of the described regimes is entered.

---

## 2.1.5 High Harmonic Generation

*HHG* is the leading technique on the attosecond frontier [9, 7, 11] and could even lead to the generation of coherent pulsed x-rays with a tabletop source.

The semiclassical model of high harmonic generation is often described in a *three-step-model* attributed to *Corkum* [36].

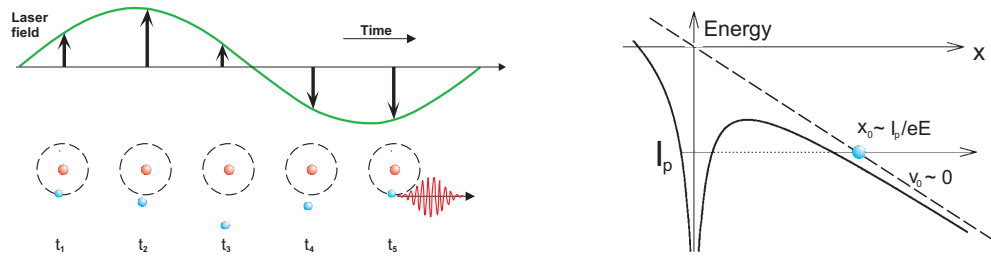


Figure 2.3: Scheme of a single atom in the presence of an intense laser field; the right side shows the variation of the atomic potential in presence of the laser electric field; the effective atomic potential is given by the solid line. The dashed line shows the electric field; the left side shows the electron's motion in the field once born free by tunnel ionization [34]

In the first step an atom is ionized by an electron tunneling through the barrier of the atomic potential suppressed by the laser electric field, as is shown on the right side of Fig. 2.3. Once born free, the electron oscillates with the laser electric field as shown on the left side of Fig. 2.3. The electron receives an acceleration due to the presence of the electric field. With a certain probability the electron will rejoin its parent ion and recombine. The energy the electron gained from the laser electric field will be set free in a high energetic photon with a multiple of the laser field frequency.

$$E_{hh} = n \cdot \hbar\omega \quad (2.22)$$

where  $\omega$  is the laser field frequency and  $n$  is an odd integer.

The formulation of this semiclassical model neglects the influence of the atomic potential once the electron is born. This is one of the most general approximations to assume a zero-range-potential.

The maximum extractable energy can be calculated using the classical electron trajectories of a free electron born at a time  $t_0$  in a laser field which leads to the most cited formula for *HHG* [35].

$$E_{hh}^{cutoff} = I_p + 3.17 \cdot U_p \quad (2.23)$$

where  $I_p$  is the ionization potential of the atomic gas and  $U_p$  the ponderomotive potential of the laser electric field. This energy called the *cutoff energy*, is exactly the energy range in which isolated attosecond pulses are produced and is predicted by this semiclassical approach [36]. Usually this approach supposes the high intensity regime for the laser electric field and thus  $I_p \ll U_p$ .

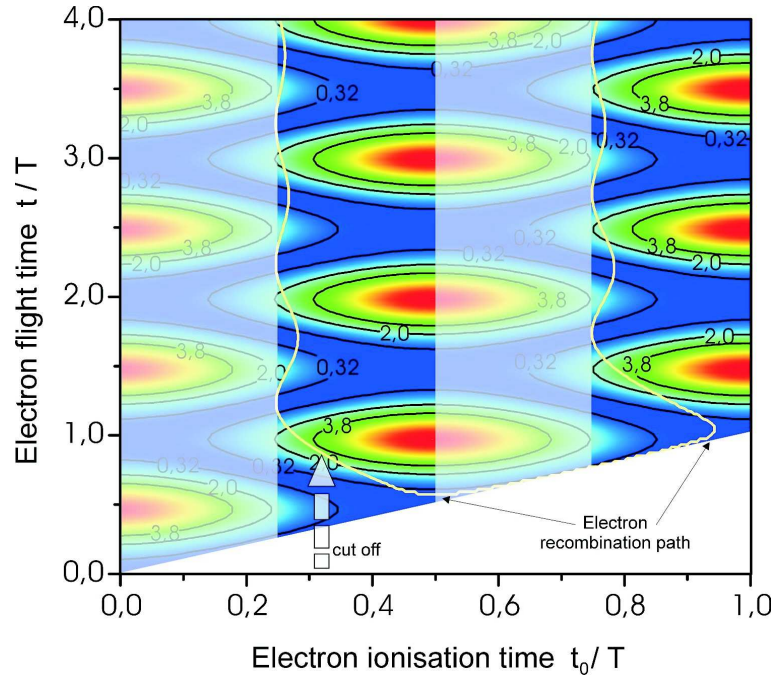


Figure 2.4: kinetic energy and recombination times of the free born electron at the time  $t_0$  in the laser field with period  $T$ ; the contour plot shows the kinetic energy; the white path shows the possible recombination gain times and the correlated kinetic energy; the white arrow indicates the maximum possible gain [37]

Figure 2.4 shows the electron's kinetic energy calculated using classical electron trajectories in a contour plot. From the possible recombination paths it becomes clear that only electrons born in the second and fourth quarter of the laser electric field period contribute to the process of *HHG*.

Several different quantum mechanical treatments of *HHG* were made using perturbation theory [35, 20]. Some of them make use of *SFA* mentioned above based on the time-reversed  $\hat{S}$  matrix theory proposed by *Keldysh* and *Reiss* [19, 25]. Generally, the aim of the theoretical description is a unified theory for *HHG* and *ATI* (*Above-Threshold-Ionization*) [38] and at last a unified theory for the single cycle and multicycle regime of *HHG*.

One of the first quantum mechanical formulations of *HHG* is given in *Lewenstein et al.* [35]. This formulation is based on the *SAE (Single Active Electron)* approximation for an electron under the influence of a linear polarized laser electric field.

Generally, a quantum mechanical approach leads to the solution of the Time Dependent Schrödinger Equation (*TDSE*). Assuming a periodic laser electric field, the TDSE is given by

$$i|\Psi(\mathbf{x}, t)\rangle = \left[ -\frac{1}{2}\nabla^2 + V(\mathbf{x}) - E \cos(t)x \right] |\Psi(\mathbf{x}, t)\rangle \quad (2.24)$$

The ground state is given by  $|0\rangle$  and is assumed to be spherical symmetric. As we can see in Fig. 2.3 the electron typically leaves the atom when the field reaches its peak value. Therefore the influence of the atomic potential  $V(x)$  can again be neglected.

The basic assumptions for this formulation of *HHG* are:

- the contribution to the evolution of the system of all bound states except the ground state  $|0\rangle$  can be neglected
- the depletion of the ground state can be neglected since  $U_p < U_{sat}$ ,  $U_{sat}$  being the saturation energy that completely ionizes the atom in one optical period
- in the continuum the electron can be treated as a free particle moving in the electric field with no effect of  $V(x)$

For the quantum mechanical model the calculations in [35] lead to the existence of only odd harmonics because of the symmetry of the atomic potential and the principle of energy conservation. This was already assumed in the semiclassical model.

Furthermore, the electron is born free in the continuum with zero initial velocity as a result of the quantum mechanical treatment. For the semiclassical model this was an assumption, as well. Comparing both models the semiclassical model for *HHG* is based on the fact that the free electron recombines at the same position in space where it starts. The dimensions of the atom cannot be neglected and therefore the potential of the nucleus affects the recombination process. Since the electron must tunnel out it cannot appear in the continuum at the origin of the nucleus and thus it cannot recombine at the origin. Additionally the electron can receive a gain in energy given by the acceleration the electron receives on the way to the origin in the potential of the nucleus. Other effects

---

like quantum interference or spread of the wave packet are not included.

As a result of the more accurate quantum mechanical calculations the *cutoff law* has been corrected giving

$$E_{hh}^{cutoff} = 3.17 U_p + I_p \cdot F(I_p/U_p) \quad (2.25)$$

For  $I_p \ll U_p \implies F(I_p/U_p) \simeq 1.32$ .

Finally *HHG* by a few-cycle pulse in the *cutoff range* for attosecond pulse generation requires to control the *carrier envelope phase* of the laser pulse ensuring the creation of isolated attosecond pulses. A detailed description and routes to other concepts getting isolated attosecond pulses are shown in 2.4.

## 2.2 Inner-shell Processes in atoms

Discussions about inner-shell dynamics of atoms in the context of this thesis in the following sections are restricted to interactions of neutral atoms with high energetic photons. If the energy of an incident photon  $\hbar\omega$  exceeds the binding energy or ionization threshold  $E_b$  of an inner-shell electron, different processes follow the interaction. In the most simple case the corresponding electron is just *photoionized* following the reaction



and the kinetic energy of the ejected electron is given by

$$\hbar\omega - E_b = E_{photo}^{kin} \quad (2.27)$$

Due to the ejection of an inner-shell electron, processes described in the following sections become probable.

### 2.2.1 Excitation, Shake-Up, Shake-Off

The ejection of a core electron results in a sudden change in the binding potential of outer electrons. This abrupt change can either excite additional electrons from their initial state to discrete excited states (*shake-up*) or eject them into the continuum (*shake-off*). This effect is described by *shake theory* [39], which is sometimes called the *sudden approximation* [40]. The *sudden approximation* is based on the assumption that for an instantaneous change in the Hamiltonian the transition from an initial state  $A_i$  to a final state  $A_f$  is

---



determined by the overlap integral of the wave function for the initial state  $A_i$  to the various possibilities of final states  $A_f$ .

The probability of removing one or more electrons through shake-off from an orbital with the quantum numbers  $n, l, j$ , with  $n$  and  $l$  being the principal and orbital angular-momentum quantum numbers and  $j = l \pm \frac{1}{2}$  is described by

$$P_{nlj} = 1 - \left| \int \Psi_{n^*lj}(A_f) \Psi_{nlj}(A_i) dr \right|^{2N} - P_F \quad (2.28)$$

where  $\Psi_{nlj}(A_i)$  and  $\Psi_{n^*lj}(A_f)$  describe the single-electron wave functions of the neutral atom and ion in the initial and final state respectively,  $N$  is the number of electrons occupying the orbital with quantum numbers  $nlj$ .  $P_F$  corrects for the finite probability of transitions to filled subshells and is given by

$$P_F = \sum_{n'=1}^{n'=x} N \frac{N'}{2j+1} \left| \int \Psi_{n^*lj}(A_f) \Psi_{nlj}(A_i) dr \right|^2 \quad (2.29)$$

where  $n' \neq n$  and  $N'$  is the number of electrons in the orbital assigned by the quantum numbers  $n'lj$ .

The neutral atom will be excited if the photon energy is less than the ionization threshold of the affected bound state or the ejected electron has a reduced kinetic energy and the ion is additionally excited.

This behavior is described by the following

$$\hbar\omega + A \rightarrow A^* \quad (2.30)$$

$$\begin{aligned} \hbar\omega + A &\rightarrow A^{*+} + e_{photo}^- \\ E_{photo}^{kin} &= \hbar\omega - (\Delta E_f^i + E_b) \end{aligned} \quad (2.31)$$

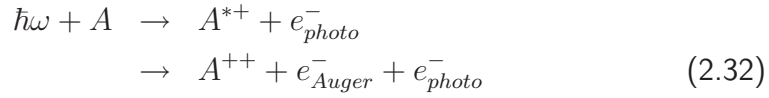
where  $\Delta E_f^i = E_{initial} - E_{final}$  is the energy necessary for the excitation, and  $E_b$  the binding energy of the ejected *photoelectron*.

## 2.2.2 Auger and Resonant Auger decay

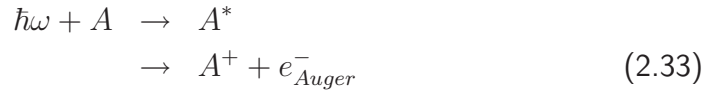
The creation of an inner-shell vacancy leaves an atom in an unstable state which will decay through a radiative transition or a radiationless transition with ejection of one or more electrons.

---

The *Auger decay* discovered by *Pierre Auger* in 1923 is a radiationless deexcitation process. In the case of photon impact the creation of the inner-shell vacancy is treated to be much faster than the lifetime of the inner-shell hole. Therefore, it is reasonable to describe the Auger electron ejection in two independent steps. In the first step a *photoelectron* from an inner-shell is emitted and in the second step the inner-shell vacancy decays with the ejection of one or more electrons, according to Eq. (2.31). This requires at least that the binding energy of the electron from the vacancy exceeds the double ionization threshold to initiate the second step.



Auger decay is not necessarily connected to the creation of a photoelectron in the first step. Another possible channel is described by Eq. (2.30). The incident photon produces an inner-shell vacancy and lifts the electron to high excited state without ejection of the electron resulting in a highly excited neutral atom. In this case the photon matches a transition in such a way that an excited neutral atom will decay by emission of an *Auger electron*. This process is known as the *resonant Auger decay*.



If the Auger process can be treated as a two step process the transition rate is given by [41]

$$\Gamma = \frac{2\pi}{\hbar} |\langle \Psi_i | \mathcal{H} - E | \Psi_f \rangle|^2 \quad (2.34)$$

where  $\Psi_i$  and  $\Psi_f$  are the many-electron wave functions in the initial and final states of the Auger decay respectively.  $E$  is the total energy of the final state and  $\mathcal{H}$  is the full electronic Hamiltonian.

In contrast to the kinetic energy of the emitted *photoelectron*, the kinetic energy of the *Auger electron* does not depend on the photon energy. The linewidth and energy are determined by the ionized inner-shell vacancy and the inner-atomic transition filling this vacancy. The total width of an Auger line and of an energy level in general is given by the sum of the partial width of all processes by which the level can decay [42, 43]

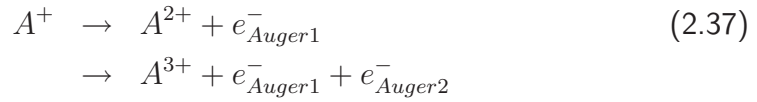
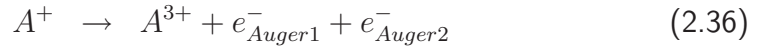
---

$$\Gamma_{total} = \sum_j \Gamma_j \quad (2.35)$$

where  $j$  determines all possible decay channels of the initial vacancy.

### 2.2.3 Nature of decay cascades

Beyond the "normal" Auger decay the ionization of deep inner shells can lead to the emission of two or more Auger electrons, if total energy of the ionized or excited atom exceeds the threshold of higher ionic charge states. The probability to produce these states due to inner-shell cascades followed by multiple electron emission increases. The emission of two electrons is either characterized by simultaneous (*double Auger decay*) or sequential (*cascade Auger decay*) ejection of both electrons.



In the case of a sequential Auger decay the stepwise model described above is extended by a further step for the emission of the second Auger electron. Concerning the lifetime of the inner-shell vacancy the stepwise decay with ejection of two Auger electrons requires a sufficiently long lived intermediate level. If this level is non-existent the two electrons are emitted simultaneously.

For the sequential Auger decay the emitted electrons appear in the continuum with discrete kinetic energies, where each kinetic energy of the emitted Auger electron is determined by the energy difference of the transition filling the vacancy ( $E_{transition}$ ) and the binding energy of the ejected electron ( $E_{Bind}$ ) following

$$E_{kin}^{Auger} = E_{transition} - E_{Bind} \quad (2.38)$$

If the intermediate level is non-existent and both electrons are emitted simultaneously they share the total energy released in filling the vacancy. In obtaining electron spectra for this process, the measured electrons cover a range from zero kinetic energy to the maximum energy released. In the extreme case the emission of a zero kinetic energy Auger electron and a fast Auger electron occurs. The simultaneous emission of two electrons shows an interesting possibility for the interpretation because it is indistinguishable from the sequential case emitting

---

a fast electron in the first step and a zero kinetic energy electron in the second step as discussed by *Lablanquie et al.* [44].

In this thesis data presented in chapter 5 contains both single and sequential decay channels. These processes are under observation regarding the time constants of population and depletion of subsequent levels involved.

## 2.3 Atomic Lifetimes

The measurement of atomic lifetimes has been of great interest from the beginning of the last century, influenced by the work of *Pierre Auger (1925)* [2] and *Coster and Kronig (1935)* [45] with many experiments carried out in the 1960s [43] and 1970s [42].

The timescale of atomic processes spans a wide interval of lifetimes from a few thousand seconds in the case of radiative lifetimes of highly excited *Rydberg states* [46, p. 5] over seconds and fractions of seconds for metastable states in rare gas atoms [47] down to the *attosecond* ( $10^{-18}s$ ) scale [42, 48, 49].

When discussing inner atomic decay or ionization dynamics in the context of attosecond time resolved pump-probe measurements, it has to be mentioned that all measurements of atomic lifetimes are based on the statistical analysis of atomic linewidth obtained from *electron or fluorescence spectroscopy* or similar techniques.

These previous measurements were performed in the energy domain and determine the lifetimes of atomic states by means of the "width" or the transition rate of an atomic level  $\Gamma$ .

Let the total transition probabilities per unit time for a state  $a$  be  $p_a^R$  for the radiative transitions and  $p_a^A$  for Auger transitions, then the mean lifetime of the state  $\tau_a$  is given by [50]

$$\tau_a = \frac{1}{(p_a^R + p_a^A)} \quad (2.39)$$

Based on the uncertainty principle one would expect an inherent uncertainty in measurement of the energy of state  $a$ . Thus the energy of level  $a$  is not sharply determined, but spread over an energy range

$$\Gamma_a = \hbar \cdot (p_a^R + p_a^A) \quad (2.40)$$


---

from the uncertainty  $\tau_a \Gamma_a \doteq \hbar$ .

Therefore, the total width  $\Gamma_{total}$ , Eq. (2.35), of an *Auger transition* from level  $a$  to level  $b$  is given by the sum over all possible Auger transitions filling the inner-shell vacancy. Radiative contributions are neglected because radiative transition of sub-valence shells in light atoms that are considered in this work are comparably weak [51] and not accessible for the experiment presented. Furthermore, the lifetime of the initial state following an electron ejection is reflected in the time dependent ion yield of the final ionic state, because it depends only on the decaying inner-shell vacancy.

Regarding 2.2.1, the lifetimes of excited or shake-up states are comparably long and typically in the range of hundreds of *ps* to *ns*. If such a state is populated once, any inner atomic dynamics is beyond the range of attosecond experiments for technical reasons based on the fact, that the maximum time window that can be covered is in the order of 600 *fs*. Since these states are comparably long lived on a sub-femtosecond timescale and created by photoionization with a few-hundred attosecond XUV pulse, depopulation of these states due to ionization with a laser electric field images field dependent dynamics referring to Eq. (2.15).

In recent years substantial efforts were made to study dynamics of the double and cascade Auger decay. In the case of xenon, measurements were made utilizing electron-electron coincidence resolving the partial width of the Auger lines in the electron spectrum [44].

These measurements are performed in the energy domain and extract time information from linewidths of the electron spectra obtained. In the case of the second step Auger decay this is a challenging problem, because the intermediate state is filled with a time constant given by the initial Auger decay and depleted with another time constant for the second step Auger decay. Therefore, the transition rates of the intermediate states filled by the first Auger decay depends on the energy of the level and is generally not directly accessible since the second step decay can follow different relaxation mechanisms.

The benefit of the new technique established in the thesis is that time-resolved measurement of population and depopulation of electronic states by means of the final ionic state is independent of the binding energy of this intermediate state. Therefore, it is sensitive to both time constants, each being separately the sum of all possible contributing channels. At the same time this is the main limitation of the technique, because it integrates over all levels populated by first step Auger transitions that can be ionized with the laser pulse.

---

## 2.4 Generation of femtosecond few-cycle laser pulses and isolated attosecond XUV pulses

First a short introduction on the mathematical formulation required to describe laser pulses and their behavior propagating will be given. After that the generation of ultrashort laser pulses and attosecond XUV pulses with respect to 2.1.5 is discussed.

### 2.4.1 Femtosecond laser pulses - a mathematical description

A light pulse is a superposition of plane waves with different wavelengths and a well defined frequency depending phase-relation. Such a pulse can be described in the form

$$\tilde{E}(t) = \frac{1}{\sqrt{2\pi}} \int_{-\infty}^{+\infty} E(\omega) e^{i\varphi(\omega)} e^{-i\omega t} d\omega \quad \text{using} \quad \tilde{E}(\omega) = E(\omega) e^{i\varphi(\omega)} \quad (2.41)$$

where  $E(\omega)$  is the real valued amplitude of the electric field and  $\varphi(\omega)$  the frequency-dependent phase of the complex valued amplitude  $\tilde{E}(\omega)$ .

Generally, the frequency dependent phase relation  $\varphi(\omega)$  can be decomposed in a Taylor expansion about the central or carrier frequency  $\omega_0$  [52]:

$$\begin{aligned} \varphi(\omega) &= \varphi(\omega_0) + \varphi'(\omega_0) \cdot (\omega - \omega_0) \\ &+ \frac{1}{2} \varphi''(\omega_0) \cdot (\omega - \omega_0)^2 \\ &+ \frac{1}{6} \varphi'''(\omega_0) \cdot (\omega - \omega_0)^3 \dots \end{aligned} \quad (2.42)$$

One can see that the shortest achievable pulse for a given spectral bandwidth is a pulse with a linear phase dependence  $\varphi(\omega)$  suppressing any higher order term of Eq. (2.42). This limit can only be achieved by Gaussian time and spectral envelopes of a femtosecond pulse [53] and is said to be *Fourier-limited*. The action of a linear optical system can be treated as the convolution of the impulse response function  $S(t)$  with the femtosecond light pulse  $E(t)$ .

---

$$\mathcal{E}_{out}(\omega) = S(\omega) e^{i\varphi(\omega)} \mathcal{E}_{in}(\omega) \quad (2.43)$$

where  $\mathcal{E}_{in}$  and  $\mathcal{E}_{out}$  represent the complex valued spectral amplitudes of the in- and out-going electric field, thus a linear optical system changes the spectral amplitude of the electric field by  $S(\omega)$  and introduces a phase-shift  $\varphi(\omega)$  described by Eq. (2.42). According to the first order term of Eq. (2.42) a pulse propagating through a medium of length  $L$  accumulates a frequency dependent group delay. This group delay can be written as

$$T(\omega) = L \frac{dk}{d\omega} = -\frac{d\varphi}{d\omega} \quad (2.44)$$

where  $k$  is the real part of the complex wave vector and is related to the refractive index by

$$k(\omega) = \frac{n(\omega)\omega}{c} \quad (2.45)$$

The second order term of Eq. (2.42) describes pulse broadening of a former *Fourier-limited* femtosecond pulse of a given bandwidth  $\Delta\omega$ . This term is called the *group velocity dispersion (GVD)* [53]. It represents the frequency depending change of the *Group Delay*.

$$\frac{dT(\omega)}{d\omega} = L \frac{d^2k}{d\omega^2} = -\frac{d^2\varphi}{d\omega^2} \quad \mathbf{GVD} \quad (2.46)$$

The third order term of Eq. (2.42) results in an asymmetric temporal stretching of a former *Fourier-limited* femtosecond pulse and is called **Third Order Dispersion**.

## 2.4.2 Optical elements of a few-cycle laser system

The optical elements of a few-cycle laser system can be summarized by the *GVD* and *TOD*. Propagation through a glass plate and the combination of a pair of prisms define the basis of the optical elements needed to describe such a system. A specialty of those systems is the use of chirped mirrors that can compensate even for high order dispersion terms of Eq. (2.42) by reflection from a stack of dielectric layers alternating in thickness.

### Propagation through a dispersive element

A femtosecond laser pulse that propagates through a dispersive element will experience *GVD* caused by angular dispersion [54]. The phase delay corresponds

---

to the angle between the frequency depending angle  $\alpha$  and the propagation distance  $L$  in relation to the frequency  $\omega$

$$\varphi(\omega) = \frac{\omega}{c} L \cos \alpha(\omega) \quad (2.47)$$

This gives the expressions for *GVD* and *TOD* by two- and threefold derivation of Eq. (2.47) at the carrier frequency  $\omega_0$ .

$$\varphi''(\omega)|_{\omega_0} \approx -\frac{L\omega_0}{c} \left( \frac{d\alpha}{d\omega} \Big|_{\omega_0} \right)^2 \quad \text{for } \sin \alpha \ll 1 \quad \text{GVD} \quad (2.48)$$

$$\varphi'''(\omega)|_{\omega_0} \approx -\frac{3L}{c} \left[ \left( \frac{d\alpha}{d\omega} \right)^2 + \omega \frac{d\alpha}{d\omega} \frac{d^2\alpha}{d\omega^2} \right] \Big|_{\omega_0} \quad \text{TOD} \quad (2.49)$$

### Propagation through a sequence of prisms

If we want to minimize *GVD* we also want to avoid beam divergence introduced by angular dispersion. In this case one of the most common choices is the use of a sequence of prisms. To achieve a minimum of reflection losses a pair of *Brewster* prisms is used for the calculations of *TOD* and *GVD* combined in the way shown in Fig. 2.5. In the *Brewster* case the *GVD* for a prism can be given by [54]

$$\varphi''(\omega_0) \approx \frac{\lambda_0^3}{2\pi c^2} [Ln'' - 4ln'^2] \quad (2.50)$$

where  $L$  is the propagation length of the beam in the prism material leading to positive *GVD* and  $l$  is the separation of the two prisms along the path of the carrier frequency  $\omega_0$  leading to negative *GVD* [55]. A prism sequence can be used to tune the *GVD* by changing the propagation path length  $L$  in the prisms' material. This can be achieved by translation of the prism perpendicular to its base.

The expression for *TOD* is given by derivation of Eq. (2.50). This leads to

$$\varphi'''(\omega_0) \approx \frac{\lambda_0^4}{(2\pi c)^2 c} [12l(n'^2[1 - \lambda_0 n'(n^{-3} - 2n)] - L(3n'' + \lambda_0 n'''))] \quad (2.51)$$

Comparing Eq. (2.50) and Eq. (2.51) one can see that increasing the propagation path length  $L$  will increase *GVD* and at the same time decrease *TOD* and vice versa. According to these calculations passing two pairs of prisms or double

---



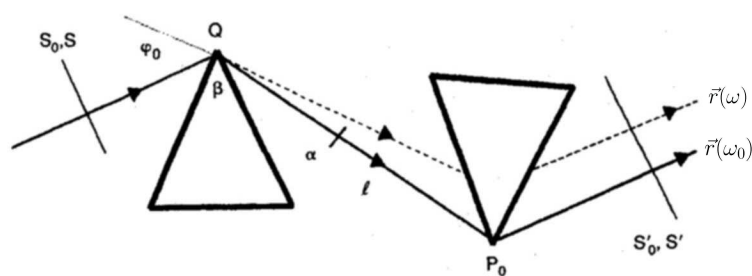


Figure 2.5: Two prism sequence introducing  $GVD$  without net angular dispersion [54]

passing one pair of prisms is often chosen to control  $GVD$ . Especially for the compensation of  $GVD$  introduced by propagation through linear media these setups are a good choice, because the  $GVD$  of prism pairs is in the same order of magnitude, has small losses and is easy to tune. Regarding a few-cycle laser system this setup is found to be the layout for the compression of the amplified and previously stretched pulses.

### Reflection from a chirped mirror

A third optical element is essential to generate ultrashort laser pulses which can be understood as a consequent development of the expressions given above. This element is the *dielectric chirped mirror* [56, 57].

Chirped mirrors can be manufactured and designed to correct for phase mismatches that are measured or at least well known. Nowadays they are manufacturable by desire and can correct for nearly arbitrary wavelength dependent phase mismatches.

### 2.4.3 Generating few-cycle laser pulses

Generally, a high power Ti:sapphire femtosecond laser consists of 4 basic parts following the scheme of *Chirped Pulse Amplification (CPA)* [5]:

- a *master oscillator* generating fs pulses
- a *stretcher* stretching the fs pulses for amplification
- a *amplifier* increasing the energy of the stretched pulses by multicycle amplification.

- a *compressor* transforming the amplified pulses back to the fs regime

In the case of few-cycle laser pulses the gain bandwidth [58] of the Ti:sapphire crystal does not support amplified sub 5 femtosecond pulses due to effects like *gain narrowing* during amplification, depending on the number of passes through the gain medium described by

$$g_{new} = g_{last} - \frac{p}{J_{sat}} \left( \frac{J_{out}}{T} - J_{in} \right) \quad (2.52)$$

In this expression  $J_{sat}$  is the saturation fluence of the gain medium,  $J_{in}$  the input fluence of the pulse entering the gain medium,  $J_{out}$  the output fluence after the actual pass. Furthermore,  $T = \exp(-L)$  is the single-pass transmission depending on the total cavity loss  $L$  and  $p$  is the gain recovery coefficient. For complete gain recovery  $p = 0.5$  and for no gain recovery  $p = 1$  [59]. Therefore, high power output is connected to decreasing spectral bandwidth. To overcome the problem of gain narrowing and support the necessary bandwidth for sub 5 femtosecond pulse durations, amplified few-cycle laser systems use a gas filled hollow fiber for spectral broadening [60, 61]. Other concepts use similar principles, but without the waveguide relying on the formation of filaments in a pressurized gas cell [62]. Both of these techniques are connected with loss in the pulse energy in the order of 20-50% depending on the total transmission through the fiber or filament cell and the kind of gas used for spectral broadening.

The broadened spectrum must be recompressed which is done by a chirped mirror compressor in the system described here. Other schemes make use of a pair of prisms referring to Fig. 2.5. Figure 2.6 shows the generalized scheme for a CPA few-cycle laser system. For a more detailed description of the main principle refer to [63, 64].

An essential detail for the generation of isolated attosecond pulses in the *cutoff region* of the harmonic spectrum is the possibility to stabilize the *Carrier Envelope Phase (CEP)* of the driving few-cycle laser pulse. In recent years this technique arised to be state of the art and the techniques behind this were honored with the Nobel Award in physics for T. W. Hänsch. Nowadays, CEP stabilized laser systems are commercially available. A layout and brief description of the stabilization loop is shown in 3.1. For a detailed description of the principle for the specific system used refer to [65].

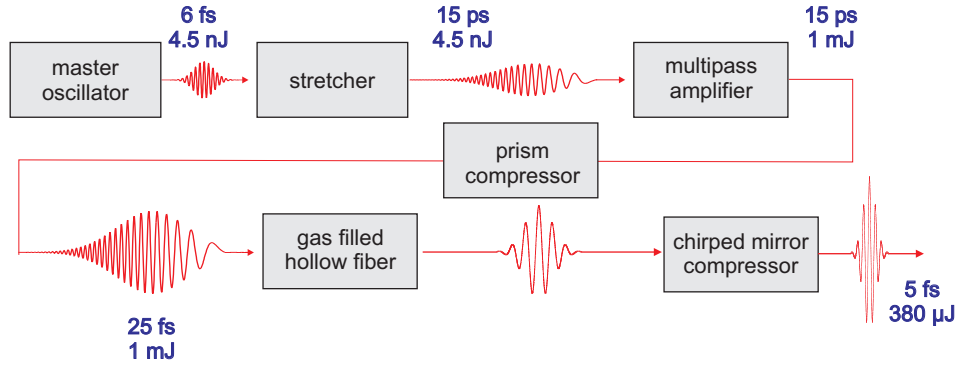


Figure 2.6: Scheme of the 3kHz femtosecond laser system used during this thesis; for details see [i02]

## 2.4.4 Generation of isolated attosecond pulses

Generation of isolated attosecond pulses is the main task to perform experiments directly following a two color pump probe scheme for time resolved measurements as will be explained in the next section.

The basis for the creation of a single attosecond pulse is the generation of a continuum with a sufficient bandwidth and a well defined phase-relationship regarding Eq. (2.42). Regarding the quantum mechanical model in 2.1.5, two different quantum paths belong to the generation of a single harmonic with long and short trajectories regarding their time propagating in the laser electric field. The relative phase of the harmonics has been measured by Mairesse *et al.* [66] describing the phase mismatch in a broad spectral range.

In the *cutoff range* the difference between the trajectories becomes meaningless and a continuum with a bandwidth determined by the pulse duration of the driving laser pulse is generated. The bandwidth of the *cutoff continuum*  $\Delta(\hbar\omega)$  is expressible by the ratio of the neighboring electric field amplitudes given by [67]

$$\Delta(\hbar\omega) = (\hbar\omega_{cutoff} - I_p) \frac{\Delta I_{peak}(t)}{I_{peak}^{max}(t)} \quad (2.53)$$

In this expression  $\Delta I_{peak}(t)$  is the intensity difference for subsequent sub-cycles of the pulse and  $I_{peak}^{max}(t)$  the intensity of the strongest one.

It follows that to increase the *cutoff bandwidth* for a constant drive laser carrier frequency requires decreasing the drive laser pulse duration. The bandwidth

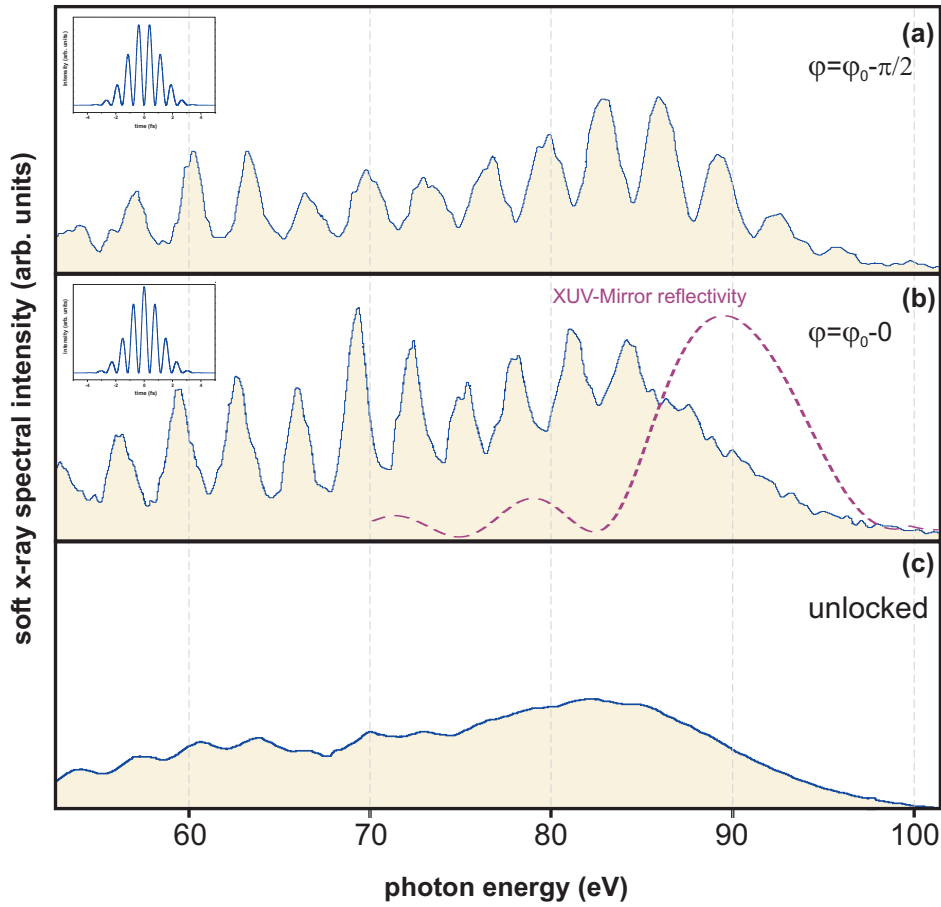


Figure 2.7: High Harmonic Spectra for three different situations (a) sine pulse, (b) cosine pulse and (c) unlocked; the small insets represent the intensity distribution for 5 fs sine- and cosine pulse respectively; the reflectivity curve of the XUV mirror used in the experiment is shown as an overlay in the HHG spectrum for the cosine pulse. The spectra are taken from [68] and the energy axis is modified to match the given experimental conditions here

for radiation resulting from a single recombination path in the high energy *cutoff* is extended and can be explained by means of an increasing contrast ratio  $\Delta I_{peak}(t)$  of the neighboring subcycles of the electric field in relation to Eq. (2.53).

Figure 2.7 shows the different behaviors in the *cutoff region* for a *sine* and a *cosine* CEP stabilized laser pulse with a duration of about 5 fs and an initial CEP of  $\varphi = \varphi_0$  being a *cosine*. For a *sine* pulse the *cutoff region* is small and distorted. The reason for this is that the neighboring intensities close to the peak of the envelope are identical, as depicted by the small inset representing

the intensity distribution of the pulse. As a consequence, for a *sine* pulse there are two identical intensities that tunnel-ionize an electron with a time delay  $\Delta\tau$  determined by a half-cycle of the optical field. For a given *cutoff energy* a *sine* pulse ends up in the creation of two attosecond pulses shifted by  $\pi/2$ . In the spectrum of the *cosine* pulse the reflectivity of the XUV mirror in use for the experiment is shown as an overlay to denote how the isolated attosecond pulse is filtered from the complete *HHG* spectrum.

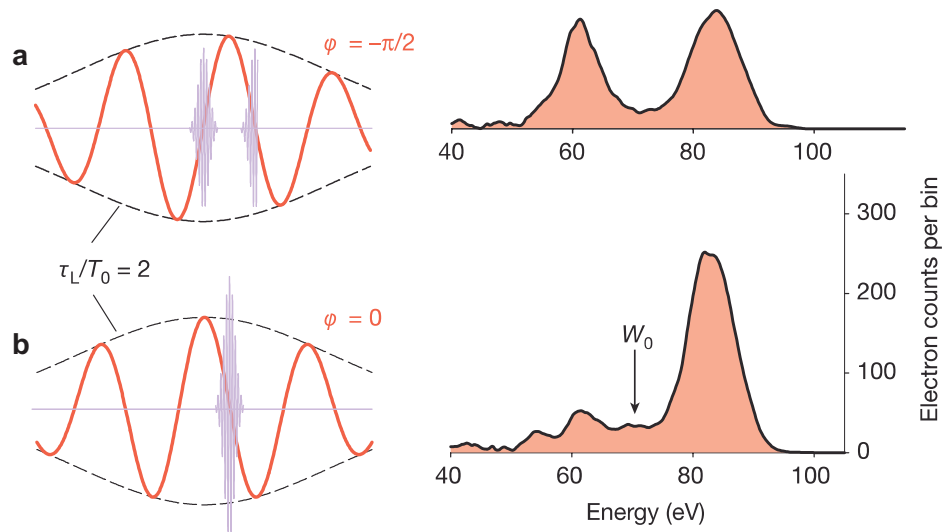


Figure 2.8: phase dependence of the attosecond pulses filtered by the XUV mirror; streaked photoelectron spectra recorded at a fixed delay of probe laser light. Energy distribution of photoelectrons emitted from neon atoms excited by a sub-fs XUV pulse [8]

In Fig. 2.8 the behavior of the XUV photoemission of neon in presence of an additional laser field is demonstrated (streaking geometry [12]). The additional momentum, given by the applied IR laser field to the free electron, results in a splitting of the photoemission line because the electrons are produced with a time delay within the laser pulse. Thus for a fixed delay the momentum transferred to the electron created by the first XUV pulse is different from that created by the second XUV pulse. For a *cosine CEP* a clean photoemission line as a convolution of the wavelength dependent ionization cross-section, the mirror reflectivity and the slope of the *cutoff spectrum* is resolved.

In the last decade a new technique isolating single attosecond pulses came of age. This technique is called optical polarization gating and is based on the idea that the electron ionized from the gas producing the harmonics will only

recombine with the core, if the laser electric field is linear polarized. This means for circular polarized light the electron will never recombine and create ATI only. In this sense the initial pulse creating the High Harmonics is split into two pulses. Both circular polarized, but with opposite orientation. Overlapping both pulses creates a subfraction that is virtually linear polarized where the electron can recombine and create High harmonics. The fraction can be adjusted by delaying one pulse with respect to the other, or changing the degree of rotation slightly.

Using this method Sansone *et al.* [18] recently demonstrated isolated attosecond pulse durations down to 130 as. This method can provide a stable attosecond source, but it requires *CEP* stabilized laser pulses. One benefit of the polarization gating method is the generation of the pulse without applying any bandpass filter like the XUV mirror. On the other hand it is connected to a tremendous loss in energy and from this follows that currently photon energies in the 90 eV need more intense laser sources which are under development, but not available right now or have a repetition rate much less than 1 kHz that make some experiments impossible for reasons of long term stability.

## 2.5 Principle of time resolved pump-probe measurements

To observe ultrafast dynamics directly in the time domain the so-called *pump-probe technique* can be utilized [69, 70, 71, 10, 37].

Initially, the system of interest is optically excited into unoccupied states with a pump pulse. Once the electronic configuration of the system has been changed the relaxation back to equilibrium is defined by the characteristic time constants for the relaxation processes associated with the excitation caused by the pump pulse.

A probe pulse with variable time delay  $\tau_d$  with respect to the pump pulse takes a snapshot of the changes in the relaxing system in terms of the detection of electrons, ions or photons as the response function at the moment  $\tau_d$  after the pump pulse. Scanning the delay between the pump pulse and the arrival of the probe pulse, allows us to follow the relaxation dynamics by means of the physical quantity measured.

---

Let us assume the response function of the system which reflects the relaxation back to equilibrium is given by  $f(t)$  after excitation with an infinitely short pump pulse  $\delta(t)$ . Then the complete response of the system  $R(\tau_D)$  is given by the convolution with the temporal intensity profile  $I_{pump}(t)$  of the pump pulse in the following form [54, 37]

$$R(\tau_D) = \int_{-\infty}^{+\infty} I_{pump}(t - \tau_D) \cdot f(t) dt \quad (2.54)$$

and for the corresponding Fourier transform

$$\tilde{R}(\omega) = \tilde{I}_{pump}(\omega) F(\omega) \quad (2.55)$$

The measured signal  $S(\tau_D)$  is now "gated" by a time delayed probe pulse that has a temporal intensity profile  $I_{probe}(t)$ . Thus  $S(\tau_D)$  is expressed as the convolution of the systems response  $R(\tau_D)$  with  $I_{probe}(t)$  which leads to

$$S(\tau_D) = \int_{-\infty}^{+\infty} I_{probe}(t - \tau_D) \cdot R(t) dt \quad (2.56)$$

and for the corresponding Fourier transform

$$\tilde{S}(\omega) = F(\omega) \tilde{I}_{pump}(\omega) \tilde{I}_{probe}(\omega) \quad (2.57)$$

Equation (2.56) defines the shape of the measured response. If the pump and probe function are delta like functions it becomes obvious that the response of the relaxation is directly measured. If the response is a delta like function, expression (2.56) reduces to a cross-correlation of the pump and probe function.

In practise there are several schemes for pump-probe measurements that allow observation of many physical observables. Most of them require that the intensity of the probe pulse is much smaller than that of the pump pulse to ensure that the probe pulse does not affect the relaxation dynamics of the system.

The special schemes of pump-probe spectroscopy to focus on in this thesis are based on photoelectron and ion spectroscopy and give a direct insight to the transient change of the electronical structure after photoexcitation. In this special case the pulses become distinguishable due to their different photon energies, as shown in section 2.4. These schemes have been applied in several

---

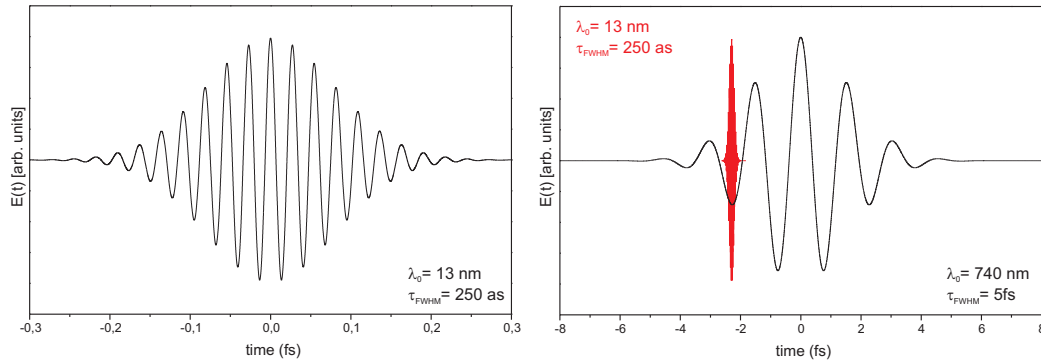


Figure 2.9: development of  $E(t)$  for a Fourier transform limited 250 as XUV pulse (left) and for a Fourier transform limited 5 fs IR pulse (right). The red inset on the right hand side depicts the temporal relation of both pulses.

experiments and for different timescales [72, 73, 69, 74, 37]. For all these measurements it is common that the applied pump and probe functions are nearly of the same duration and comparably long meaning that those pulses are far away from the few-cycle limit. In this sense the time resolution and the objects under observation are mainly determined and restricted by the envelope of the pump or probe pulse.

In the experiments described in this thesis we will use attosecond pump-probe techniques, Eq. (2.56) is appropriate to describe the general behavior but, depending on the experiment, the dynamics under observation is sampled with a few-cycle laser pulse and an attosecond XUV pulse. From Fig. (2.9) one can see that the substructure of the IR pulse has to be taken into account because the XUV pulse is even shorter than one half-cycle of the IR pulse. This leads e. g. to the possibility of sampling the electric field of the IR laser pulse directly [12]. As a result of the field dependence, the *CEP* of the IR pulse becomes of importance for the response of the system and needs to be taken into consideration.

Figure 2.10 gives a brief overview of the atomic processes that could be probed with XUV-pump and IR-probe pulse by detection of electrons or ions. In case *a*, the XUV produced photoelectron experiences an additional momentum from the probing IR laser field [12, 10]. In case *b*, a core level electron is emitted. Again the electron might gain an additional momentum from the IR laser field, but because it is a core hole, an Auger decay *c*, results in an emission of a second electron which is determined by the decay time constant of the Auger decay to appear in the continuum [11]. For the cases *d* and *e* we assume that



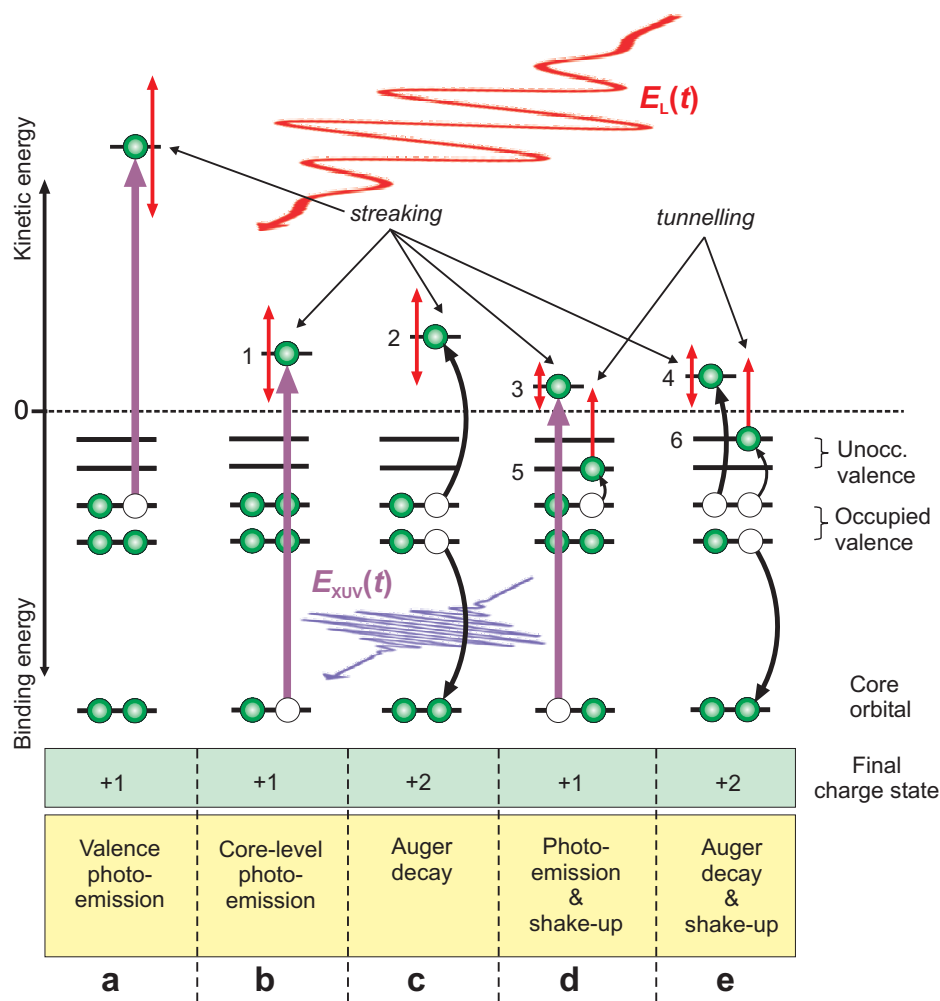


Figure 2.10: Probing electron motion with attosecond sampling techniques. A sub-fs XUV pulse triggers electron dynamics by inducing valence (process *a*) or core photoelectron emission (process *b*). The temporal evolution of photo- and Auger electron emission (process *c*) can be probed via attosecond streaking to retrieve the triggering XUV pulse or the sampling laser field and trace inner-shell relaxation dynamics, respectively. XUV photoexcitation as well as subsequent Auger decay processes are usually accompanied by shake-up of another electron to a previously unoccupied level (processes *d* and *e*). For sufficiently strong laser probing laser fields, the shake-up electrons can be liberated by tunneling ionization. The temporal evolution of the tunneling current will provide information about inner-atomic electron dynamics that populate and/or depopulate the interrogated shake-up states and the duration of the process that populated the levels on a sub-fs timescale. Note that the final charge state of the residual ion given in this figure increases by attosecond tunneling while it remains unchanged in case of attosecond streaking.

the occupied valence electrons are not accessible by the IR laser pulse, but the excited valence electrons are. Case *d* shows the emission of a photoelectron connected with an excitation of a valence electron. The directly emitted electron gets again an additional momentum transfer from the IR laser field. Furthermore, the excited electron becomes accessible for the IR laser pulse and is ionized. This can happen due to tunnel ionization in the strong field or by multiphoton ionization. In case *e*, this process is connected with the Auger decay of an inner-shell vacancy which results in a shake-up of valence electrons to excited states that are accessible by the IR laser pulse.

The processes in *d* and *e* will be discussed in detail in chapter 5. The measurements are performed by means of ion spectroscopy and show a time-dependent population variation in the corresponding ion charge state, as shown in Fig. 2.10.

---

## Chapter 3

# Experimental Setup

Within the scope of this thesis a new apparatus for attosecond time resolved studies was developed and assembled based on the main principles and considerations discussed in [10]. The development and design of this new system focusses on the improvement of the old concepts described in [10] in two directions. The first is related to harmonic generation and beam guiding which is designed to ensure a high throughput from the high harmonic source to the experimental target. The second is the improvement of the background pressure in the target area towards UHV conditions. The requirements for the setup with respect to these considerations are defined by a desired working pressure for the *HHG* conversion in the  $\sim 10^{-3}$  mbar range to minimize reabsorption and a background pressure of  $\sim 10^{-9}$  mbar in the experimental environment.

For future experiments and new developments for the XUV mirrors towards higher photon energies as well as support of attosecond pulse durations  $<250$  as, the accuracy of the delay between the as-XUV pulse and the laser pulse must be improved. This will allow the highest possible resolution for future experiments with isolated as pulses  $<250$  as. To achieve vibration isolation of all components inside the vacuum from the vacuum pumps and other sources of noise the vacuum design must be improved.

These basic conditions led to the attosecond experimental system presented in Fig. 3.1 which was built and used for the measurements presented in this thesis and has been named *AS-1*.

---

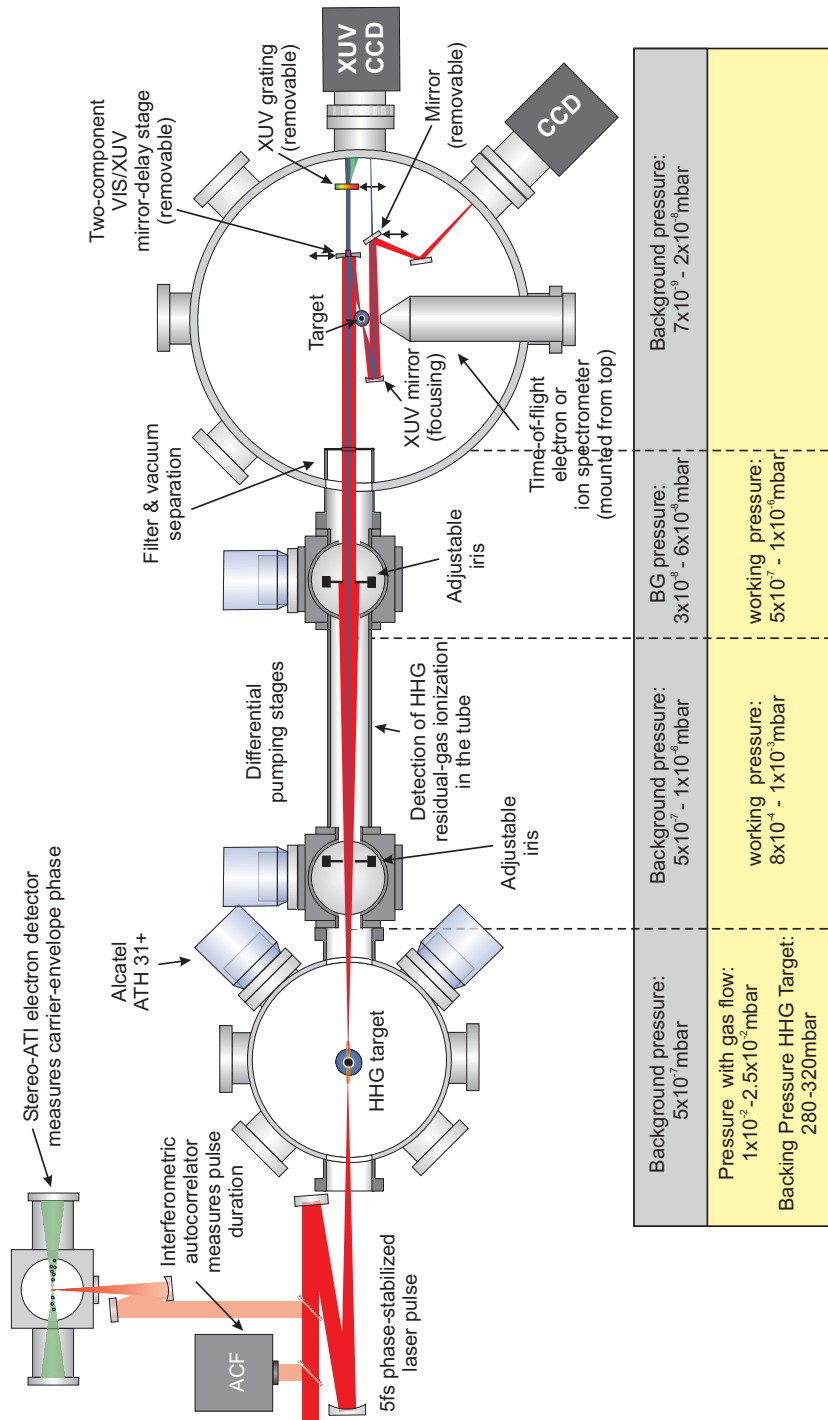


Figure 3.1: schematic drawing of vacuum, optical and diagnostic setup of AS-1

In the next section the AS-1 vacuum system shown in Fig. 3.1 is presented in detail. Only a brief overview of the driving CEP stabilized laser system is given because it is commercially available.

### 3.1 Laser System and Diagnostics

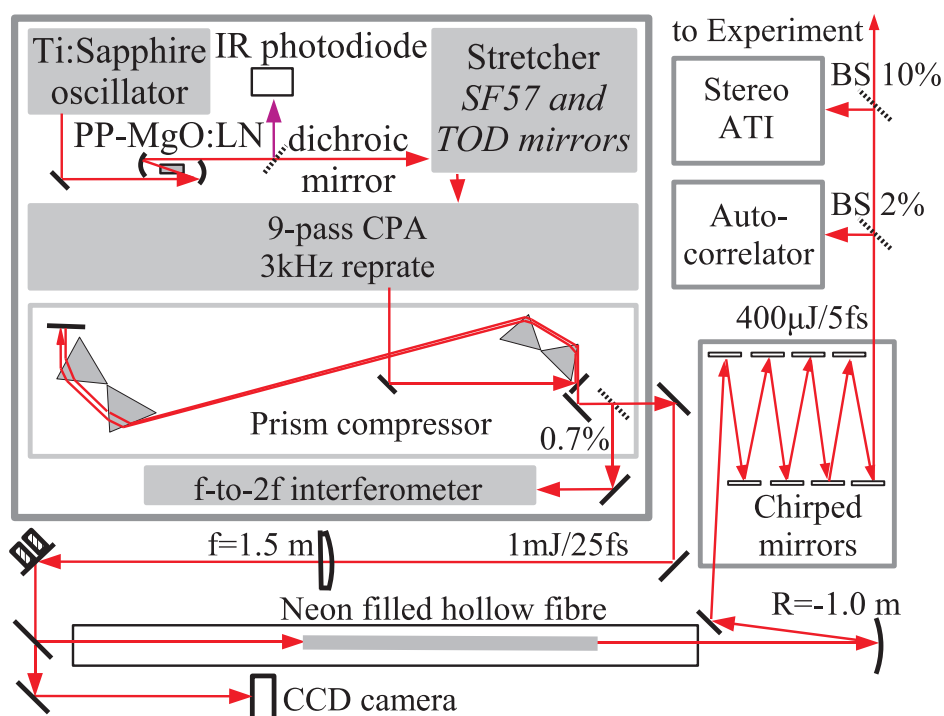


Figure 3.2: Schematic diagram of the 3 kHz few-cycle laser system

The laser system driving this experiment is based on a *Femtopower Compact PRO CE-Phase* delivering 25 fs,  $\sim 1$  mJ pulses centered at 740 nm with a repetition rate of 3 kHz.

To phase stabilize the pulses from the Ti:sapphire oscillator they are focused into a magnesium oxide-doped periodically poled lithium niobate (PP:MgO-LN) crystal for *difference frequency generation (DFG)* ( $f$ -to- $2f$ ) and *self-phase modulation (SPM)*. In the region of spectral overlap of the spectra corresponding to SPM and DFG an interferometric beat signal is detected that contains the carrier envelope phase offset and can be used for the stabilization of the Ti:sapphire oscillator. Because the region of spectral overlap is not covered by

the fundamental spectrum, it can be separated by a dichroic mirror acting as a beam-splitter for the spectral components. This concept was proposed by *Fuji et al.* [75].

In the next step the pulses are stretched to  $\sim 15$ ps for amplification and propagating through a SF57 glass block. The *Third Order Dispersion (TOD)* introduced by the stretcher and prism is compensated compressor by multiple reflections from specially designed *TOD* mirrors. The pulses are mainly *GVD* chirped.

Using a *multipass amplifier* with 9 passes the oscillator pulses are amplified with the full repetition rate up to the fourth pass. After the fourth pass one pulse is picked with a repetition rate of 3 kHz and amplified in the last 5 passes. The amplified pulses are compressed with a double pass prism compressor. Behind the prism compressor 0.7% of the energy is split to another f-to-2f interferometer for detecting slow phase drifts and delivering feedback for a secondary phase-lock loop. The amplified and phase stabilized pulses are then focused into a hollow fibre filled with 2 bar of neon to generate spectral broadening to support 5 fs pulses. The leakage of the last folding mirror coupling the focused beam into the hollow fiber is used to monitor beam pointing. Slow drifts are corrected a computer controlled motorized mirror using the camera image as a feedback. After the hollow core fiber the remaining phase mismatch is compressed by multiple reflections in a chirped mirror compressor, also pre-compensating the chirp introduced by propagation in air and passing the entrance window into the vacuum system. The pulses behind the chirped mirror compressor are characterized with a second order autocorrelator and the absolute phase is measured in a stereo ATI which can be used as additional feedback for the phase locking electronics [76]. Both devices give real-time information about the laser parameters during measurement.

## 3.2 Vacuum Layout and Vibration Control

In the layout and design of the vacuum system special care was taken to implement elements for vibration damping and isolation, since  $100 \text{ as}$  corresponds to a distance of  $30 \text{ nm}$ . Even if the double mirror assembly is virtually jitter free based on the construction both mirror mounts are not identical and have different vibration resonances and amplitudes. For this reason the optical breadboards inside the vacuum chambers are decoupled from the walls of the chambers, which support to the vacuum pumps by edge welded bellows with

---

posts inside. Using this concept the chambers and the optical tables inside are standing on separate posts mounted on the large optical tables in the lab which uses the damping capabilities of the large optical tables as well as damping vibrations between the posts.

The second thing implemented is a strict damping of the connected roughing pumps realized with "U" shaped flexible hoses covered with silica sand at a length of nearly 1 m.

Mechanical vibration in the apparatus becomes visible in the image of the laser focus as described later on. Without calibrated vibration measurements that need to be carried out, the mean lifetime of the harmonic target that needs to be replaced after some time, increased in comparison to the old system used by *Hentschel et al.* [7]. Therefore the efforts to reduce the transmission of external vibrations to the optical system in vacuum (including the *HHG* target) have already shown positive results in the stability of the experimental environment.

### 3.3 Vacuum System and Diagnostics

In the following section the beamline shown in Fig. 3.1 is explained, divided in the particular parts to focus on some detailed solutions to improve the experimental situations in this newly developed beamline. Refer to Appendix A for a technical vacuum layout.

#### 3.3.1 High Harmonic Generation

The *HHG* is based upon a neon filled nickel tube with a constant gas pressure inside the tube. To optimize the conversion efficiency of the *HHG* the propagation length is one of the important parameters. Figure 3.3 shows the efficiency as a function of length for a fixed pressure inside the tube. In the energy range of  $\hbar\omega \approx 90\text{eV}$  the conversion efficiency of *HHG* is in the range of  $10^{-7}$  to  $10^{-8}$ . Thus it becomes necessary to minimize reabsorption in the expanding gas jet.

For a propagation distance of 15 cm (diameter of the *HHG* chamber is 30 cm) the reabsorption must be minimized and at the same time most of the expanding gas jet efficiently pumped. Assuming only neon as the absorbing gas inside the chamber during conversion the reabsorption has to be taken into account for pressures  $> 10^{-3}$  mbar [i03]. Therefore the chosen turbo pumps (Alcatel ATH31+) were selected to support a high gas flow at sufficiently good vacuum pressure in the range of  $8 \cdot 10^{-3}$  mbar to  $2 \cdot 10^{-2}$  mbar under working conditions,

---

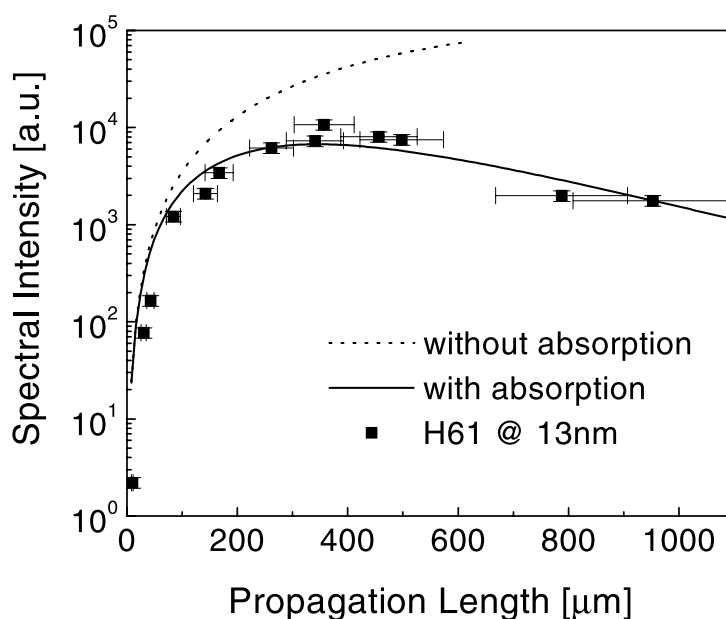


Figure 3.3: Evolution of the 61st harmonic (*squares* - measured, *lines* - computed) upon propagation in the neon target at a fixed pressure of 0.4 bar. The error bars depict systematic errors resulting from an uncertainty in estimating the effective interaction length. [77]

depending on the size of the source. By maintaining these conditions, only 2% of the *HHG* were reabsorbed before entering the first differential pumping stage (first cube in Fig. 3.1).

The pressure inside the nickel tube is controlled by a flow-controller (Pfeiffer EVR116) and monitored by a piezo electric membrane sensor (Sunx DPHA07) that is connected to a PC monitoring the actual pressure of the *HHG* target and can be logged if necessary.

### 3.3.2 Differential pumping and XUV detection

Two differential pumping stages are located between the *HHG* and experimental chamber for further beam guiding and pumping to achieve UHV-conditions in the experimental chamber.

The laser and the highly collimated x-ray beam emerging from the interaction region within the nickel tube co-propagate collinearly along the axis of the emission cone through a 1.60 m beamline toward the double mirror assembly.



The pressure gradient, achieved under working conditions by the two differential pumping stages shown in Fig. 3.1, is about 6 to 7 orders of magnitude. The pressure in the first stage is typically in the order of  $1 \cdot 10^{-3}$  mbar to  $8 \cdot 10^{-4}$  mbar and in the second stage  $1 \cdot 10^{-6}$  mbar to  $5 \cdot 10^{-7}$  mbar entering the experimental chamber.

An ionization detector between the two differential pumping stages of the beamline serves for monitoring the spectrally integrated high-harmonic flux. The measured current is converted into a voltage that is monitored by a PC and logged into a file during measurement.

The motorized iris in the first cube has three main functions. In a first instance it is used for beam alignment inside the vacuum, but more importantly it acts as a variable scattering aperture for the expanding gas jet. Thus to a certain amount the efficiency of the differential pumping in the first cube is adjustable due to this iris. Finally closing the iris too much reduces the background gas inside the ionization detector and decreases the signal.

The energy transported by the resulting annular laser beam to the experimental chamber can be adjusted with the second motorized iris located in the second cube. Typically the laser pulse energy is between a fraction of a microjoule and a few tens of microjoules. Energy attenuation is the primary function of this iris.

### **3.3.3 Experimental Chamber**

In the experimental chamber a background pressure in the range of  $8 \cdot 10^{-9}$  mbar to  $3 \cdot 10^{-8}$  mbar is usually achieved by vacuum separation between the second differential pumping stage and the experimental chamber.

Following the beam path the colinear propagating beams hit a removable double mirror assembly focussing the beams to the target under observation and in the desired distance in front of the detector.

Several diagnostics of the laser radiation as well as the XUV radiation are implemented in this setup and will be explained in the following text as well as the vacuum separation and the assembly of the double mirror.

#### **Vacuum Separation and Filter Slider**

A filter slider (Fig. 3.4) closes the end of the beamguide and acts as a complete vacuum separation between the second differential pumping stage and

---

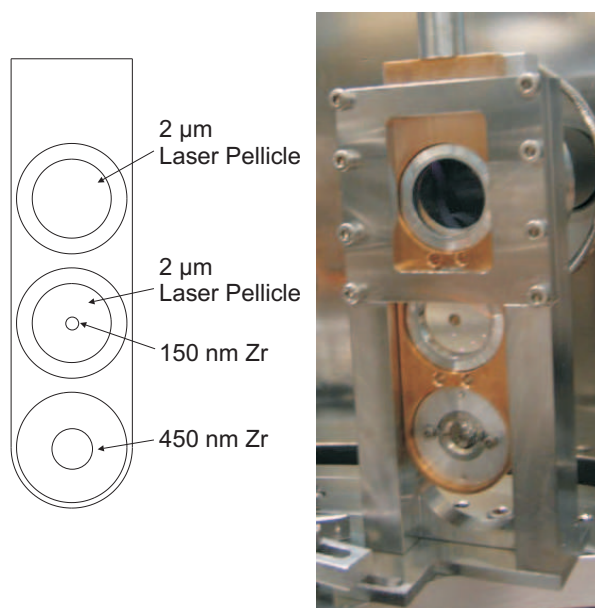


Figure 3.4: Slider for complete vacuum separation between the second differential pumping stage and experimental chamber.

experimental chamber. This slider has three insets that allow diagnostics of laser and XUV light without breaking the vacuum separation between the last cube and the experimental chamber (Fig. 3.1). The upper part is a  $2\ \mu\text{m}$  laser pellicle which transmits only the laser light to adjust the spatial and temporal overlap. Using this filter the XUV radiation is completely absorbed and the inner mirror illuminated by laser light, as well. The central inset allows to transmit both the laser and harmonic beam. The high harmonic radiation passes through a zirconium foil with a thickness of  $150\ \text{nm}$  and a diameter of  $5\ \text{mm}$  placed on a nitrocellulose pellicle with a thickness of  $2\ \mu\text{m}$  to cover a hole of  $5\ \text{mm}$  diameter. This double structured filter blocks the fundamental laser radiation in the central part but allows the XUV radiation pass through. At the bottom a zirconium filter with a thickness of  $450\ \text{nm}$  which suppresses the fundamental radiation completely allows XUV only diagnostics. The Z-folded geometry (Fig. 3.1) of the optical beampath is based on restrictions set by the various spectrometers that can be used with this apparatus such as the reflectron ion spectrometer in this study. Generally, the folding angle should be kept below  $5^\circ$  to minimize astigmatism. Spherical aberration in this use gives rise to a temporal resolution smearing of  $<0.05\ \text{fs}$  for the harmonic and  $<1\ \text{fs}$  for the laser beam.

### XUV/VIS Double Mirror Setup

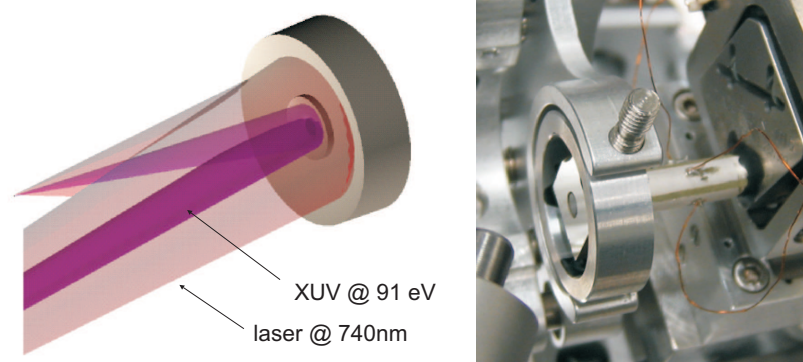


Figure 3.5: Double mirror Setup; inner mirror  $\rightarrow$  Mo/Si multilayer  $\lambda_0 \approx 90\text{eV}$ ; outer mirror  $\rightarrow$  silver mirror protective coated; both mirrors can be delayed with respect to each other

The main core of the experiment is realized by the double mirror assembly shown in Fig. 3.5. The mirror consists of an annular part that has an outer dimension of  $18 \times 18 \text{ mm}$  with a concentric hole of  $5\text{-mm}$  diameter hosting a miniature mirror of a slightly smaller diameter being a Mo/Si multilayer mirror reflecting the XUV radiation in normal incidence. Both parts originate from the same substrate, ensuring identical radii of curvature ( $R = 245 \text{ mm}$ ). The miniature central mirror is mounted on a closed loop controlled ultra high precision piezo translation stage (PI P-621.1CD) allowing alignment and translation with respect to the external component. This two-component mirror forms a compact, nearly jitter-free delay stage for the laser and the harmonic pulses and was improved to a maximum scan range of  $660 \text{ fs}$  and a reproducibility of better than  $3 \text{ attoseconds}$  with this new translation stage.

The mirror assembly has all necessary degrees of freedom to align the focus with respect to the spectrometer in use. It is mounted on a long range translation stage perpendicular to the beam axis to remove the mirror, a tilt and rotation stage to move the focus in a plane parallel to the spectrometer (the spectrometers are mounted from top). Another translation stage moves along the direction of the angle of incidence. Finally the tip and tilt axis of the outer mirror are motorized to align the spatial overlap of the foci with respect to each other.

## Laser Diagnostics

Using the upper inset of the filter slider the XUV radiation is blocked and both the inner and outer mirror are radiated by the laser beam. Performing diagnostics of the laser pulse the focus is imaged onto a CMOS camera by a lens with a magnification <sup>1</sup> of a factor of  $\sim 5$ . Figure 3.6 shows a typical image obtained using the upper inset of the filter slider. The small spot in the upper right is the image of the focus from the inner mirror, whereas the large image refers to the focus of the outer mirror with the iris in the second cube slightly closed to reduce the intensity contributed by the outer mirror.

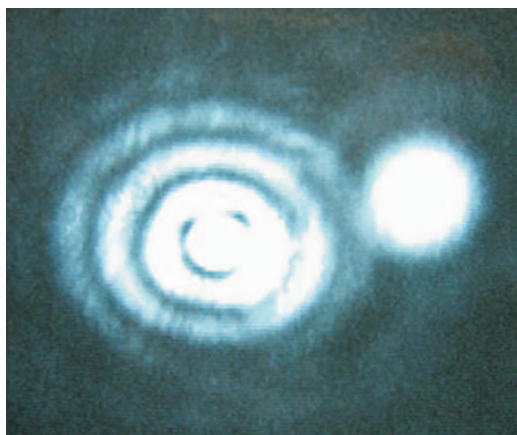


Figure 3.6: Magnified image of the focus. Left  $\rightarrow$  outer mirror; right  $\rightarrow$  inner mirror; the focus of both mirrors is displaced for demonstration purposes

If both mirrors reflect approximately the same intensity, the pulse overlap in time and space can be found by observation of clean interference fringes. In the first step, the translation stage that the inner mirror is mounted on (the "delay" stage) is moved until interference fringes appear. In the second step the angle of the outer mirror is adjusted until the image is symmetric. The image of the focus is monitored during, and throughout every measurement and the relative laser intensity is measured with a silicon photodiode which uses a front side reflex of a thin window.

---

<sup>1</sup>just for completeness it is worth to mention that a set of two mirrors exist, that allow diagnostics of the reflected XUV beam, which has not been used so far. This is the setup shown in Fig. 3.1. Currently the imaging mirror is replaced with an achromatic lens and a wedge using the front side reflex like a mirror.

---

In general, all these diagnostics can be recorded. Typically, only the relative intensity is recorded to obtain information on intensity fluctuation during a measurement. The image of the focus is only shown on a monitor, but could be connected to a framegrabber for spotsize analysis.

### XUV Diagnostics

For direct monitoring of the XUV beam, the third inset of the slider with the 450 nm zirconium filter is used. The double mirror is moved out of the beam path and the XUV beam propagates to the back-thinned CCD camera (*Princeton Instruments LCX400*). This camera is located 572.5 mm behind the mirror and 480 mm behind a freestanding transmission grating that is mounted on the same linear translation stage.

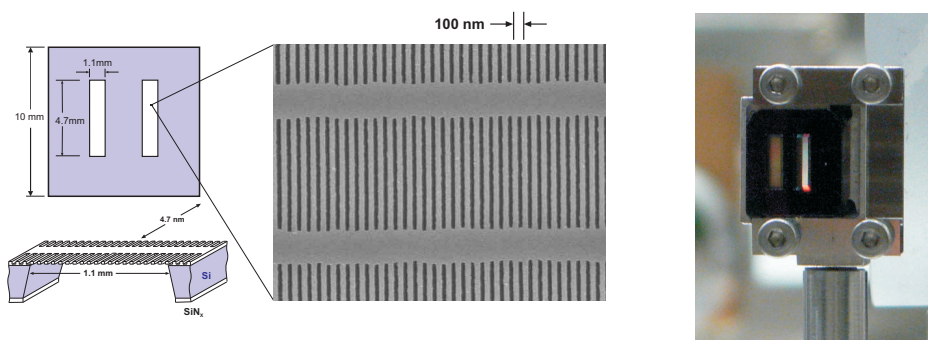


Figure 3.7: freestanding silicon nitride grating with 10000 lines/mm (by courtesy of T. A. Savas [78])

To adjust the *cutoff* in a way that it meets the XUV mirror reflectivity, the freestanding transmission grating (Fig. 3.7) is moved into the XUV beam. The resolved *HHG* spectrum, as shown in Fig. 4.4. A spectrum like this is routinely used to meet the XUV mirror's reflectivity and select a single isolated attosecond XUV pulse.

## 3.4 Experimental Environment

The data acquisition environment of the presented beamline is determined by the monitoring, control and automation of the parts described above and the characteristics of the detector and data-acquisition for the actual experiment.

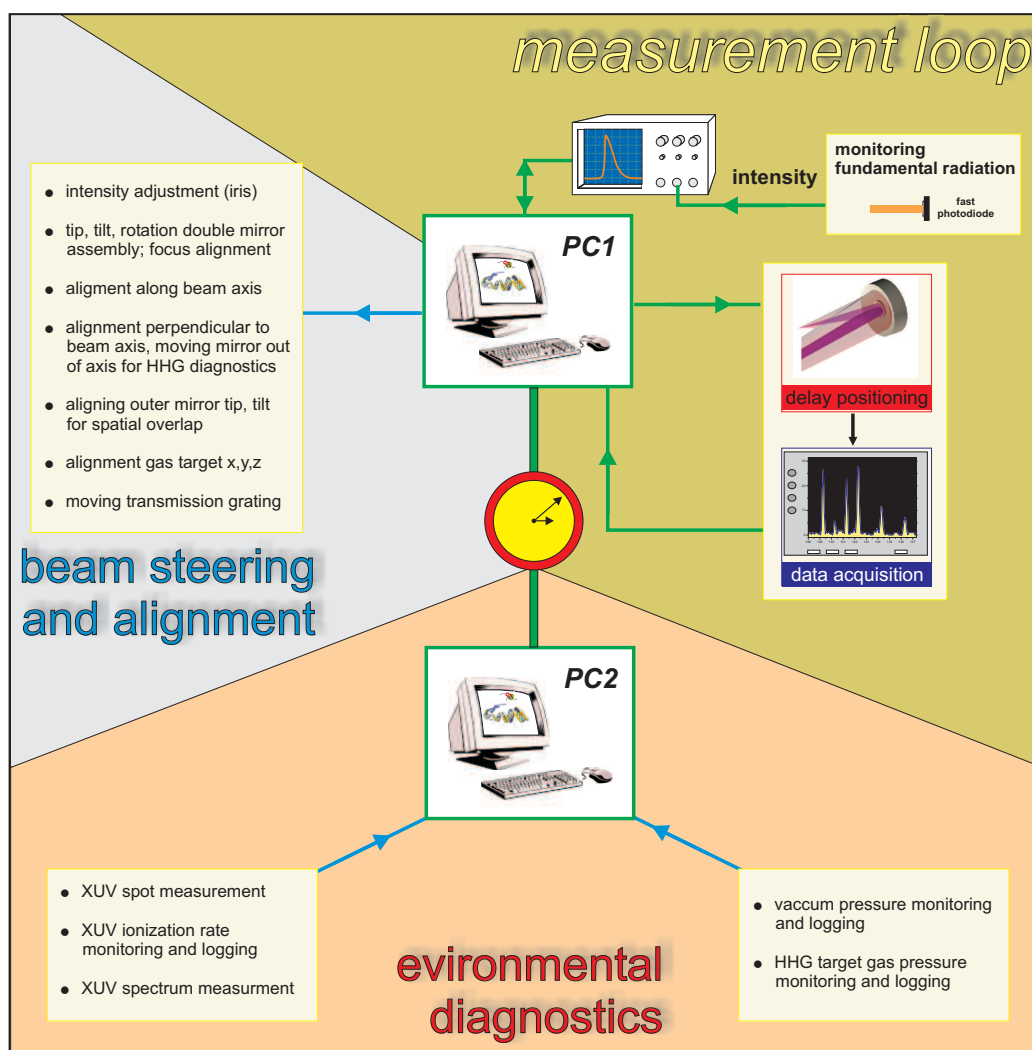


Figure 3.8: flowchart of the computational network steering and observing the experimental environment. The computers are synchronized in time using atomic clock client software

Figure 3.8 shows the main layout of the computer control circuits for the beam-line. The arrows indicate the flow of information.

### 3.4.1 Data Acquisition

The computers used to control and monitor the experiments, are separated in an "active" interaction (PC1) and "passive" data collection (PC2). Both computers are synchronized by use of *Automachron* client software synchronizing

the actual computer time with the NTP<sup>2</sup> time server of the *PTB Berlin* every five seconds and updating for deviations larger than 1 second, which will usually not happen in a 5 second synchronization interval. Therefore collecting and logging data in relation to PC time is in first instance sufficient to have synchronized data acquisition for both computers.

PC1 serves mainly for automated delay dependent data collection. The measurement loop is a sequence of setting the delay of the *PI P-621.1CD* delay stage and then collecting the data. In the case of the experiments presented here the time-of-flight spectra are retrieved with a *FastComtec P7887* multiscaler with a burst count rate of  $4\text{ GHz}$  or  $250\text{ ps}$  resolution. Additionally, a photo diode signal is monitored by an oscilloscope which is a measure for the relative laser intensity used in chapter 5 to determine the intensity of the laser.

The parameters of the measurement are controlled with a *Labview* program written for this purpose. LabView controls the position of the delay stage and acquiring data from the P7887 and the photodiode. Separate files are written for the parameters, delays and acquired data.

PC2 monitors the pressure for the whole vacuum part reading out a *Pfeiffer Maxigauge TPG256A* and presenting the data and the time dependent behavior of the pressure in a *Labview* program. Furthermore, PC2 uses a *BMC-PCI Base 1000* digital interface board with the *MAD12* 12-bit analog to digital conversion interface module. Via this module the data from the ionization detector and the *Sunx* pressure gauge is monitored with *LabView* programs written for this purpose and can be saved with the PC time to assign the data to the corresponding measurement on PC1. The back-thinned CCD Camera (*Princeton Instruments LCX400*) is connected to this computer as well. The XUV beam can be monitored either in the direct beampath or as a XUV spectrum in the first order of the transmission grating.

### 3.4.2 Beamline Automation

PC1 drives all in vacuum motors and stages. The optical components are motorized with *UHV picomotors* from *Newfocus* connected to an *iPico Ethernet Controller Model 8752* and cascaded modules for more than three axis of the type 8753. The steering of the irises in the differential pumping stages are

---

<sup>2</sup>The Network Time Protocol (NTP) is a protocol for synchronizing the clocks of computer systems over packet-switched, variable-latency data networks and is one of the oldest protocols in use since 1985; for more information see <http://ntp.isc.org/>

---



motorized with *UHV picomotors* and controlled by PC1, as well.

The translation stage that moves the double mirror assembly and the transmission grating perpendicular to the axis of the beam entering the chamber, is driven with a UHV compatible stepper motor driven stage with a travel range of 50 mm (*Micos VT-80 50*).

For all these components *LabView* programs were written to steer the components from the PC.

### 3.4.3 Reflectron ion mass spectrometer

For the ionization chronoscopy experiments, the detector chosen for this purpose is a reflectron type mass ion spectrometer from Stefan Kaesdorf comparable to the RFT10 [i04].

For *Time-Of-Flight (TOF)* mass spectrometers the energy selection properties are characterized by the flight time dispersion curves concerning the initial energy of the charged particle accelerated in the static electric field between the repeller and extractor electrode.

For the detection of ions, compensating for the energy spread of the various ions is the major issue and must be carefully chosen to gain the highest possible resolution. A reflectron type mass spectrometer strives for this by retroreflection of the ions in an electrostatic mirror with a dispersion curve of highest possible flatness over a large kinetic energy interval [80].

Figure 3.9 shows the layout and principle of the reflectron type ion mass spectrometer. Ion trajectories resulting from different points in space and focused in time by retroreflection in the ion mirror are drawn. The lower part of the figure depicts the principle of the ion mirror that corrects for the flight time dispersion caused by the formation of a particular ion at different points in space.

Generally, focusing the ionic charge states by this technique results in the first instance in a loss of information on the location of ion formation. At the same time this is a benefit to compensate for space charge effects originating from coulomb interaction of the charged ions. Space charge virtually behaves like the formation of the ion at a different location in space. Therefore, focusing of the ionic charges compensates for space charge effects.

---



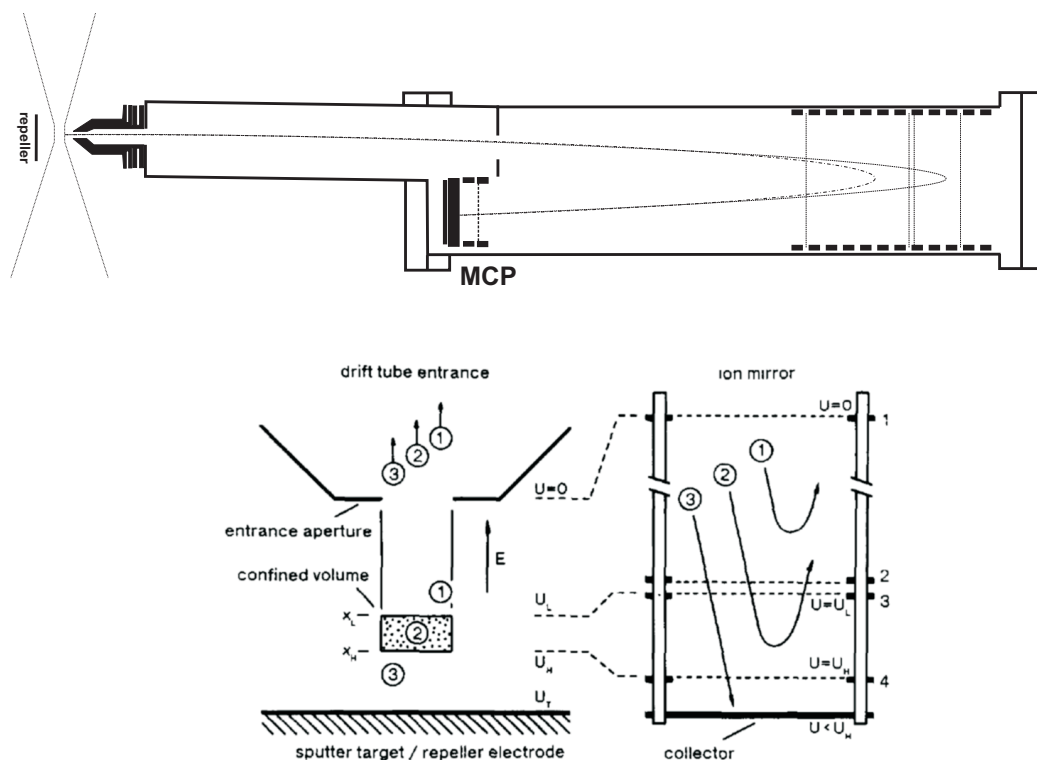


Figure 3.9: Layout and working principle of the reflectron ion mass spectrometer. The upper part shows a cross cut of the reflectron with two different ion trajectories shown inside and a sketch of the laser focus between repeller and entrance of the reflectron. The lower part denotes the benefit of this detector geometry, the areas 1, 2, 3 correspond to different ion trajectories with different accelerations due to the static electric field between repeller and the entrance aperture (extractor). On the right hand side the corresponding behavior of the ions in the ion mirror assembly resulting from the different volumes is shown. The special geometry and the ion mirror assembly allows to restrict the spacial volume of interest and correct for space charge effects.[79, 80]

Proper adjustment of the potentials in the ion mirror of this spectrometer allows confinement of a particular volume of interest, where the ions are formed with respect to the lower part of Fig. 3.9 [79].

The mass resolution of this ion spectrometer is specified to be on the order of  $\Delta m/m = 1000$ . The focused ions are detected with an *MCP* (*Multi Channel Plate*) detector. The signal is amplified and connected to the input of the *Fast ComTec P7887* multiscaler card.



## Chapter 4

# Characterization measurements

Before coming to the experiment itself measurements to characterize the experimental apparatus will be presented in the following sections.

### 4.1 CEP few-cycle Laser System

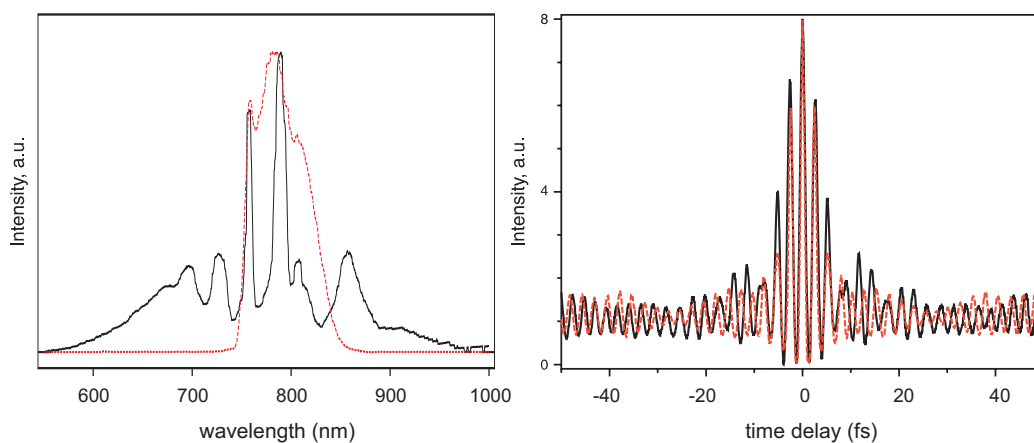


Figure 4.1: autocorrelation trace of the pulses after the hollow fiber - mirror compressor (right diagram). The dashed line shows the transform-limited autocorrelation as derived from the broadened spectrum (left diagram) assuming a flat phase. Full width at half maximum pulse width are 5.3 fs and 4.4 fs, respectively. The dashed spectrum (left) shows the spectrum in front of the hollow fiber.

Figure 4.1 shows the typical pulse characteristics of the laser system are characterized. Usually, the spectra retrieved in day-by-day operation are comparable to the spectra shown in the left diagram of Fig. 4.1, where the red dashed line represents the spectrum in front and the solid line the broadened spectrum

behind the hollow fiber.

In the plot on the right the autocorrelation traces for this spectrum are shown, where the red dashed trace represents the Fourier transform of the spectrum assuming a flat phase while the black solid line is the measured pulse duration. The full width at half maximum of the traces is given to be 5.3 fs for the measured trace and 4.4 fs for the fourier transform of the spectrum, respectively.

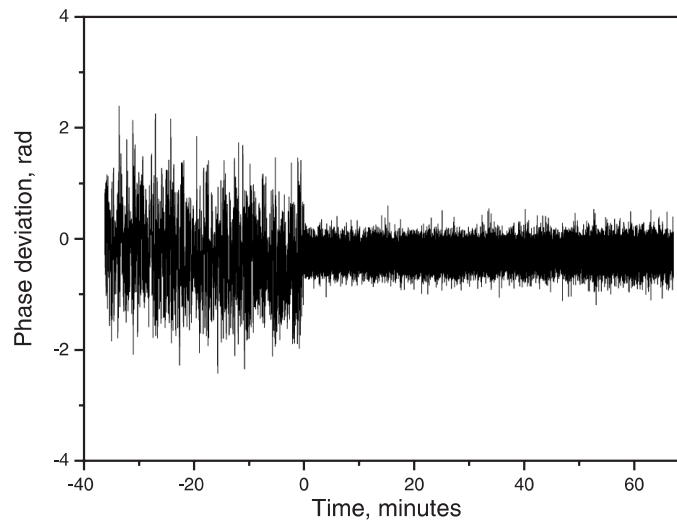


Figure 4.2: Phase deviations derived from the  $f$ -to- $2f$  interference pattern by the Fourier transform algorithm. The feedback loop was put into operation at  $t = 0$  [65]

The stability of the complete *CEP* stabilized laser system is represented in Fig. 4.2. It shows a plot of the phase deviations without stabilization, and with both feedback loops in operation exemplarily. The resultant rms jitter is 149 mrad equivalent to 60 as in a bandwidth between 0.13 mHz - 15 Hz when both loops are active. For the unlocked laser system, the rms phase deviation is in the order of 678 mrad. Generally, this does not represent the fluctuations outside the locking loops but is in the same order of magnitude as shown in [81].

Inside the hollow core fiber, any additional phase jitter is most likely due to pulse-to-pulse fluctuations of the amplified pulses and can be estimated to be in the order of 50 mrad corresponding to 20 as in [82, p. 37]. Reverting to 2.4.4 a jitter on this order only affects the *HHG* a small amount and regarding 2.5 the ejection and recombination points will "jitter" at the same time. Therefore,

the possibility of pump-probe experiments and the generation of isolated pulses is nearly unaffected by time jitter in this laser system.

## 4.2 High Harmonic Beam characterization

For the generation of the High Harmonic beam the direct spot size at a distance of 2175 mm from the source is recorded by the cooled back-thinned CCD camera shown in Fig. 3.1. Taking into account that a 400 nm Zr filter is introduced for observation of the direct XUV beam to suppress the fundamental laser radiation and reduce the transmitted Harmonic radiation so much that the camera chip is not saturated, the spot and the corresponding cross cuts at this distance are shown in Fig. 4.3. The diagrams show the real spot recorded in the small insets in a bandwidth from 70 ~ 100 eV. From this the indicated cross cuts were extracted and fitted with a Gaussian function<sup>1</sup>. In the x-direction the  $2\omega_0$  width covering 95% of the full energy is 3.95 mm and in y-direction the  $2\omega_0$  width is 1.89 mm.

With respect to the spot shown in the inset the situation observed here is with a new hole burned into the target. After some time when the hole is larger the spot becomes symmetric and round and a little bit bigger. From these measurements the divergence and source size for the XUV beam can be calculated. The divergence  $\theta_0$  of the XUV beam is determined by the beam radius and the distance corresponding to half of the opening angle, which leads to

$$\tan \theta_x = \frac{1}{2} \cdot \frac{3.95}{2175} = 9.08 \times 10^{-4} \quad (4.1)$$

$$\tan \theta_y = \frac{1}{2} \cdot \frac{1.89}{2175} = 4.34 \times 10^{-4} \quad (4.2)$$

---

<sup>1</sup>the fitting procedures were performed using Origin; by definition of the Gaussian function  $\omega_0$  is the full width at  $1/e$  of the Gaussian distribution; to match the standard definitions  $w_0$  is the half width at  $1/e^2$  of the Gaussian distribution

---

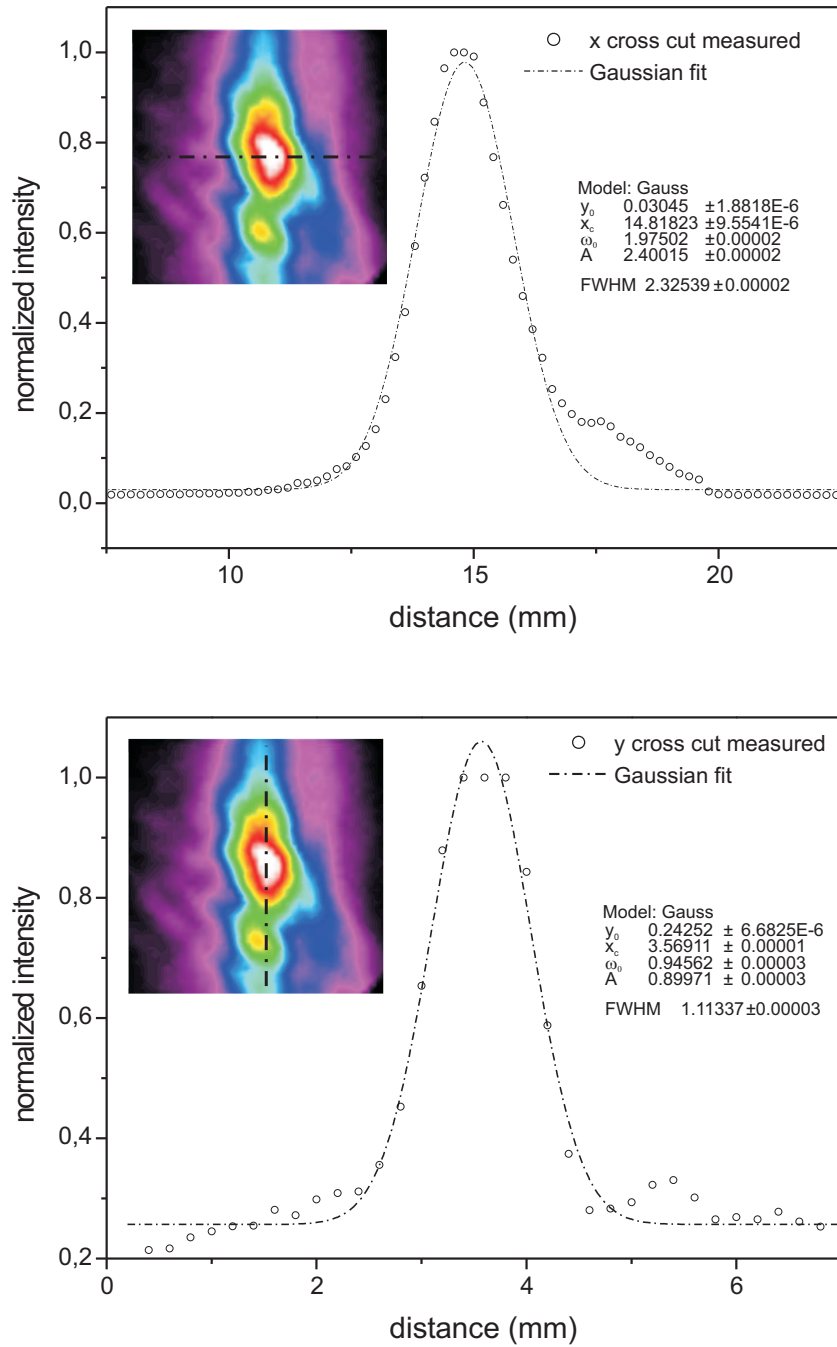


Figure 4.3: X and Y cross cut of the HH beam measured 2175 mm behind the source where X is the horizontal and Y the vertical direction. The inset shows the original retrieved spot where the dash dotted lines show the cuts.

The source size for the central wavelength of 13 nm is given by

$$\tan \theta_0 = \frac{\lambda}{\pi w_0} \quad (4.3)$$

$$\leftrightarrow w_0 = \frac{\lambda}{\pi \tan \theta_0} \quad (4.4)$$

$$\rightarrow 2w_x = 9.114 \mu m \quad (4.5)$$

$$\rightarrow 2w_y = 19.028 \mu m \quad (4.6)$$

For the spotsize shown the cross cut in x-direction is more realistic. Thus a source size in the range of 9 - 18  $\mu m$  seems to be reasonable in this energy range and is just a lower limit, since the used equations assume a perfect Gaussian beam with a *quality factor*  $M^2 = 1$ . For the laser system used  $M^2 < 2$  is specified [i02]. Thus the determined focus size can differ by a factor of 2.

The size of the driving laser focus assuming  $M^2 = 1$  again for  $\lambda = 740 \text{ nm}$ , a focal length of  $f = 50 \text{ cm}$  and a beam radius of  $w_0 = 4 \text{ mm}$  is given by

$$w_f = \frac{f \lambda}{\pi w_0} \quad (4.7)$$

$$\Rightarrow w_f = 29,44 \mu m \quad (4.8)$$

Hence the spot diameter at  $1/e^2$  is  $2w_f = 58,88 \mu m$  in the Gaussian limit. Comparing with the XUV diameter specified above it is in a quite good agreement with the expectation for the XUV source size to be approximately 50% of the laser focus in this energy range.

Regarding the spot diameters at the position of the XUV mirror the position from the source is 1602.5 mm. This gives beam diameters of

$$w_x^{mirror} = 1.455 \text{ mm} \quad (4.9)$$

$$w_y^{mirror} = 0.6970 \text{ mm} \quad (4.10)$$

For the full width at 95% intensity of the XUV we receive 2.910 mm and 1.394 mm. Generally, the beam diameter is expected to become larger, if the source is sufficiently drilled. Using the "*Knife Edge*" Method would give more detailed information on the effective spot size assuming a nearly Gaussian intensity distribution but the asymmetries of the spot would be blurred. For this

---

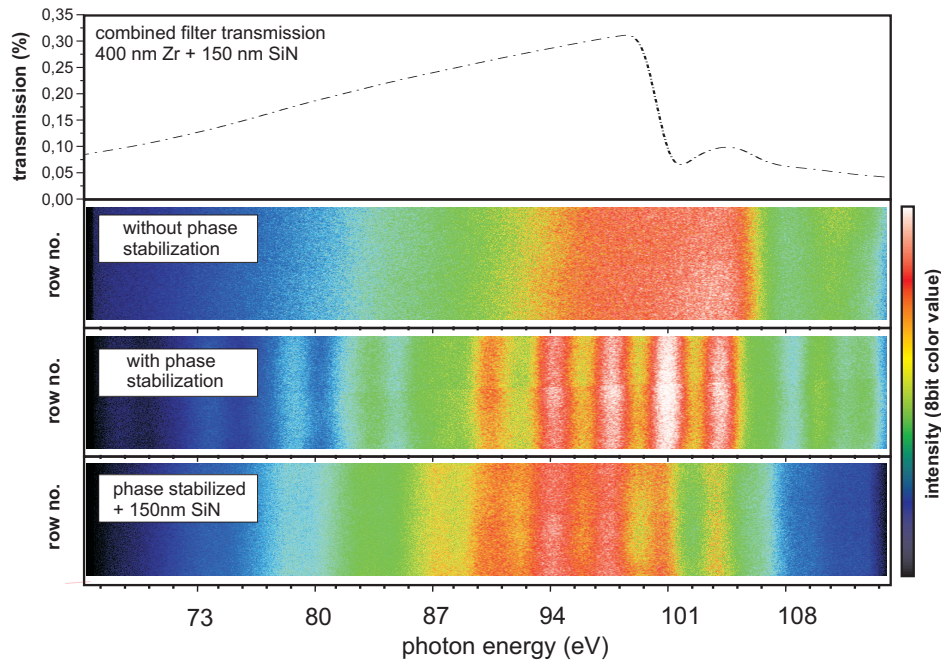


Figure 4.4: typical XUV spectra resolved with this setup; in the upper panel the complete transmission curve for the lowest spectrum shown is plotted (data from [i03]). The calibration is done by use of the silicon  $L$ -edge and the 3.2 eV separation between the observed plateau harmonics.

reason the cross cuts are shown.

When observing the direct XUV beam on the back-thinned CCD camera, it is possible to move a 10000 lines/mm  $\text{Si}_2\text{N}_3$  transmission grating into the beam path and moving the camera into the first order of diffraction (see Fig. 3.1). Typical spectra are shown in Fig. 4.4. In the upper diagram the transmission curve of 400 nm Zr + 150nm  $\text{Si}_2\text{N}_3$  is used to calibrate the spectrum utilizing the Si  $L$ -edge at  $\sim 100$  eV.

The upper XUV spectrum was taken without  $CEP$  stabilization, whereas the lower ones are taken with  $CEP$  stabilization of a *cosine*-like pulse. The feature of the plateau harmonics is clearly resolved and used to determine the energy range calibration. A  $\text{Si}_2\text{N}_3$  membrane is introduced in the lower spectrum to specify the 100 eV energy. Furthermore, the reflectivity curve of the used XUV mirror is centered at about  $\sim 90$  eV slightly below the absorption edge of the  $\text{Si}_2\text{N}_3$  membrane. Placing the membrane in the beam path gives a possibility to adjust the *cutoff* matching the mirror reflectivity curve.



The resolution of the XUV spectrometer is sufficiently high to distinguish a sine and a cosine pulse by eye. Due to this it is an obvious tool for adjusting the drive laser phase and energy.

### 4.2.1 Measurement of the focus size

To estimate the focus size, geometrical ray tracing simulations were done with ZEMAX using the following parameters: Source diameter  $10 \mu\text{m}$  at  $\omega_0$ , wavelength  $\lambda = 13\text{nm}$ , divergence as given above, but with the same value for the divergence in both directions. Following the real experimental conditions, a  $5^\circ$  tilt with respect to the surface normal for one axis of the focussing mirror and a distance between source and mirror of  $1602.5 \text{ mm}$  were used.

The intensity distribution of the beam is assumed to be Gaussian. Furthermore, the simulations and measurements are restricted to the inner mirror supposing that the focus of the outer "donut" is at least larger than the focus of the inner mirror.

Figure 4.5 displays the measured and simulated focus sizes determined by the "Knife Edge" Method described in Appendix B for the measured and simulated data.

The x cross cut (left) gives a Gaussian beam diameter at the focus of  $22.58 \mu\text{m}$  from the experimental data and  $13.82 \mu\text{m}$  for the simulation which equals the beam radius  $w_0$ . There are several factors that were not taken into account that explain this discrepancy. The experimental focus is astigmatic as a result of the  $5^\circ$  tilt angle. Thus what is called a focus is the most round focus that can be observed, but possibly not the smallest and most intense one. Moreover, as the inset in Fig. 4.3 depicts, the XUV beam is strongly distorted and definitely not symmetric. Even if the "Knife Edge" Method integrates over the intensity and flattens these distortions, the divergence is different from that in the simulations. The main deviation is based on the determination of the path length between focus and imaging optics and imaging optics to the camera chip to calculate the magnification for a given focal length which has been determined to be a factor of 5. Even if the imaging mirror shown in Fig. 3.1 is replaced by a lens and a wedge to avoid further astigmatism introduced by this mirror, the determination of the magnification denote the largest error source. The error is estimated to be on the order of 20% and within this estimation the simulation matches the experimental data. For the y direction the deviation turns out to be much smaller with  $13.68 \mu\text{m}$  for the simulation and  $17.94 \mu\text{m}$  for the measured focus diameter.

---

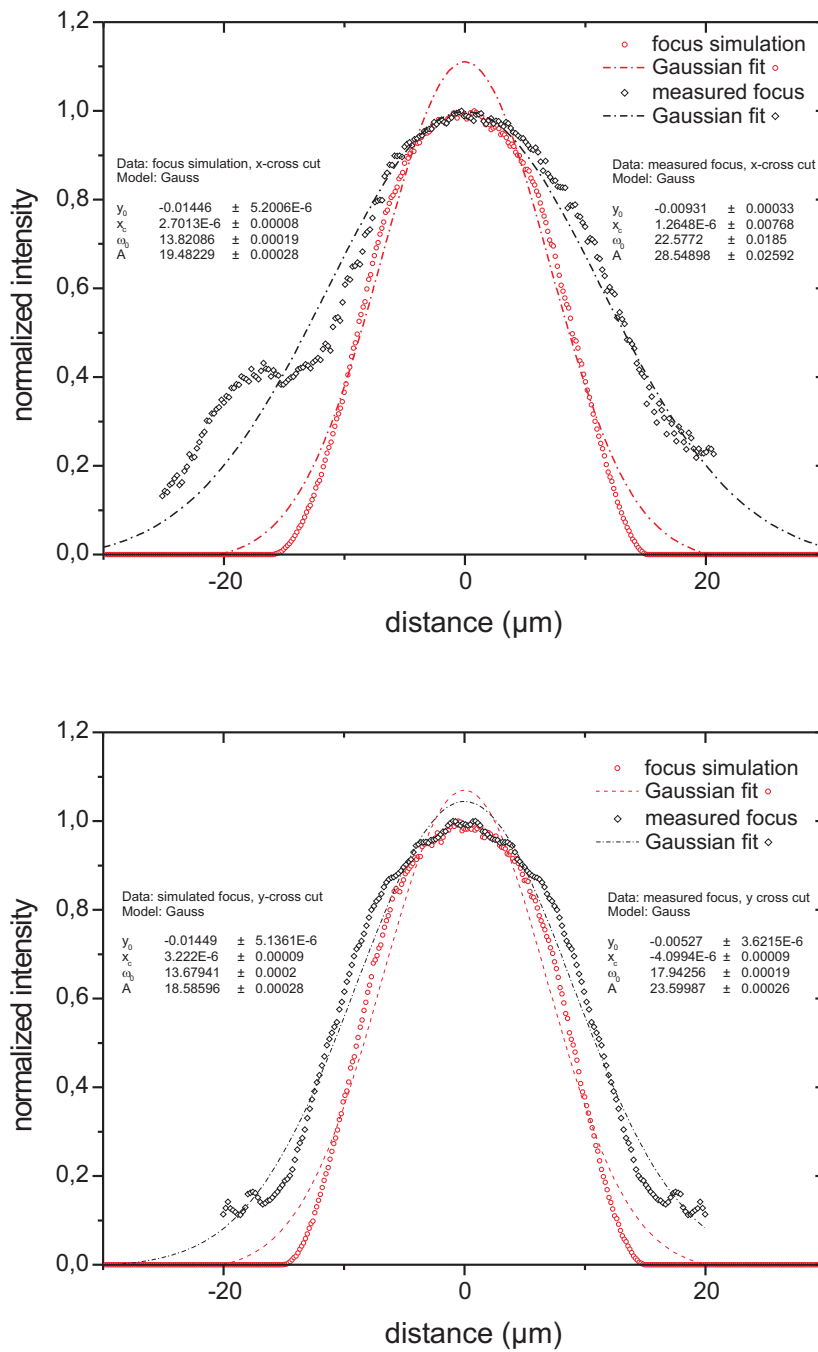


Figure 4.5: simulated and measured focus size for the inner mirror. The profiles have been retrieved using the "Knife Edge" method applied to the image retrieved from a CMOS camera monitoring the focus shown in Fig. 3.6 and using the software described in Appendix B.

## 4.2.2 Calculation of the effective partial XUV cross-sections

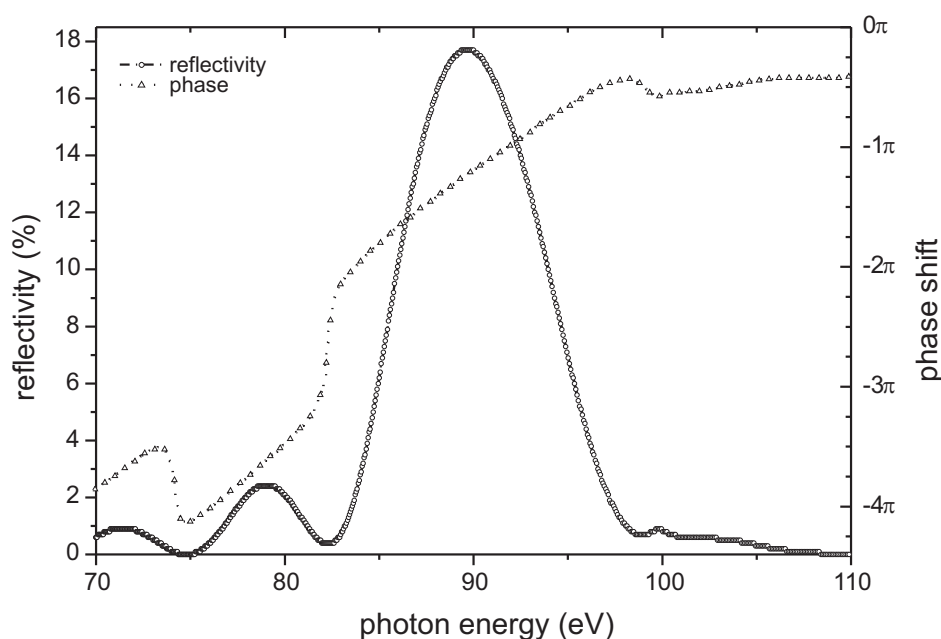


Figure 4.6: computation of the reflectivity and phase behavior of the XUV mirror used in the experiment. The reflectivity curve is already the multiplication with the transmission curve of a 150 nm Zr foil, added in the experiment to suppress the fundamental laser radiation. Measurements at the PTB at BESSYII in Berlin have shown that the type of manufacturing process for this mirror leads to a shift in the reflectivity towards higher energy in the order of 4% thus the peak reflectivity is supposed to be  $\sim 91$  eV

Figure 4.6 depicts computations of a recursive fresnel code of the reflectivity and phase of the XUV mirror that is used in the experiment. The reflectivity curve is already multiplied with the transmission of a 150 nm zirconium foil which is used to suppress the fundamental radiation. The data for the transmission of the zirconium foil is obtained from [i03].

Calculating the effective partial cross-sections, the mirror reflectivity was fitted with a Gaussian. The partial cross-section data given in [83] were taken for the ions of neon, krypton and xenon in the energy bandwidth corresponding to the reflectivity bandwidth of the XUV mirror and fitted with a Gaussian, as well.

Integration of the Gaussian fits and dividing the area of the partial cross-section by the mirror reflectivity leads to a mean partial cross-section within the mirror bandwidth shown in Tab. 4.1.

Gas	charge		
	$A^+$	$A^{2+}$	$A^{3+}$
Neon	4.01	0.14	
Krypton	0.17	0.37	0.07
Xenon	1.53	14.99	5.00

effective partial ionization cross sections (Mb)

Table 4.1: effective ionization cross-section taking the reflectivity bandwidth of the mirror and 150 nm Zr into account, based on the data of [83]

The data in [83] is not covering the energy bandwidth of the mirror very well because of the large energy steps between the data points. Furthermore, fitting the few data points with a Gaussian distribution may overestimate the mean partial cross-section. Especially in the case of krypton the mirror covers the  $3d \rightarrow 5p$  resonances where the partial cross-sections are greatly enhanced.

The effective partial cross-sections calculated in this way are in good agreement with the experimental data. As an example, referring to the xenon data in Fig. 4.7 and integrating the count rates of the isotopes to get the total number of counts for a particular ion, the total count rates for each ion are compared to the effective cross-section in the following table.

	charge		
	$Xe^+$	$Xe^{2+}$	$Xe^{3+}$
ion count rate	307	2513	914
effective cross-section	1.534	14.988	5.001
ratio	200.31	167.66	182.76

Table 4.2: comparison of the total ion count rates with the calculated effective cross-sections

Deviation from the reflectivity profile of the mirror will result in a difference for the effective cross-section. In connection to Fig. 2.7 the real shape of the incident harmonic cutoff spectrum reflected by the XUV mirror was not taken into account and assumed to be constant over the given spectral range.

### 4.2.3 Resolution of the Reflectron ion mass spectrometer

All measurements presented in chapter 5 were obtained with the *reflectron ion mass spectrometer*. Figure 4.7 shows the resolution of the spectrometer. An XUV ion spectrum of xenon is shown for example.

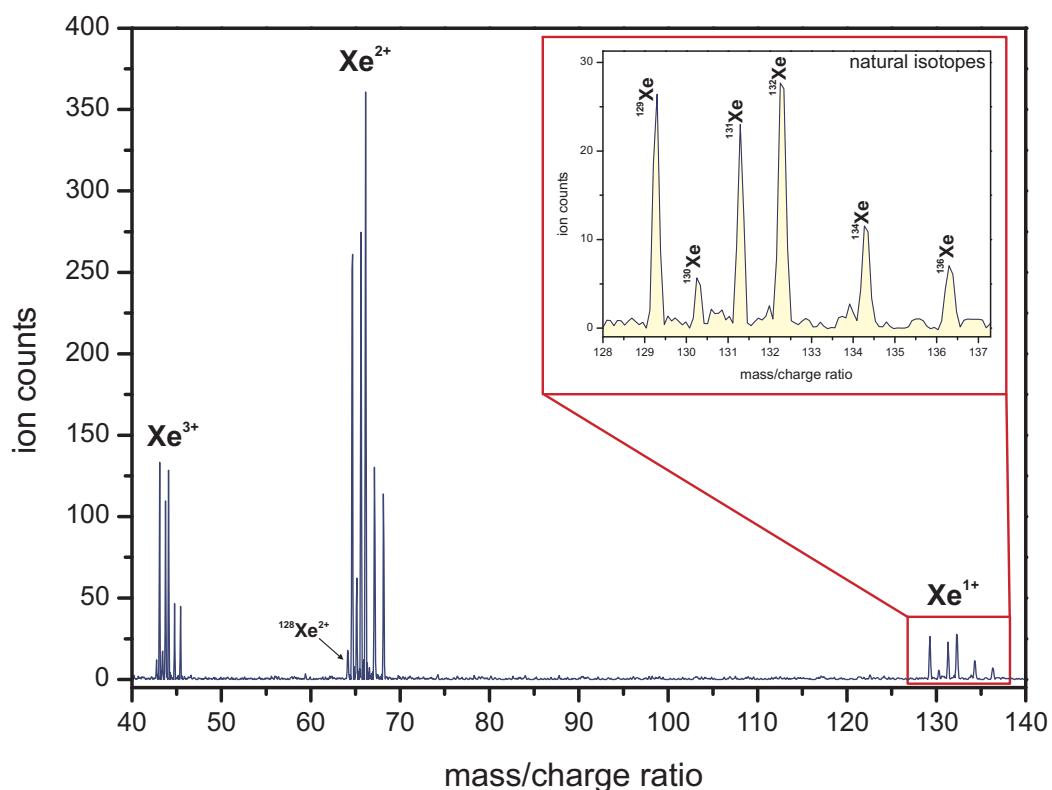


Figure 4.7: Typical XUV ion spectrum of xenon resolved with the TOF reflectron ion mass spectrometer described in 3.4.3. Even for low count rates the resolution is high enough to measure with isotopic resolution in all the ionic states. The inset shows a zoom of the  $\text{Xe}^{1+}$  ionic states split in the natural isotopes of xenon. The missing  $^{128}\text{Xe}$  ion is hidden in the background, but due to better statistics well resolved on the left side of the  $\text{Xe}^{2+}$  and  $\text{Xe}^{3+}$  isotope groups.

The plot shows the ion spectrum of xenon measured with XUV excitation centered at  $\sim 90\text{eV}$  following the XUV ionization cross-sections reported in [83]. As one can see, the natural isotopes of xenon are well resolved up to the third ionic state of Xenon. The inset zooms in on the  $\text{Xe}^+$  isotope group, which has the smallest cross-section. Because of the short time for data collection the  $^{128}\text{Xe}^+$  is missing, but clearly resolved in the higher ionic

charges. Effects like space charge are practically negligible since the compensation of the flight time dispersion in reflectron geometry is not sensitive to this within certain limits. Furthermore, in every ionic group the isotopes are resolved with the ratio of their natural existence with reference to the data in [84].

## Chapter 5

# Attosecond real time observation of electron tunnelling and multi-electron dynamics in rare gases

In this chapter the experimental results will be discussed in studies of three noble gases using this newly developed technique of *attosecond-time-resolved ionization chronoscopy*.

The experiment was initially based on calculations of *CEP* phase dependencies in the ionization yield of Helium [64] and Xenon [85]. Similar to electron streaking measurements [12, 10] the measurement of the ion yield should be sensitive to the *CEP* phase of the few-cycle laser pulse. This behavior is also strongly dependent on the intensity of the IR-laser field. The calculations did not include the effects of the probing XUV pulse acting on the atomic gas target. In this case the processes taking place become different and the detection of the ionization yield with respect to the different ionic states opens up a new way to resolve inner-shell dynamics which are not directly accessible in the energy domain. Figure 5.1 shows these main concept of the experiments that are presented in the following sections.

Let us assume a laser pulse with an intensity sufficiently low that the laser cannot ionize the bound electron with potential  $W_2$  for  $\tau_D < 0$ . Thus the atom remains neutral. For  $\tau_D = 0$  the XUV pulse meets the neutral atom at the peak intensity of the laser pulse. As in the first case the laser pulse can be neglected, because the intensity is sufficiently low, but the XUV pulse can act on the atom in two different ways:

---

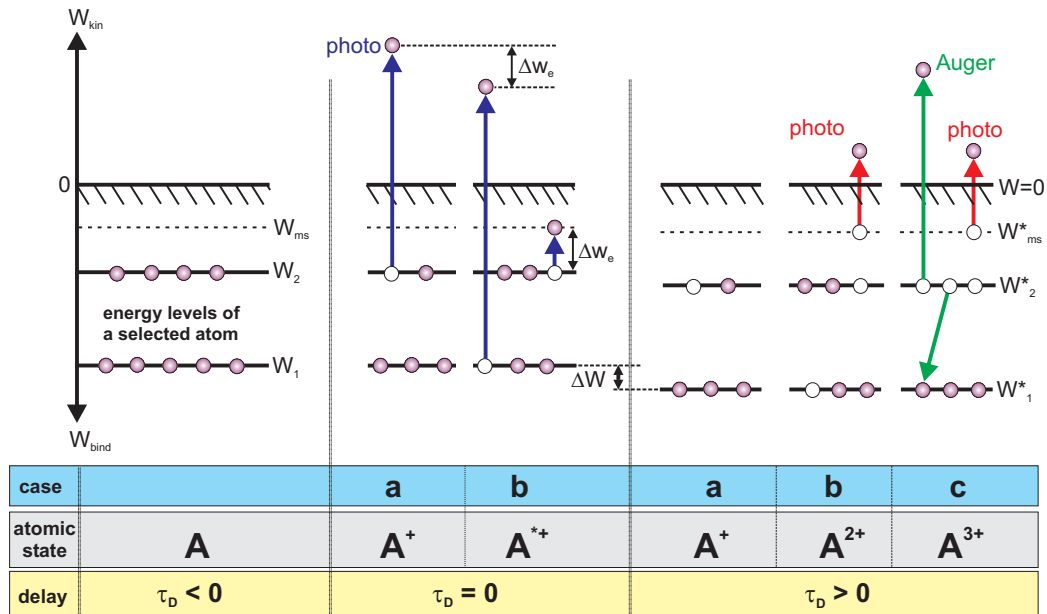


Figure 5.1: Illustration of the ionization sequence related to attosecond excitation and IR probing. In this picture the intensity of the IR laser pulse is assumed to have an intensity that is too low to act on the bound electron at  $W_2$ . The ionization and excitation of the former neutral atom by the attosecond XUV pulse enables the IR laser pulse to ionize the excited electron  $W_{ms}$ . Furthermore, inner-shell processes may be induced, as shown in case *c* for  $\tau_D > 0$ . For a detailed description see text.

- a a valence electron is photoionized and appears in the continuum with a kinetic energy  $W_{kin} = \hbar\omega - W_{bind}$ . This leads to a singly ionized atom.
- b an inner-shell electron or deeply bound valence electron is ionized and the photoelectron appears in the continuum with a slightly lower kinetic energy because the atom gets excited due to shake-up processes  $W_{kin} = \hbar\omega - W_{bind} - \Delta W_e$ . Additionally a core-level shift  $\Delta W$  will occur. The atom is singly ionized and excited.

For  $\tau_D > 0$  the laser pulse meets atoms in an excited ionic state that the XUV pulse created at  $\tau_D = 0$

- a because the laser intensity is sufficiently low that the bound electron  $W_2$  cannot be ionized by the laser field, nothing further happens to the singly ionized atom.



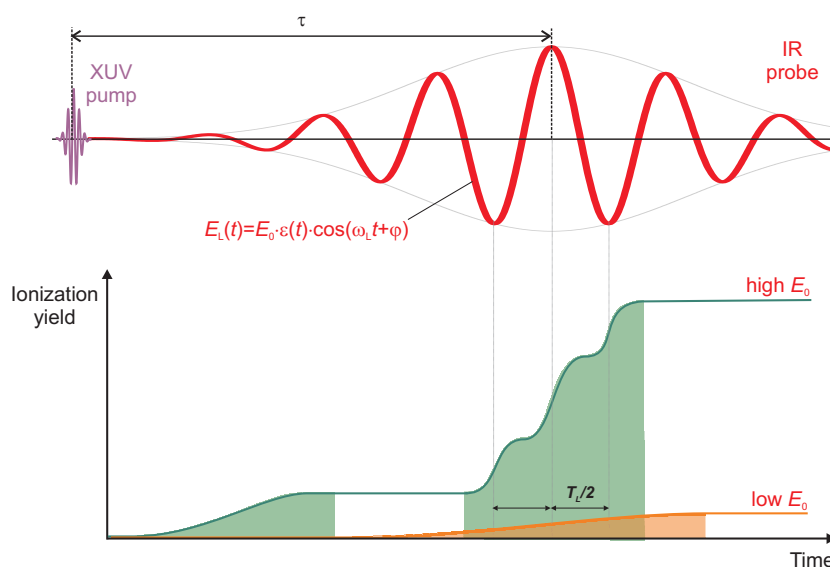


Figure 5.2: The ionization yield of the a single excited state is shown in dependence of the relative delay  $\tau$  between the XUV excitation (pump) and IR laser pulse (probe) as well as the field strength of the IR laser field. The red curve shows the delay dependent increase of the population in the atomic ion in the case of a low intensity IR laser pulse, where *multiphoton ionization* dominates. The green curve shows the ionization yield dependence in the case of a strong IR laser field well in the *tunnel- or above the barrier ionization regime*

- b once there is an excited electron existing the laser intensity is suitable to ionize the excited electron at  $W_{m.s.}$ . In this case the ionic charge state is increased by one and finally the atom is doubly ionized. Taking into account the excitation with an attosecond XUV pulse, the ionization rate follows strongly the field strength or intensity of the laser pulse (compare Fig. 2.9).
- c if the ionization of a core level is involved, inner-shell processes like Auger decay could be induced depending on the excitation energy of the XUV photon and the atomic target. In the case shown an Auger decay takes place, while the excited electron is ionized due to the laser pulse. A triply charged ion is created.

In particular, in case *c* there are two competing time constants for the process. The ionization of the excited electron due to the laser pulse results in an increase in the population of the doubly charged ion. In a competing effect, the Auger decay decreases the population of the doubly charged ions and gives a rise to the population of the triply charged ion. The competition of these two processes depends not only on the laser pulse duration and intensity, but also on the time

constants for the observed Auger decay.

In this illustrative description of the experiment we neglected two aspects of the real experiment which are of major importance:

In Fig. 5.1 the excited electron is bound to a discrete state with binding energy  $W_{ms}$ . Generally this is not the case. As will be shown in the following sections, several excited states are populated by the XUV pulse. Some of them with comparable probability. This defines a certain bandwidth of excited states that become accessible by the laser pulse. Thus it is possible to obtain information about the levels involved in the measured ionization yield. Furthermore, an intense laser pulse was assumed, but it remains to be determined if the nature of the observed ionization process is correlated with the multiphoton regime, or if we assume the field strength of the laser to tunnel ionize the corresponding excited states.

Figure 5.2 shows the difference between these two cases, assuming again a discrete excited state that is ionized by the laser pulse. With increasing delay  $\tau$  the total ion yield measured is given by integration over all laser generated ions after XUV excitation. For low laser field intensities the multiphoton ionization dominates the process and the resulting curve will predominantly follow the integration of the ionization yield over the remaining laser pulse and related to the typical behavior of *MPI* following Eq. (2.16), which is depicted with the red curve. For high laser intensities in the tunnel regime or over the barrier ionization regime, the ionization yield depends on the actual strength of the laser field. The left part of the green curve depicts the multiphoton nature of the ionization in these regions of the laser pulse. In the central part of the laser the steep steps shows the field dependent ionization of the excited electron in the tunneling regime.

It is expectable that if the number of excited states becomes too large, the substructure of the time dependent ionization yield as shown in Fig. 5.2 will be washed out by integration over contributions from all levels to the final ionization yield. This is especially the case if we consider highly excited states with a substantial occupation probability equally distributed over a specified energy bandwidth.

With this description the complexity of the processes and the difficulties for measurement and interpretation regarding this new technique should have been demonstrated.

---

For the experiment presented in the following sections the experimental apparatus described and characterized in chapter 3 and 4 was used to measure time-dependencies in the ionization processes of noble gas atoms excited by an XUV attosecond pulse with a bandwidth and spectral shape as shown in Fig. 4.6.

Data analysis and computations described in *Appendix C* and *D* are mainly based on the work of V. Yakovlev and M. Kling and are part of the supplementary online information of [86].

## 5.1 Tunneling ionization dynamics in Neon

This experiment focusses on light induced tunneling of shake-up electrons. For this purpose we ionize neon atoms shaken-up by a  $\sim 250$  as XUV pulse. Figure 5.3 shows the level structure of XUV excited neon atoms and the relevant transitions for the ionic states. According to Tab. 4.1 the absorption of photons within the mirror bandwidth will produce singly and doubly charged neon atoms with a probability of 3.17% and 96.65% respectively neglecting the shape of the high harmonic spectrum. This is in reasonably good agreement with the experimentally determined probabilities of 4.8% for  $\text{Ne}^{2+}$  and 95.2% for  $\text{Ne}^{1+}$ .

Due to shake-up processes a small fraction of the singly-charged neon atoms is excited to  $2p^{-2}nl$  configurations each of which consist of  $2p^{-2}(^3P)nl$ ,  $2p^{-2}(^1D)nl$  and  $2p^{-2}(^1S)nl$  states with the probabilities of the different channels well known from electron spectroscopy [41]. Since these satellite states can only decay radiatively and on a picosecond time scale [87] and Auger decay is absent for these excitation energies [88] the few-cycle laser field can remove electrons from these shake-up states once the excited states are populated by the attosecond XUV pulse. Therefore, the probability of double ionization increases to 6.7% due to population transfer from the  $2p^{-2}nl$  states by depletion from the IR laser field. The population distribution is shown in Fig. 5.3. The most probable shake-up satellites are the  $2p^{-2}3p$  and  $2p^{-2}3s$  with 50% and 25% occupation probability. Their binding energies are accessible for the laser electric field.

The laser pulse intensity is chosen to produce only singly-charged ions (in configuration  $2p^{-1}$ ) corresponding to an ionization energy above 21.56 eV but below the double ionization threshold of 48.47 eV depicted by the red shaded area in Fig. 5.3 with a measured laser intensity of  $(7 \pm 1) \times 10^{13} \text{ W/cm}^2$ . This

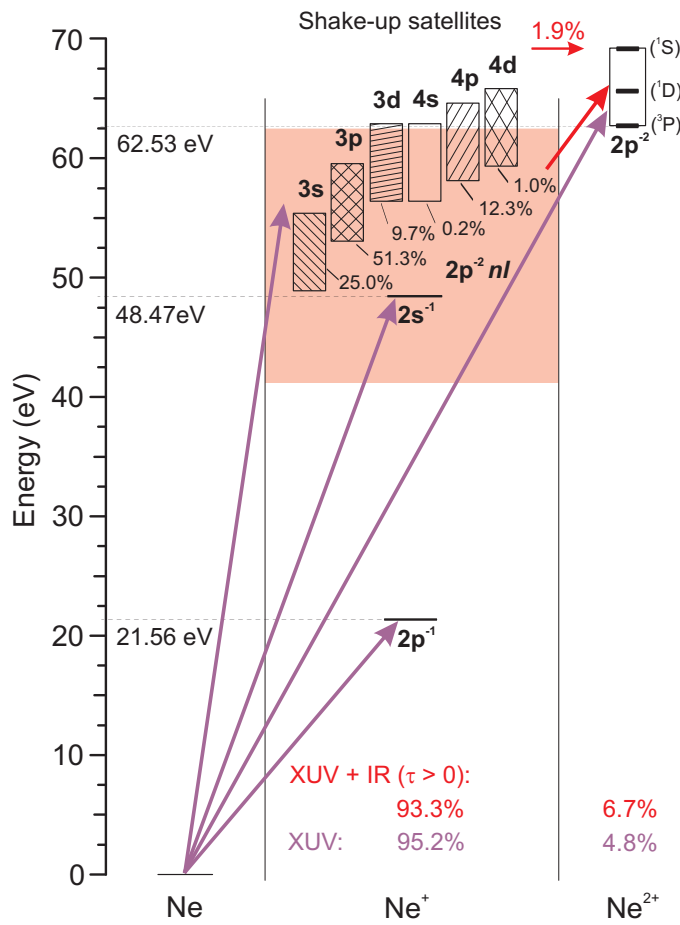


Figure 5.3: Energy levels and transitions relevant for the study of light induced tunneling of excited states in neon; purple arrows show XUV induced transitions; red arrows show laser induced transitions; the red shaded area indicates the energy levels accessible for the laser pulse.

means that the XUV generated Ne<sup>2+</sup> ionization rate is not affected by the laser for negative delays  $\tau_D < \tau_L$ , when the laser pulse reaches the target before the XUV pulse.

The Keldysh parameter  $\gamma$  for the satellite states in the observed effects indicates that tunnel ionization dominates (see Appendix C). Therefore, once the XUV populates the states, the laser pulse can efficiently deplete them depending on the local field strength.

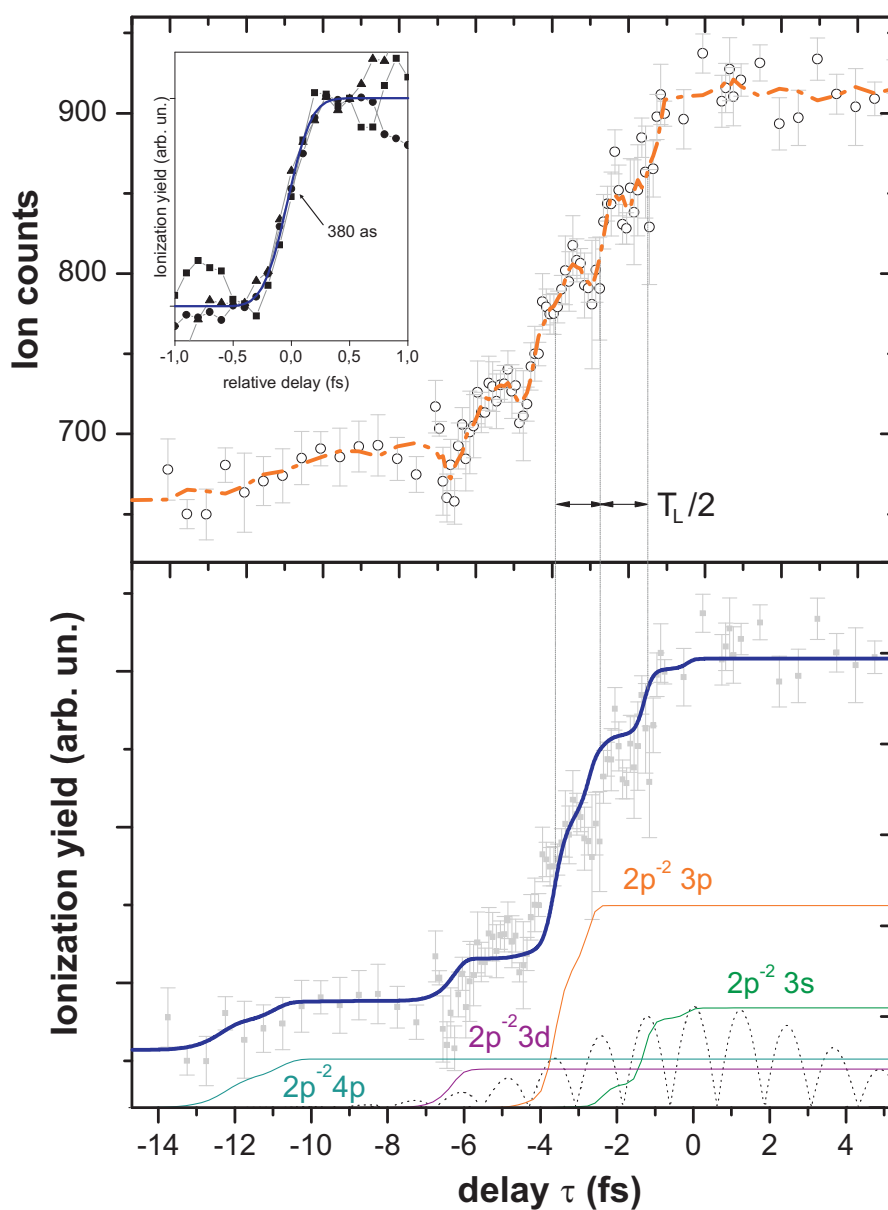


Figure 5.4:  $\text{Ne}^{2+}$  ion yield versus delay, between attosecond XUV excitation pulse and femtosecond probing laser pulse. The upper panel shows the measured data; the lower panel shows the computation of the process using generalized ADK theory with the levels used for the computations; the inset in the upper panel depicts a zoom in a step resulting from 3 measurements normalized to have the same ionization yield enhancement. The blue solid line is an error function fit. [89]

The upper graph of Fig. 5.4 shows the measured pump-probe trace as the number of  $\text{Ne}^{2+}$  ions versus delay  $\tau$  between the exciting attosecond XUV pulse and the CEP stabilized probing laser pulse. The data was acquired through six delay scans repeated under the identical experimental conditions. The signal was integrated for three seconds at each delay setting. The circles and the error bars show the average and the standard deviation of the results of the six measurements analyzed by the procedure described in Appendix D.

Negative delay times indicate that the probing laser pulse is early and acts on the target atom before the exciting XUV pulse. Positive delays mean that the XUV excitation is early and the probing laser pulse acts on the excited neon atom with the levels of Fig. 5.3.

It should be mentioned that the definition of zero delay may imply the perfect temporal overlap of the maximum field strength of the probing laser pulse and the exciting XUV pulse. Unlike photoelectron based streaking measurements [12] this is not the case for *ionization chronoscopy* since the depletion of all excited states involved can occur much before the maximum field strength of the probing laser pulse thus there is no further enhancement of the ionization yield, even if this is not the perfect temporal overlap of both pulses. As a consequence, there is an optimal intensity by observation of the measured dynamics shown in Fig. 5.5. It is common for all experiments described in the following that there is an optimal intensity where the observed effect is best resolved.

In Fig. 5.4 for large negative delays there is no enhancement of the ionization yield. This means that there is no contribution to ionization of the doubly charged neon resulting from the laser pulse. Furthermore, this is an indication that no ionization enhancement occurs resulting from XUV ionization of singly charged neon atoms generated by the laser pulse. As a consequence, the laser pulse does not saturate the neon target with respect to the single ionization of neon and the enhancement of the ionization yield is based on the depopulation of XUV excited states in singly ionized neon.

The primary enhancement starts at a delay of -7 fs clearly following a stepwise increase with a periodicity reproducing half the laser oscillation period indicated by  $T_L/2$  in the graph.

The inset in Fig. 5.4 depicts an ionization step extracted from three different measurements normalized to have the same change in the ionization yield. Fitting with an error function determines a total rise time of 380as FWHM, which is a measure related to the time of tunneling. The complete width of the

---

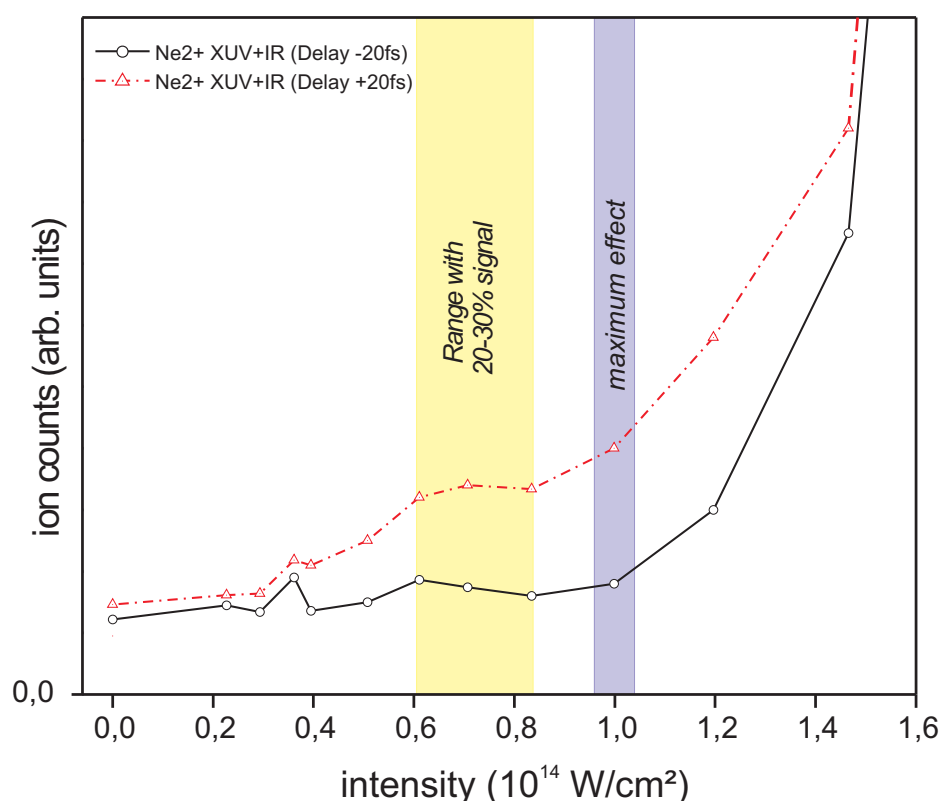


Figure 5.5: intensity dependent measurement of the ionization yield for delay -20 fs and +20 fs; for the low energy part the contrast decreases, because the laser intensity is not sufficient to reach the excited levels of the neon atom; for the high energy region the effect is basically limited by the fact that the production of doubly ionized neon from the laser pulse increases. Shown by the symmetric increase for both delay positions. The optimum intensity is in the range  $6 - 9 \times 10^{13} \text{ W/cm}^2$

full enhancement is approximately the full width at half maximum (FWHM) of the laser pulse as indicated by the dotted line in the lower graph. This represents the  $|E(t)|^2$  of the laser electric field used in the modeling of this measurement shown in that graph.

The lower graph shows the simulation of the pump-probe experiment based on the nonadiabatic theory of tunnel ionization [89] performed by Yakovlev. The thin solid lines show the calculated fractional ionization rates contributed by electrons liberated from different shake-up states. The thick solid line depicts the overall ionization rate obtained by adding the fractional rates from the shake-up states. These simulations were carried out for a Gaussian 250 as XUV pulse and a Gaussian 5.5 fs laser pulse with a peak intensity of  $7 \times 10^{13} \text{ W/cm}^2$ .

The highly-excited  $2p^{-2}4p$  states are completely ionized even by the wing of the laser pulse, while significantly higher intensities are required to deplete  $2p^{-2}3s$  states. The agreement with the experimental data is quite good, but the sharp dips on the top of the step is not very well reproduced. Currently we attribute this to the influence of the probe laser field on the excitation process which is not included in the simulations. Recent work of *Smirnova et al.* [90] provides a first treatment in this direction.

These steps were reproduced in several experiments and with different *carrier envelope phases*. If the phase is not stabilized the stepwise structure disappears and only the main enhancement in the ionization yield persists which is exactly the behavior that is expected.

## 5.2 Multi-electron ionization dynamics in Krypton

In another experiment the atomic gas of interest was krypton. The main difference between these measurements is based on the fact that in the XUV energy range of the mirror, krypton provides the probability of Auger and resonant Auger decays following inner-shell ionization and excitation, respectively.

Figure 5.6 presents the levels and transitions relevant for the interpretation of the pump-probe measurement shown below. For excitation energies within the mirror bandwidth (Fig. 4.6) the most probable transitions are indicated by the purple arrows in the diagram.

In the case of krypton in this energy range resonant as well as non resonant Auger decay becomes probable indicated by the green arrows. Thus singly charged krypton originating from XUV photo ionization with a 3d vacancy decays predominantly to doubly charged krypton, but with a fraction of 30% also to triply charged krypton [91].

Contemporaneously highly excited neutral atoms in  $3d^{-1}np$  excited states are produced followed by Auger decay via intermediate states to singly and doubly charged krypton ions. These Auger decay channels are described by  $3d^{-1}np \rightarrow 4s^{-2}4p^6nl \rightarrow 4p^{-2}$  for the doubly charged krypton ion and  $3d^{-1}np \rightarrow 4p^{-2}np$  or lower for the singly charged krypton ion. A fraction of 10% will directly decay to triply charged krypton [92].

---



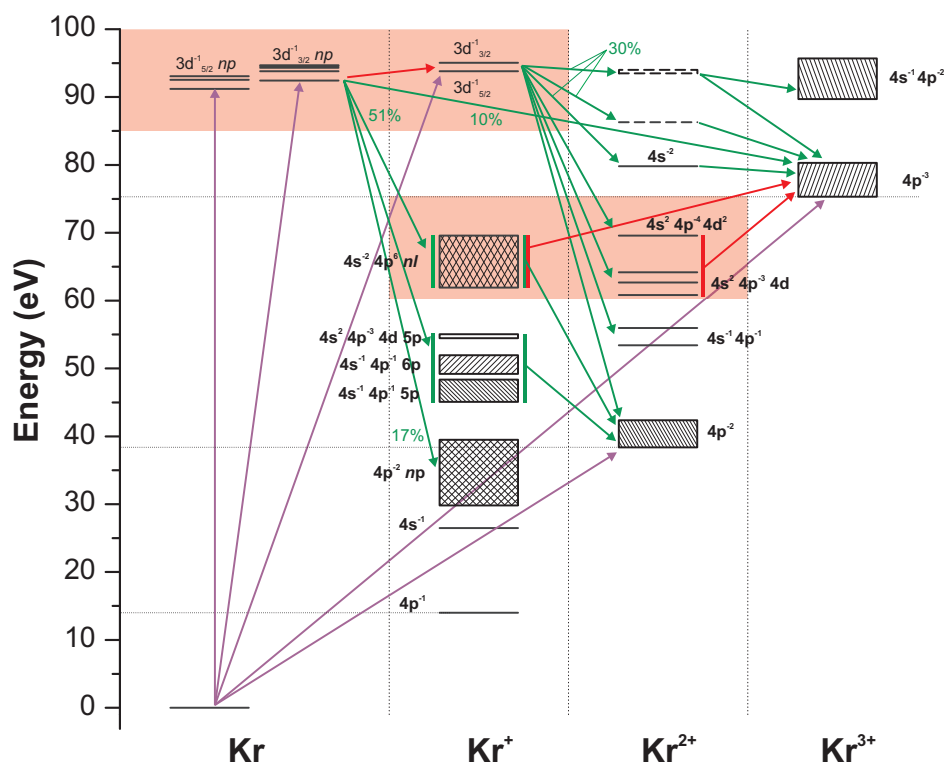


Figure 5.6: Transitions relevant for the described study. The energy levels shown are based on data published in [93, 94, 91, 95, 96]

The red shaded areas represent the minimum accessible energy bandwidth from the laser pulse under the condition that the laser intensity is adjusted producing only singly ionized krypton. The transitions probable from the interaction with the laser field are indicated by the red arrows.

In the generation of triply charged ions the time-dependent development of the ionization yield follows two competing processes resulting from the different probabilities and decay channels corresponding to the resonant and non-resonant Auger decays indicated by the numbers in the diagram.

The most obvious behavior originates from the normal Auger decay of the 3d vacancy in the singly charged ion. The Auger decay populates the intermediate states  $4s^2 4p^{-4} 4d^2$  and  $4s^2 4p^{-3} 4d$  with the decay constant related to the lifetime of the 3d vacancy of 7.9 fs [11]. These states are well below the triple ionization threshold and comparably long lived thus the laser induced depletion

of those levels samples the population of the levels caused by the Auger transition.

In the case of the resonant Auger decay an increase of the ionization yield in the  $Kr^{3+}$  ion can originate from three different channels and these channels are not independent which makes a complete interpretation difficult.

In the first case a normal Auger decay populates  $4s^{-2}4p^6 nl$  intermediate states with the same time constant for the decay of the  $3d^{-1}$  vacancy as given above. These states are depopulated by two competing processes. One is a second step Auger decay to the  $4p^{-2}$  ground state, while the other is the depopulation caused by the probe laser pulse.

The second channel is related to the probe laser pulse in the beginning of the decay cascade. The resonantly excited  $3d^{-1}np$  states are depleted by the probing laser pulse and thus the transition probability of 10% for the direct channel increases to 30% as for the decay of a singly charged ion with a pure 3d vacancy. Hence the transition is followed by an increase of the ionization yield in comparison to the direct transition by 20% and the initiation of the Auger transition is delayed by the interaction with the laser pulse.

For the third channel the laser needs to act on the atom twice initiating the channel for the normal Auger decay described above due to depletion of resonantly excited states  $3d^{-1}np$ .

Similar to the depletion of the  $2s^{-2}4p$  state in the tunneling ionization of neon the depletion of the excited  $np$  states in this case will happen in the wings of the laser pulse. Therefore, it is expected, that this channel becomes indistinguishable from the normal Auger decay to the intermediate states  $4s^24p^{-4}4d^2$  and  $4s^24p^{-3}4d$ .

Figure 5.7 shows the results of the experiment. The large negative delays are not shown since the ion yield remains constant corresponding to the XUV generated  $Kr^{3+}$  ions. This indicates also that the laser induced generation of singly charged krypton is not saturated otherwise XUV ionization of singly ionized krypton would become favorable for negative delays and an enhancement of the ionization yield would be observed in this delay range, as well.

The model to fit the experimental data and extract the time constants as described in Appendix D uses a 4.3 fs pulse duration as the probing function for the laser pulse and 7.9 fs for the  $3d^{-1}$  Auger decay from [11]. The laser pulse duration is chosen to be 4.3 fs to indicate that no ionization of the excited states

---

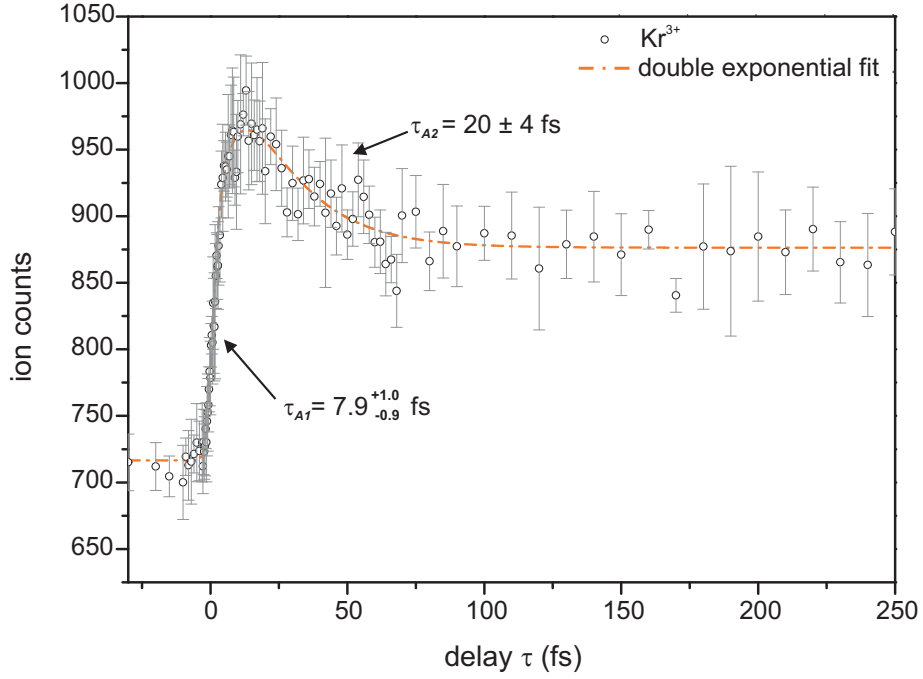
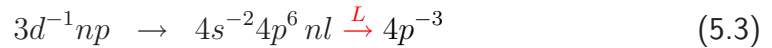
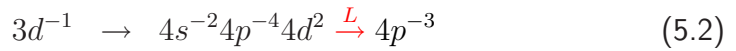
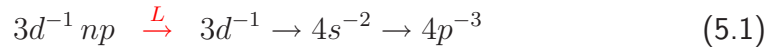


Figure 5.7:  $Kr^{3+}$  versus delay; the indicated time constants result from the model described in Appendix D; the laser intensity is in the range of  $4 \pm 1 \times 10^{13}$  W/cm<sup>2</sup>

occurs in the wings of the pulse. The shape of the curve is explained in terms of the channels described above assuming early depletion of the resonantly excited  $3d^{-1}np$  states. The sharp rising edge is determined by the decay of the initial vacancy. Under this assumption, the three routes to the triply charged ion can be addressed to this enhancement of the ionization yield determined by the following processes:



For large negative delays the direct transitions from the  $3d^{-1}$  and  $3d^{-1}np$  are not affected by the probe laser pulse and build a constant count rate for the XUV produced  $Kr^{3+}$  ions. For large positive delays the enhancement of the ionization yield follows the transition described by Eq. (5.2) since the  $4s^24p^{-4}4d^2$  state is long lived compared to the maximum delay range.

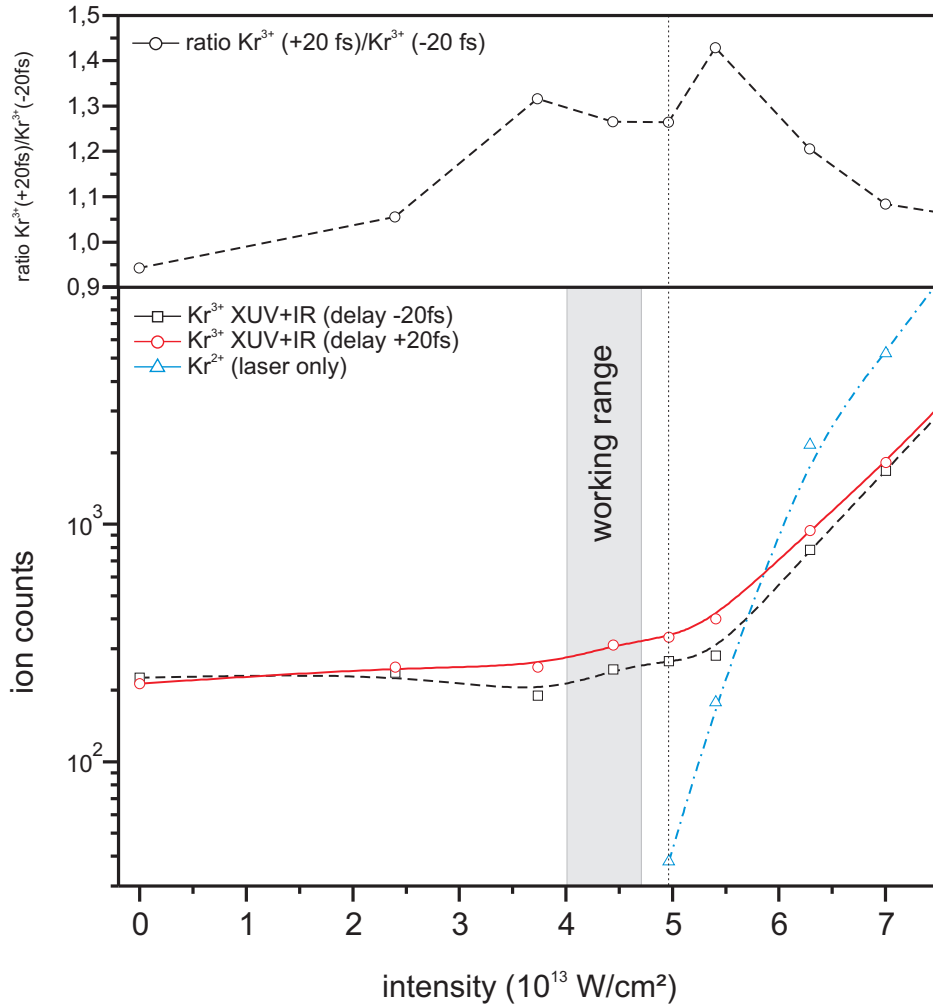
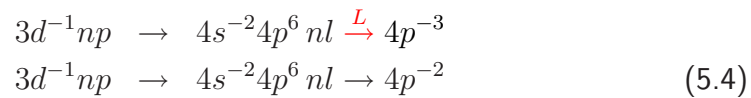


Figure 5.8: intensity dependent ionization yield of  $\text{Kr}^{3+}$  for two delay positions; the red circles indicate the intensity dependent behavior +20 fs delay; the black squares the intensity dependent behavior for -20 fs delay; the blue triangles depict the laser based ionization yield of the  $\text{Kr}^{2+}$  ions; in the upper graph the ratio  $\text{Kr}^{3+} (+20\text{fs})/\text{Kr}^{3+} (-20\text{fs})$  is shown. The dashed vertical line indicates the threshold intensity where we observe the first laser induced  $\text{Kr}^{2+}$  ions. From the number of ion counts in the  $\text{Kr}^{1+}$  (not shown here) the intensity where this measurement was performed was in the range indicated by the gray box around  $4 \pm 1 \times 10^{13} \text{ W/cm}^2$ . The lines are shown to guide the eye.

The decaying part of the peak is best explained by following the cascade



Where the depopulation of the intermediate state  $4s^{-2}4p^6 nl$  to  $Kr^{2+}$  dominates the depopulation to the  $Kr^{3+}$  caused by the laser pulse with increasing delay. This requires that the  $3d^{-1}np$  is not totally depleted by the laser because a substantial fraction needs to decay to the intermediate state  $4s^{-2}4p^6 nl$  to yield the depopulation process. Probing this behavior higher, laser intensities would open the channel for a population transfer from the  $4s^{-1}4p^{-1} np$  states to the  $4p^{-3}$  ground state. For large delays the increased ionization yield should change in magnitude if the  $4s^{-1}4p^{-1} np$  are involved or not, while the time constant for the Auger transition to the  $4p^{-3}$  ground state should remain the same.

A first indication to support this statement of an intensity dependent change in the ionization yield due to the accessibility of more strongly bound excited states in the  $4s^{-1}4p^{-1} np$  configuration is shown in Fig. 5.8. At laser intensities that create a substantial amount of  $Kr^{2+}$  ions, the ratio  $Kr^{3+}(+20fs)/Kr^{3+}(-20fs)$  becomes larger which could be the indication that the  $4s^{-1}4p^{-1} np$  states get depleted by the laser pulse as well. Thus for future experiments on krypton, measurements with varying intensities in small intensity steps are important.

Another possible interpretation is that the depletion is only significant in a delay range of 7.9 fs starting from the rising edge to explain the "overshoot" of the ionization enhancement., because the resonantly excited states are depleted by the Auger decay for delays larger than the lifetime of the 3d vacancy. Therefore, the laser pulse can only act on the  $4s^{-2}4p^6 nl$  intermediate state. Independent of the role of depletion in this process, the time constant  $\tau_{A2} = 20 \pm 4 fs$  for the decreasing edge of the measured curve is related to the second step Auger decay  $4s^{-2}4p^6 nl \rightarrow 4p^{-2}$  and therefore to the lifetime of the intermediate state involved in this decay cascade.

### 5.3 Multi-electron ionization dynamics in Xenon

In the last experiment multi-electron inner-shell relaxation of xenon atoms following excitation with the attosecond XUV pulse is explored. Due to the fact that xenon is a high Z-atom a variety of decay processes follow XUV excitation or ionization of an inner-shell electron.

Figure 5.9 shows the energy levels and transitions relevant to this experiment. As a consequence of the strong  $4d \rightarrow \epsilon f$  resonance in xenon [83] slightly above the excitation energy of 91 eV electrons from the 4d orbital will be preferably liberated.

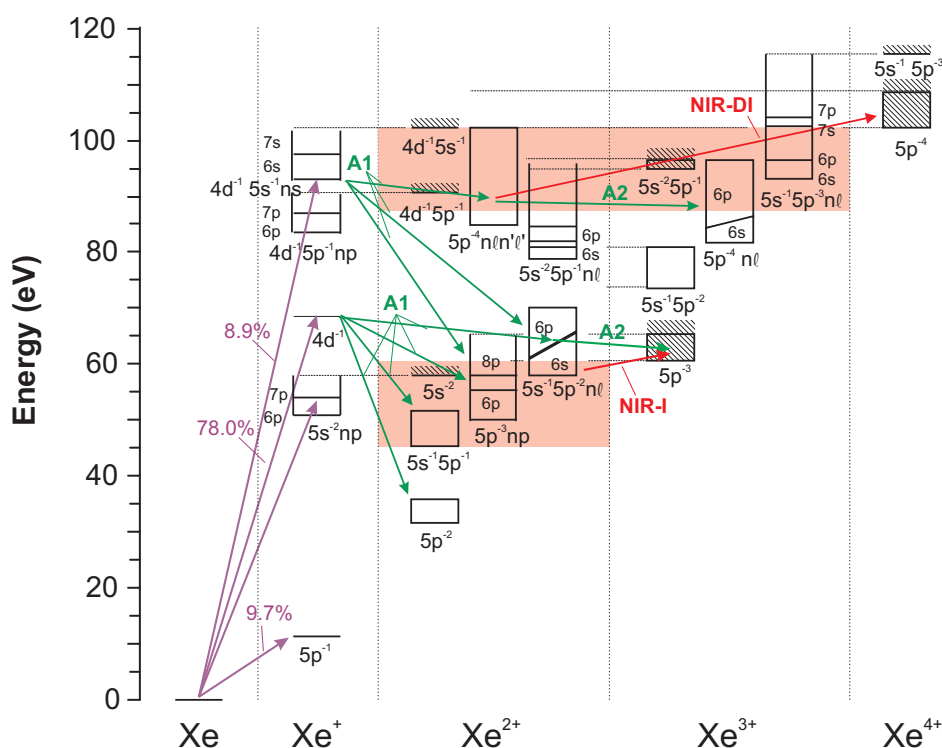


Figure 5.9: Energy levels and transitions in xenon ions relevant for the current study. The energy levels are based on data from *Kabachnik and Fritzsche* [97]. The relative population of states in  $Xe^{1+}$  is given for an XUV excitation energy of 90 eV [41]. Purple arrows indicate direct XUV photo ionization, green arrows subsequent Auger transitions, red arrows further ionization by the laser pulse

Referring to the ionization of an inner atomic shell in section 2.2 a vacancy will rapidly decay by single and cascaded Auger processes. This leads to higher ionic charge states with a high probability ( $\sim 99\%$ ). Furthermore, in the case of a  $4d^{-1}$  ionization additional shake-up and satellite states will be populated.

Regarding Fig. 5.9, a  $Xe^{1+}$  in one of the configurations  $4d^{-1}$ ,  $4d^{-1}5s^{-1}ns$  and  $5s^{-2}np$  will Auger decay through channels A1 to  $Xe^{2+}$ . Approximately 19% will decay further via a second Auger process following A1 and A2 depicted in Fig. 5.9 to  $Xe^{3+}$  according to photoelectron-ion coincidence measurements [98]. The complete description of all channels leading to the formation of a triply charged xenon ion include the probability of direct double Auger decay as mentioned in section 2.2 which is not shown in Fig. 5.9. The corresponding lifetimes of the individual levels are well known from synchrotron measure-

ments. From the linewidths measured by electron spectroscopy [99] the  $4d_{3/2}$  and  $4d_{5/2}$  lifetimes are extracted to be  $6.3 \pm 0.2 \text{ fs}$  and  $5.9 \pm 0.2 \text{ fs}$ , respectively.

As in the krypton measurement, the lifetime of the decay represented by A1 is only dependent on the decay of the 4d vacancy. Thus an enhancement of the ionization yield in the  $\text{Xe}^{3+}$  is related to the population of an intermediate level with a time constant related to the transition indicated by A1, that will be depopulated by the probing laser pulse. Those intermediate levels serving for the enhancement of the ionization yield in the  $\text{Xe}^{3+}$  are indicated by the small red shaded area covering the energy range from 45 eV up to the  $5p^{-3}$  threshold in Fig. 5.9.

The first Auger process A1 populates more strongly bound states such as  $5s^{-1}5p^{-2}6p$  and Rydberg states in the configuration  $5p^{-3}np$  below this threshold where no further decay is possible. The additional energy transferred from the laser pulse gives rise to overcome the  $5p^{-3}$  threshold from those levels and results in a triply charged xenon ion. The bandwidth of the area satisfies the condition that the laser produces only singly charged xenon ions, thus the maximum energy transferred from the laser pulse is below 33 eV.

Creation of  $\text{Xe}^{3+}$  by the XUV pulse is dominated by cascaded double Auger transition mainly via two intermediate states, presumably  $5s^{-1}5p^{-2}7p$  [100, 96]. Furthermore, the configurations  $4d^{-1}5p^{-1}np$  and  $4d^{-1}5s^{-1}ns$  yield for a cascaded decay to the  $\text{Xe}^{3+}$ . The decay of those states results in the constant XUV yield for large negative delays in relation to the XUV cross-sections measured in synchrotron experiments [83] and calculated for the broadband reflectivity of our XUV mirror in Tab. 4.1.

Figure 5.10 shows the measured curve of the ion count rate versus delay at the laser intensity of  $(7 \pm 1) \times 10^{13} \text{ W/cm}^2$  used in this experiment. For positive delays a rapid exponential increase is observed in the ionization yield from the background in the  $\text{Xe}^{3+}$  signal that arises from the A1+A2 Auger cascade discussed above. The laser-induced increase in the  $\text{Xe}^{3+}$  yield is due to ionization from the states in  $\text{Xe}^{2+}$  in configurations  $5p^{-3}np$ ,  $5s^{-1}5p^{-1}$  and  $5s^{-1}5p^{-2}nl$  indicated in Fig. 5.9.

No decay of the enhanced  $\text{Xe}^{3+}$  yield was observed up to our maximum delay of 300 fs, indicating a lifetime of the involved intermediate states longer than one picosecond. The exponential increase in the  $\text{Xe}^{3+}$  signal is the convolution of the A1 decay and the laser induced ionization process (denoted by NIR-I in Fig. 5.9) with the temporal evolution of the A1 process known from synchrotron

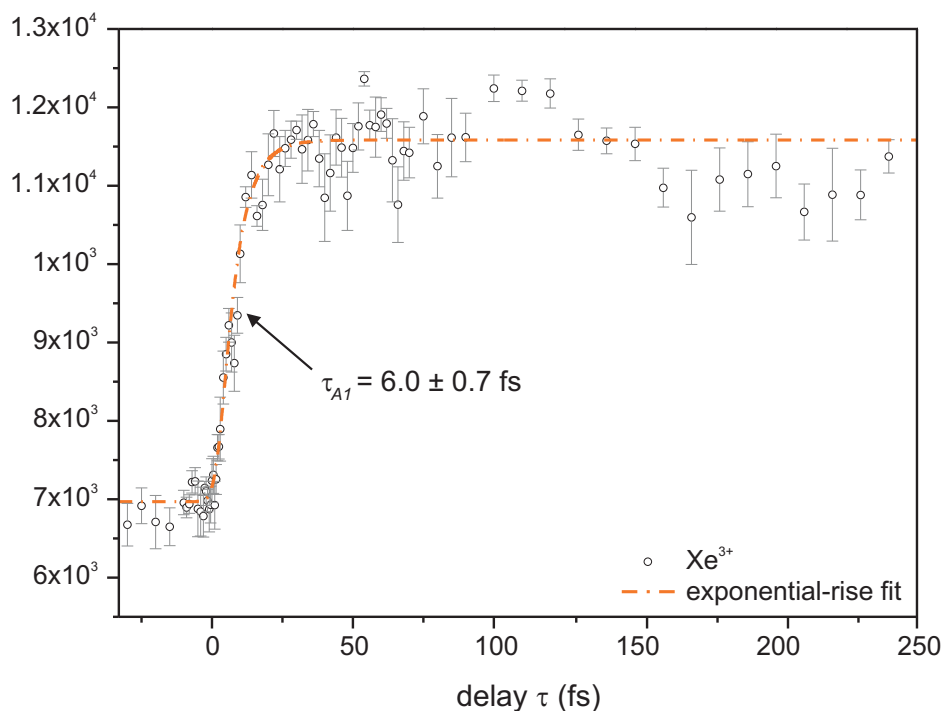


Figure 5.10:  $\text{Xe}^{3+}$  versus delay; the indicated time constant result from the model described in Appendix D

measurements [99].

With a 6 fs decay time for A1 that is extracted from the time dependent dynamics of the  $\text{Xe}^{4+}$  presented below, the temporal evolution of the laser-induced transition responsible for the increase of the  $\text{Xe}^{3+}$  yield for  $\tau > 0$  becomes accessible and is extracted from the exponential rise giving a laser-induced ionization time of  $5.8 \pm 2.5$  fs (full width at half maximum). This indicates that low order, one- and/or two-photon, transitions may promote electrons from the corresponding states of  $\text{Xe}^{2+}$  to the  $5p^{-3}$  states of  $\text{Xe}^{3+}$  because the extracted laser pulse duration can be interpreted as a contribution of the complete laser pulse to the ionization of the excited states. Therefore even small intensities in the wings of the pulse, corresponding to one- and two-photon processes lead to an enhancement of the ionization yield.

From Fig. 5.9 one can see that charge-states higher than  $\text{Xe}^{3+}$  cannot be created with the XUV pulse alone because the XUV photon energy is well below the  $\text{Xe}^{4+}$  threshold of about 105 eV. The corresponding energy bandwidth



accessible for the laser pulse is denoted by the red shaded area, again.

With the laser pulse transferring additional energy to the xenon ions the generation of  $\text{Xe}^{4+}$  ions is observed for a restricted range of positive delays.

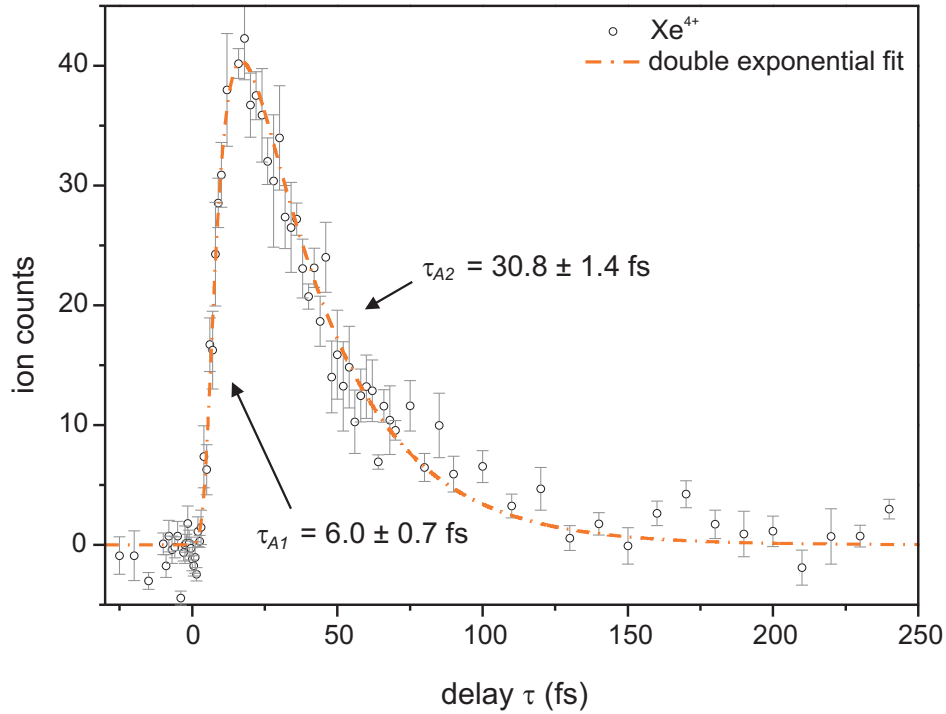


Figure 5.11:  $\text{Xe}^{4+}$  versus delay; the indicated time constants result from the model described in Appendix D

Figure 5.11 depicts the delay dependent behavior of the laser induced generation of the  $\text{Xe}^{4+}$  ions. The ionization yield exponentially increases within a few femtoseconds followed by a long exponential decay on a time scale of several tens of femtoseconds. The  $\text{Xe}^{4+}$  generation is currently believed to be provoked by laser-induced double ionization (denoted by NIR-DI in Fig. 5.9) from the intermediate states in configurations  $5p^{-4}nl n'l'$  (*doubly-excited*) and/or  $5s^{-2}5p^{-1}nl$  (*singly-excited*) states of  $\text{Xe}^{2+}$ .

These states are populated by the first Auger process A1, from the satellites  $4d^{-1}5p^{-1}nl$  of the  $4d^{-1}$  state upon emission of near-zero energy photoelectrons [101, 99] and depopulated by the second Auger decay A2 to states of much larger binding energy in  $\text{Xe}^{3+}$ , which cannot be reached by the probing laser pulse.

Thus the exponential rise and decay of the  $\text{Xe}^{4+}$  signal is based on the evolution of the first (A1) and second (A2) Auger decay in the same manner as the decreasing edge in the  $\text{Kr}^{3+}$  has been explained. The intermediate states corresponding to the generation of  $\text{Xe}^{4+}$  are populated by the first Auger decay A1, sampled in the rising edge and depopulated by the Auger decay A2, sampled in the falling edge, because the depopulation due to the Auger decay is competing with the depopulation from the probing laser pulse. Note that this neglects the exact nature of the process referring to section 2.2.3. The laser-induced double ionization may be either sequential or non-sequential and the cascade decay may eject a fast electron at the beginning of the cascade or at the end. The presented technique of *attosecond time-resolved ionization chronoscopy* averages over all possible channels resulting in the formation of a  $\text{Xe}^{4+}$  ion from all contributing states inside the red shaded area of Fig. 5.9.

Fitting the result of a simple rate-equation analysis including the transitions A1 and A2 to the  $\text{Xe}^{4+}$  data shown in Fig. 5.11 yields decay times of  $\tau_{A1} = 6.0 \pm 0.7 \text{ fs}$  and  $\tau_{A2} = 30.8 \pm 1.4 \text{ fs}$  for the A1 and A2 Auger processes.

While the A1 decay is to be accurately known from measurements in the energy domain[99] hitherto it has only been possible to set a lower limit of  $23 \text{ fs}$  for A2. Both time constants are in accordance with the results of energy-resolved measurements [99]. Therefore this sampling technique unfolds processes on a few-femtosecond or longer time scale and with sub-femtosecond resolution, but on the basis of formation of "forbidden" charge states assisted by laser-induced ionization.

The presented measurements give for the first time direct access to measurement of the time constant for the averaged lifetime of the intermediate states related to the double/cascade Auger decay for the  $\text{Xe}^{3+}$  formation in the XUV spectral range defined by the mirror reflectivity (see Fig. 4.6).

---

## Chapter 6

### Conclusions and outlook

In the framework of this thesis a novel apparatus for the application of attosecond time-resolved measurements has been built and characterized. It relies on the principles of pump-probe measurements previously used for attosecond studies of inner-shell processes [11] and sampling of the electric field of a few-cycle laser pulse [12] but this time based on ion detection sampling transient electronic states populated by a sub-femtosecond XUV pulse. This novel apparatus was developed with the aim to improve the experimental setup in terms of UHV conditions, vibration isolation, High Harmonic throughput and focusing on the application for measurements regarding ionization dynamics.

To this end, new pumping schemes were applied to support more effective differential pumping. Concepts for better vibration isolation were implemented and the High Harmonic throughput was optimized by reduction of background pressure.

The novel setup was characterized by simulating and measuring the focus sizes in the target region, specifying divergence and spot size of the incident High Harmonic beam and adjusting the *cutoff* range using a transmission grating spectrometer to resolve the High Harmonic spectrum. Finally this setup was used for *ionization chronoscopy* in rare gas atoms studying dynamics in the ionization processes of neon, krypton and xenon with sub-femtosecond resolution utilizing a reflectron ion mass spectrometer.

The measurements demonstrate the capability of ionization chronoscopy to study light induced tunneling processes and inner-shell cascade decays in real time by probing transient populations of short lived atomic states that have been populated with an attosecond XUV pulse.

---

Especially the study of resonant Auger decay in krypton and the double/sequential Auger decay in xenon demonstrates that *ionization chronoscopy* is a powerful tool to study two step processes in multi-electron atoms. Since all generated ionic charges are measured simultaneously even higher order cascade processes are accessible with this technique.

Although the second step Auger decay has been under investigation in the energy domain for more than two decades, measurements in the energy domain fail to define the mean lifetime of intermediate states involved in this decay cascades [96, 44]. Several reasons can be addressed to this problem. The mixing of direct double Auger and sequential Auger decay represents only one difficulty, that can be overcome by attosecond pump-probe techniques.

*Ionization chronoscopy* turns out to be a tool of choice for studying these processes, because it is insensitive to the different final electrons only on the occupied initial states and the final ion. Contemporaneously this reflects the main disadvantage of the technique. All measurements of this kind need interpretation because the information on the binding energy of the ionized electron is lost. Furthermore, this method integrates over all occupied states below the ionization threshold that are accessible for the laser pulse.

Even as the experimental importance of this technique becomes clear, theoretical modeling of the described processes is quite complex and is currently under investigation [102]. This is one of the reasons that only a qualitative explanation is presented in the cases of krypton and xenon.

Moreover, the developments regarding the production of isolated attosecond pulses with a high conversion efficiency [17] and laser developments towards the single-cycle regime [15] at high pulse energies support the establishment of attosecond physics and it becomes reasonable to think about XUV-XUV pump-probe schemes.

As an outlook for the new developments in this field I want to mention the successful application of this technique to solid state physics. During the time of this thesis I was also involved in setting up an attosecond solid state experiment, that finally resolved a streaking effect in the electron spectrum comparable to [12]. Utilizing attosecond-pump probe techniques for solid state experiments and with increasing photon energies for the XUV pulse opens up a vast range of target material for physical investigation with ultrafast dynamics in the attosecond time scale.

---

Another new and interesting route is the application of different spectrometers for these experiments. The use of *COLTRIMS* (*COLd Target Recoil Ion Momentum Spectroscopy*) detectors and *VMI* (*Velocity Map Imaging*) detectors have been discussed and first tests with a VMI were already performed and show promising results. Extracting additional information from the angular distribution of electrons or ions would give more tools to isolate effects performing measurements in the time domain that cannot be treated or resolved in the energy domain. Concerning the *COLTRIMS* it strongly combines the benefits of both worlds, being highly selective for the process under observation in the energy domain and resolving time dependent dynamics on the attosecond time scale.

It is even possible to think of Spin resolved measurements utilizing Mott detection, but to come closer to this many improvements are still required, especially in terms of XUV flux which is already under investigation [17].



# Appendix A

## - Vacuum Layout

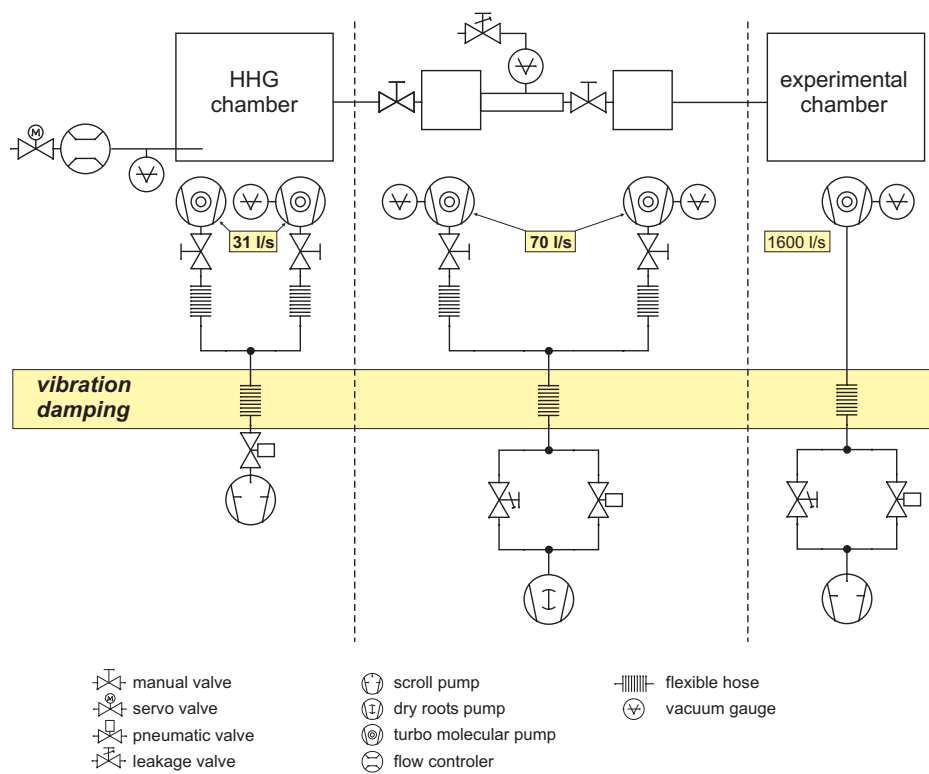


Figure 1: vacuum layout of the beamline AS-1





## Appendix B

### - "Soft" - Knife Edge

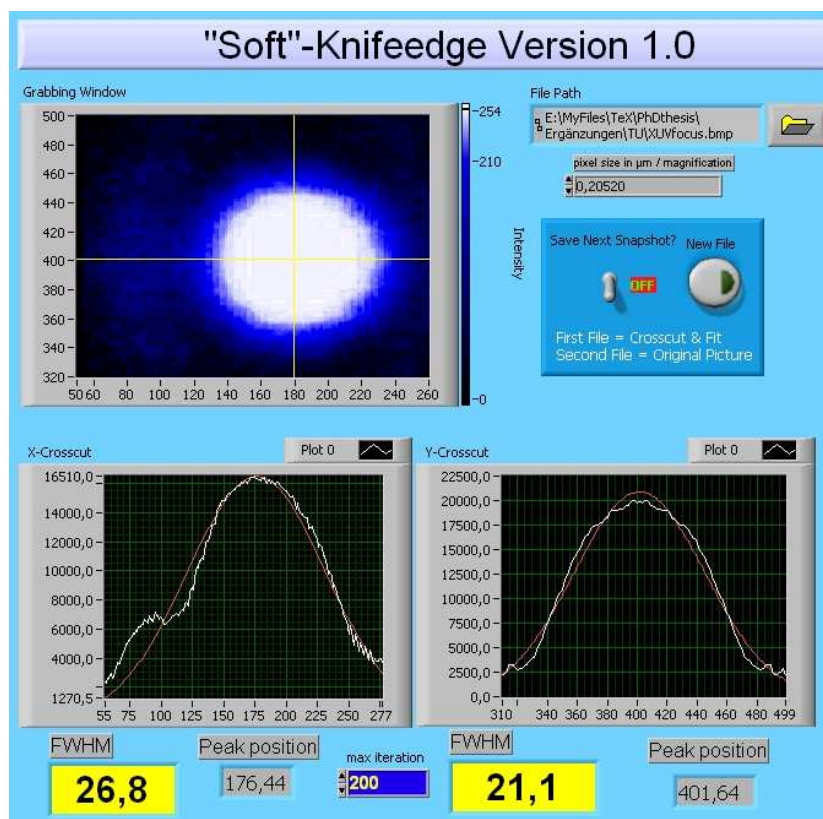


Figure 2: User Interface of the "Soft" Knife edge software

The most simple technique of the beam profile analysis is so-called *knife-edge technique*. In the classical setup that is even commercially available for beam profile analysis the beam is gradually blocked by a razor blade and the passing residual light is measured with a photodiode. The measured signal is

proportional to the intensity as a function of the knife-edge position integrating over the remaining intensity in two dimensions. Fitting the retrieved profile with a Gaussian error function leads to the parameters for a gaussian shaped beam profile.

This technique was utilized and combined with image acquisition where the razor blade position is realized reducing the image array row by row and integrating over the resulting array in two dimensions. This is done in x- and y- direction and the resulting graph as a function of the row or column number is numerically differentiated and fitted with a Gaussian function. Obtaining kind of an effective Gaussian shaped focus resulting in the same intensity profile. A calibration parameter can be entered to match the real dimension, knowing the pixel size of the camera and the magnification of the image. The software is shown in Fig. 2 with an example image where the profiles are extracted.

---

## Appendix C

### - $\gamma$ -parameter neon

Table 1 is based on the data published in [94]. The XUV photon energy used in that work was equal to 96 eV, which is very close to the one used in the experiments on attosecond tunnelling spectroscopy. Since the fine-structure splitting is irrelevant for these experiments, the fine-structure states belonging to the same configuration were grouped together.

configuration	$W_b$ , eV	line in- tensity, arb. units	barrier- suppression intensity, W/cm <sup>2</sup>	$\gamma_s$
$2s^2 2p^4(^3P)3s$	13.17	0.3	$3.0 \cdot 10^{13}$	2.0
$2s^2 2p^4(^1D)3s$	13.60	4.2	$3.4 \cdot 10^{13}$	1.9
$2s^2 2p^4(^3P)3p$	9.712	4.9	$8.9 \cdot 10^{12}$	3.2
$2s^2 2p^4(^1D)3p$	10.00	14.4	$1.0 \cdot 10^{13}$	3.1
$2s^2 2p^4(^1S)3s$	13.55	7.2	$3.4 \cdot 10^{13}$	2.0
$2s^2 2p^4(^3P)3d$	6.102	1.3	$1.4 \cdot 10^{12}$	6.5
$2s^2 2p^4(^3P)4s$	5.967	0.1	$1.3 \cdot 10^{12}$	6.7
$2s^2 2p^4(^3P)4p$	4.562	3.2	$4.3 \cdot 10^{11}$	10.0
$2s^2 2p^4(^3P)4d$	3.396	0.5	$1.3 \cdot 10^{11}$	15.6
$2s^2 2p^4(^1S)3p$	9.967	4.4	$9.9 \cdot 10^{12}$	3.1
$2s^2 2p^4(^1D)3d$	6.170	2.2	$1.4 \cdot 10^{12}$	6.4
$2s^2 2p^4(^1D)4p$	4.815	2.5	$5.4 \cdot 10^{11}$	9.2
$2s^2 2p^4(^1S)3d$	6.199	1.0	$1.5 \cdot 10^{12}$	6.3

Table 1: Atomic states of Neon, based on [94], see text for details.

We see that with  $\lambda = 740$  nm the  $\gamma \leq 1$  regime is not accessible for any of the states. However, the tunnelling ionization remains significant even if  $\gamma > 1$ , just

the relative efficiency of the multiphoton ionization becomes increasingly higher with larger values of  $\gamma$ . Figure 3 shows the ionization rate of the  $2p^{-2}(^3P)3s$  state calculated for different values of  $\gamma$  using the generalization of the ADK theory, which is applicable to the intermediate regime [89]. Even for  $\gamma = 5$  sub-cycle ionization dynamics is visible.

This theory also provided a basis for the simulations presented in Fig. 5.4. In these simulations we assumed that the XUV pulse instantaneously populates the shake-up states and that the interaction of the XUV pulse with the atom is not influenced by the laser field.

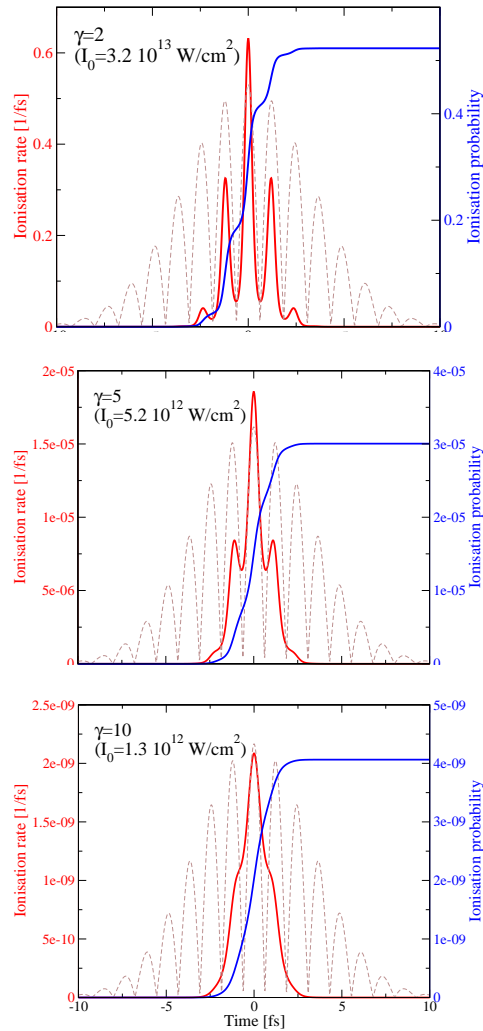


Figure 3: ADK calculations (see text).

## Appendix D

### - Data analysis

#### Rise time of the steps in the $\text{Ne}^{2+}$ signal

The fact that the probability of double ionization has the step-like dependency on the delay indicates that the processes must happen on a subfemtosecond time scale. Indeed, neither the time during which the shaken-up state is populated, nor the time during which the tunnelling ionization channel is open can exceed the rise time of observed steps. In order to place an upper limit on these times the noise, with which the data were measured, must be taken into consideration.

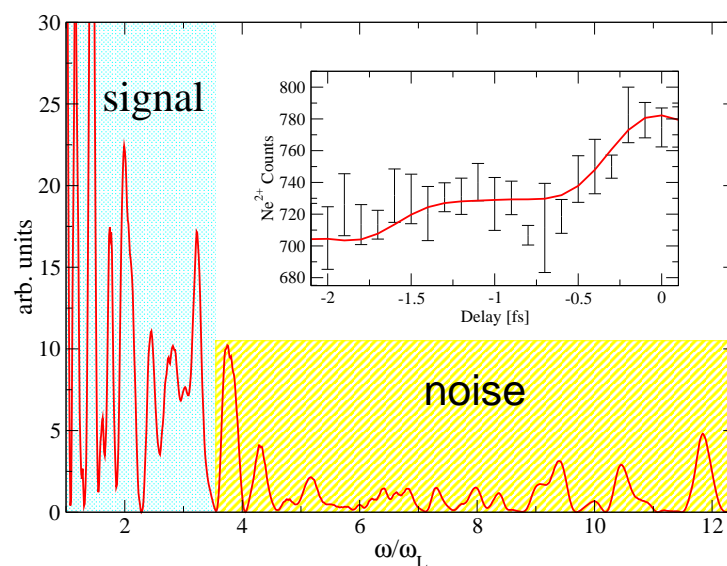


Figure 4: Noise suppression in the  $\text{Ne}^{2+}$  signal. The inset shows the original data and the filtered signal.

In Fig. 4 the power spectrum of the signal is plotted versus frequency normalized to the central frequency of the laser pulse. The fact that the steps occur two times per laser period is clearly manifested by the peak at  $\omega = 2\omega_L$ .

The part of the spectrum at high frequencies is dominated by noise. By suppressing those spectral components we filter the noise out of our data by simultaneously broaden the steps. In general, it is not possible to precisely separate signal from noise, but we believe that by suppressing all spectral components larger than  $3.5\omega_L$  we place a reasonable upper limit on the step rise time.

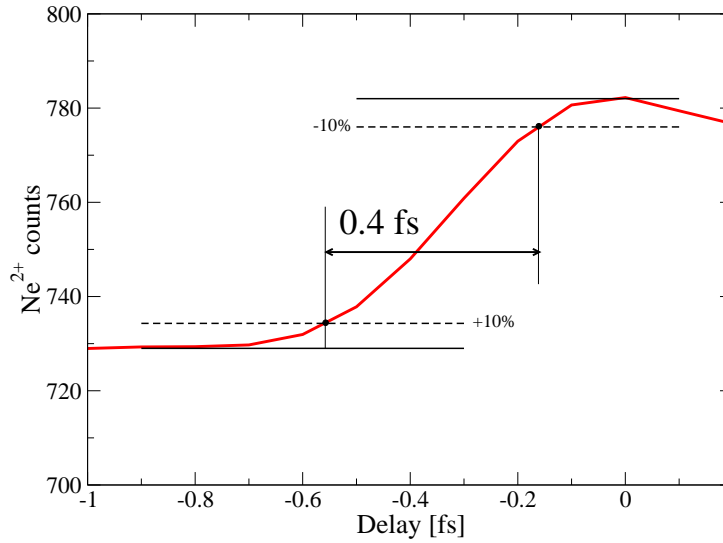


Figure 5: Determination of the step rise time.

The procedure that we used to quantify the step rise time is illustrated in Fig. 5. First, we determine the values of the signal before and after a step. After that we are searching for the delays, at which the relative change of the signal amounts to 10%. The interval between these delays is defined as the rise time of the step, which we find to be equal to 400 attoseconds.

## Error bars

In order to estimate the accuracy of the measurement and to minimize the impact of slow drift of different parameters the data were collected in several runs by scanning the delay from its minimal to its maximal value a few times. After that the data  $y_n(\tau)$  obtained in runs 2, 3, etc. was scaled and shifted in order to minimize the discrepancy with run 1 (see Fig. 6 for the  $\text{Xe}^{4+}$  data as an example):

$$y_n^{\text{new}}(\tau) = ay(\tau) + b, \quad (1)$$

$$\sum_i |y_n^{\text{new}}(\tau_i) - y_1(\tau_i)|^2 \rightarrow \min. \quad (2)$$

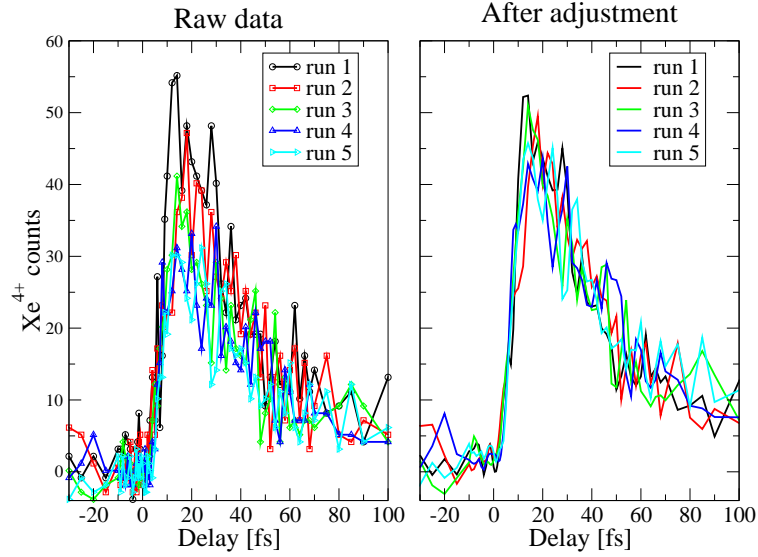


Figure 6: Adjustment of individual runs of the  $\text{Xe}^{4+}$  data.

After this adjustment the runs were averaged and the standard error was calculated for each delay. The magnitude of the error bars in Figures 5 and 7 of the main paper are equal to twice the standard error. Note that large fluctuations in the ion yield signals may result from XUV intensity variations as becomes evident from Fig. 7, where the temporal evolution of ion yield ratio  $\text{Xe}^{3+}/\text{Xe}^{2+}$  is shown.

### Fitting the temporal profiles

The temporal profiles are fitted with model functions that result from a convolution of a Gaussian representing the IR laser pulse width and the following exponential functions

$$A(t) = A_1 \left( 1 - \exp \left( -\frac{(t - t_0)}{\tau_1} \right) \right) \quad (3)$$

$$B(t) = B_1 \left( \exp \left( -\frac{(t - t_0)}{\tau_1} \right) - \exp \left( -\frac{(t - t_0)}{\tau_2} \right) \right) \quad (4)$$

for the evolution of the  $\text{Xe}^{3+}$  and  $\text{Xe}^{4+}$  ion yields, respectively. A constant offset was added to the fit functions to account for signal before time zero that originates from XUV only. The weighted fits to the data are optimized by a home written program [103] via the Levenberg-Marquardt algorithm as implemented in the Curve Fitting Toolbox 1.2 in Matlab R14. Errors in given time constants represent 95% confidence intervals.

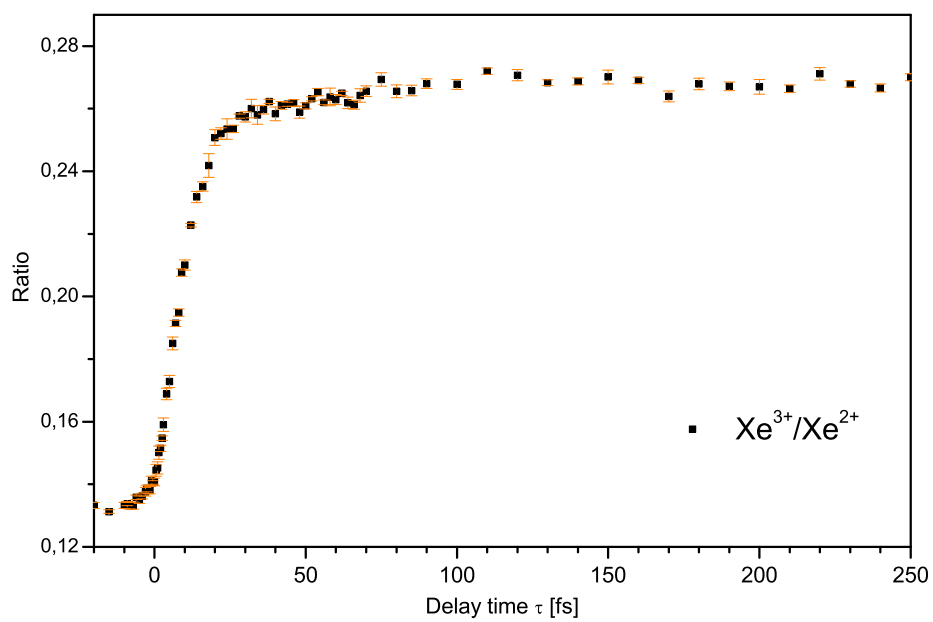


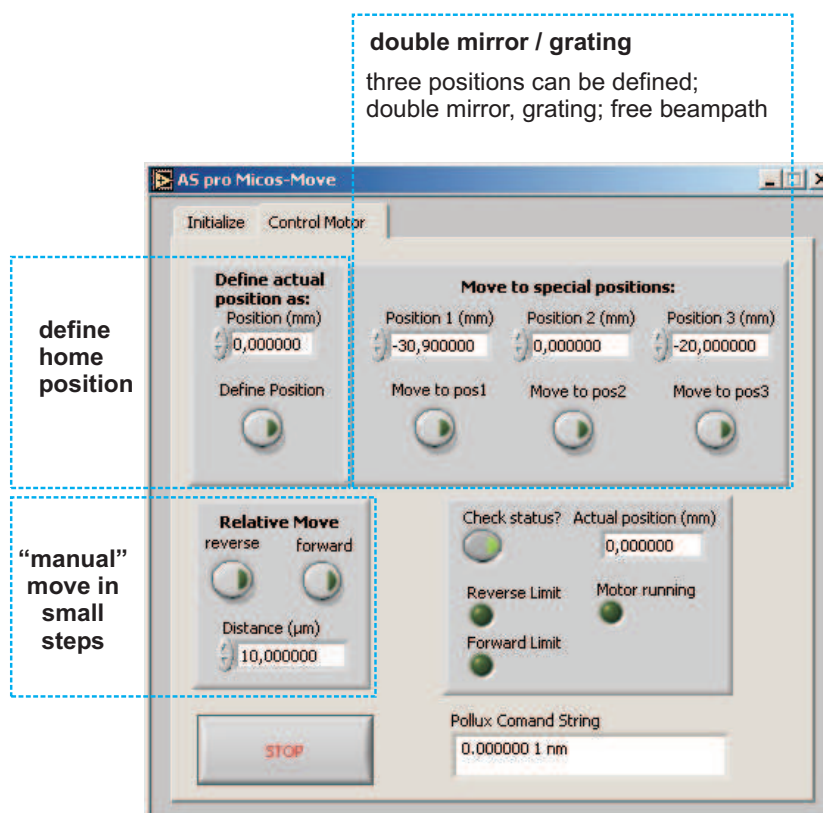
Figure 7: Temporal evolution of the  $\text{Xe}^{3+}/\text{Xe}^{2+}$  ratio.



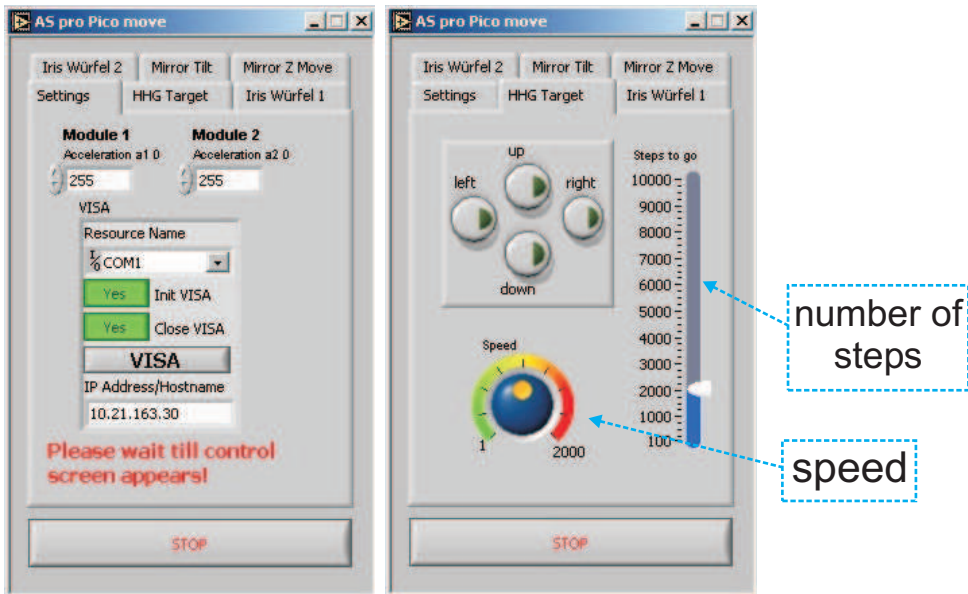
# Appendix E

## - Measurement and Automation Software

### Double Mirror assembly and Transmission Grating adjustment

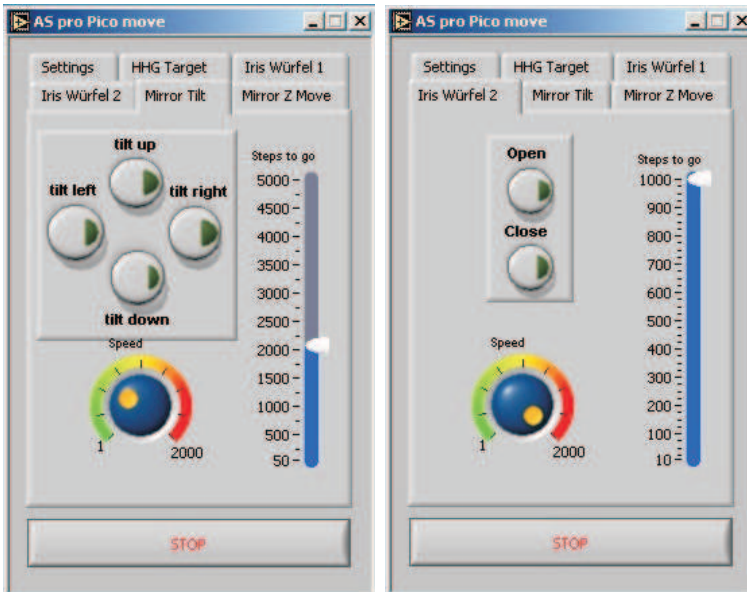


### Optics adjustment



**settings**

**HHG Target**



**double mirror  
tip/tilt**

**Iris adjustment**

Measurement and Optimization software

**Measurement Window**

optional online data analysis

start measurement

integration time

Delay stage controls  
adjustment of the experimentally determined pulse overlap position

Delay determination  
adjustment of the delay steps, it is possible to select between a predefined ASCII table or a linear scan with a fix step width

zoom into data  
the sliders allow to zoom a selected range in the data window

**Optimization Window**

adjusting averages progress indicator

ion yield  
ion yield in the area selected with the red and blue cursor. The area is selected with the sliders below the graph.

count rate indicators

**Settings Window**

parameters multiscaler

path- and filenames

delay stage parameters



## Bibliography

- [1] Einstein, A.:  
Ann. d. Phys. **17**, 132 (1905)
  - [2] Auger, P.:  
J. Phys. Radium **6**, 205 (1925)
  - [3] Blewett, J. P.:  
Phys. Rev. **69**, 87 (1946)
  - [4] Elder, F. R.; Gurewitsch, A. M.; Langmuir, R. V.:  
Phys. Rev. **71**, 829 (1947)
  - [5] Strickland, D.; Mourou, G.:  
Opt. Commun. **56**, 219 (1985)
  - [6] Agostini, P.; DiMauro, L. F.:  
Rep. Prog. Phys. **67**, 813 (2004)
  - [7] Hentschel, M. *et al.*:  
Nature **414**, 509 (2001)
  - [8] Kienberger, R. *et al.*:  
Nature **427**, 817 (2004)
  - [9] Kienberger, R. *et al.*:  
Science **297**, 5584 (2002)
  - [10] Drescher, M. *et al.*:  
Science **291**, 1923 (2001)
  - [11] Drescher, M. *et al.*:  
Nature **419**, 803 (2002)
  - [12] Goulielmakis, E. *et al.*:  
Science **305**, 1267 (2004)
-

- 
- [13] Gauthier, J.-C.; Rousse, A.:  
J. Phys. IV France **12**, Pr5 (2002)
- [14] Ross, I. N. *et al.*:  
Opt. Commun. **144**, 125 (1997)
- [15] Kobayashi, T.; Baltuska, A.; :  
Meas. Sci. Technol. **13**, 1671 (2002)
- [16] Ishii, N. *et al.*:  
Opt. Lett. **30**, 567 (2005)
- [17] Tsakiris, G. D.; Eidmann, K.; Meyer-ter-Vehn, J.:  
New J. Phys. **8**, 19 (2006)
- [18] Sansone, G. *et al.*:  
Science **314**, 443 (2006)
- [19] Keldysh, L. V.:  
J. Exptl. Therot. Phys. (U.S.S.R.) **47**, 1945 (1964)
- [20] Protopapas, M.; Keitel, C. H.; Knight, P. M.:  
Rep. Prog. Phys. **60**, 389 (1997)
- [21] Ivanov, M. Y.; Spanner, M.; Smirnova, O.:  
J. Mod. Opt. **52**, 165 (2005)
- [22] Landauer, R., Martin, Th.:  
Rev. Mod. Phys. **66**, 217 (1994)
- [23] Hauge, E. H.; Stoevng, J. A.:  
Rev. Mod. Phys. **61**, 917 (1989)
- [24] Faisal, F. H. M.:  
J. Phys. B: At., Mol. Opt. Phys. **6**, L89 (1973)
- [25] Reiss, H. R.:  
Phys. Rev. A **22**, 1786 (1980)
- [26] Reiss, H. R.:  
Phys. Rev. A **42**, 1476 (1990)
- [27] Bauer, Jaroslaw:  
Phys. Rev. A **73**, 023421 (2006)
- [28] Augst, S.; Meyerhofer, D. D.; Strickland, D.:  
J. Opt. Soc. Am. B **8**, 858 (1991)
-

- 
- [29] Ammosov, M. V.; Delone, N. B.; Krainov, V. P.:  
Zh. Eksp. Teor. Fiz. **91**, 2008 (1986)
- [30] Perelomov, A. M.; Popov, V. S.; Terent'ev:  
J. Exptl. Therot. Phys. (U.S.S.R.) **23**, 924 (1965)
- [31] Scrinzi, A.; Geissler, M.; Brabec, T.:  
Phys. Rev. Lett. **83**, 706 (1999)
- [32] Yergeau, F.; Petite, G.; Agostini, P.:  
J. Phys. B: At., Mol. Opt. Phys. **19**, L663 (1986)
- [33] Lindner, Fabrizio:  
*Atoms in intense ultrashort laser pulses and the absolute phase*,  
PhD Thesis, Ludwig-Maximilians-Universität München, 2004
- [34] Geissler, M. *et al.*:  
Phys. Rev. Lett. **83**, 2930 (1999)
- [35] Lewenstein, M. *et al.*:  
Phys. Rev. A **49**, 2117 (1994)
- [36] Corkum, P. B.:  
Phys. Rev. Lett. **71**, 1994 (1993)
- [37] Siffalovic, Peter:  
*Femtosecond Time-Resolved Photoelectron Spectroscopy  
in the Extreme Ultraviolet Region*,  
PhD Thesis, Universität Bielefeld, Germany, 2002
- [38] Usachenko, V. I.; Pazdzersky, V. A.:  
J. Phys. B: At., Mol. Opt. Phys. **35**, 761 (2002)
- [39] Becker, U. *et al.*:  
Phys. Rev. Lett. **63**, 1054 (1989)
- [40] Carlson, T. A.; Nestor, C. W. Jr.; Tucker, T. C.:  
Phys. Rev. **169**, 27 (1968)
- [41] Becker, Uwe; Shirely, D. A.:  
*VUV and Soft X-Ray Photoionization*,  
Plenum Press, New York, 1996
- [42] Nolan, P. J.; Sharpey-Schafer, J. F.:  
Rep. Prog. Phys. **42**, 1 (1979)
- [43] Fink, R. W.; Jopson, R. C.; Swift, C. D.:  
Rev. Mod. Phys. **38**, 513 (1966)
-

- 
- [44] Lablanquie *et al.*:  
Phys. Rev. Lett. **87**, 053001 (2001)
- [45] Coster, D.; Kronig, R. De L.:  
Physica **2**, 13 (1935)
- [46] Lebedev, V. S.; Beigman, I. L.:  
*Physics of Highly Excited Atoms and Ions*,  
Springer, Berlin, Heidelberg, New York, 1998
- [47] van Dyck, R. S. Jr.; Johnson, Ch. E.; Shugart, H. A.:  
Phys. Rev. A **5**, 991 (1972)
- [48] Adam, M. Y. *et al.*:  
Phys. Rev. A **49**, 1797 (1994)
- [49] Gemmell, D. S.; Holland, R. E.:  
Phys. Rev. Lett. **14**, 945 (1965)
- [50] Burhop, E. H. S.:  
*The Auger Effect - and other radiationless transitions*,  
Cambridge University Press, Cambridge, 1952
- [51] McGuire, E. J.:  
Phys. Rev. A **2**, 273 (1970)
- [52] French, P. W. M.:  
Rep. Prog. Phys. **58**, 169 (1995)
- [53] Rullière, C.:  
*Femtosecond Laser Pulses - Principles and Experiments*,  
Springer, Berlin, Heidelberg, New York, 1998
- [54] Diels, Jean-Claude; Rudolph, Wolfgang:  
*Ultrashort Laser Pulse Phenomena*,  
Academic Press, San Diego, New York, London, 1995
- [55] Fork, R. L.; Martinez, O. E.; Gordon, J. P.:  
Opt. Lett. **9**, 150 (1984)
- [56] Mayer, E. J. *et al.*:  
Opt. Lett. **22**, 528 (1997)
- [57] Tempea, G.; Krausz, F.; Spielmann, Ch.:  
IEEE J. Sel. Top. Quant. **4**, 193 (1998)
- [58] Moulton, P. F.:  
J. Opt. Soc. Am. B **3**, 125 (1986)
-



- 
- [59] Koechner, W.:  
*Solid-State Laser Engineering*,  
Springer, Berlin, Heidelberg, New York, 1999
- [60] Milosevic, N.; Tempea, G.; Brabec, T.:  
Opt. Lett. **25**, 672 (2000)
- [61] Vozzi, C. *et al.*:  
Appl. Phys. B **80**, 285 (2005)
- [62] Hauri, C. P. *et al.*:  
Appl. Phys. B **79**, 673 (2004)
- [63] Hentschel, M.; Cheng, Z.; Krausz, F.:  
Appl. Phys. B **70**, S161 (2000)
- [64] Brabec, T.; Krausz, F.:  
Rev. Mod. Phys. **72**, 545 (2000)
- [65] Rauschenberger, J. *et al.*:  
Laser Phys. Lett. **3**, 37 (2006)
- [66] Mairesse, Y. *et al.*:  
Science **302**, (2003)
- [67] Goulielmakis, Eleftherios:  
*Complete Characterization of Light Waves using Attosecond Pulses*,  
PhD Thesis, Ludwig-Maximilians-Universität München, 2005
- [68] Baltuska, A. *et al.*:  
IEEE J. Sel. Top. Quant. **9**, 972 (2003)
- [69] Oudar, J. L.; Hulin, D.; Migus, A. Antonetti, A.:  
Phys. Rev. Lett. **55**, 2074 (1985)
- [70] Taieb, R.; Veniard, V.; Marquet, A.:  
Phys. Rev. A **57**, R4098 (1998)
- [71] Siffalovic, P. *et al.*:  
Rev. Sci. Instrum. **72**, 30 (2001)
- [72] Johansson, A. *et al.*:  
Eur. Phys. J. D **22**, 3 (2003)
- [73] Ogawa, S.; Nagano, H.; Petek, H.:  
Phys. Rev. Lett. **78**, 1339 (1997)
-

- 
- [74] Siffalovic, P.; Drescher, M.; Heinzmann, U.:  
Europhys. Lett. **60**, 924 (2002)
- [75] Fuji, T. *et al.*:  
Opt. Lett. **30**, 332 (2005)
- [76] Verhoef, A. J. *et al.*:  
Opt. Lett. *submitted* (2006)
- [77] Schnürer, M. *et al.*:  
Appl. Phys. B **70**, S272 (2000)
- [78] T. A. Savas:  
(MIT Nanostructures Laboratory, Cambridge, MA, USA)  
*private communication*
- [79] Wagner, M.; Schröder, H.:  
Int. J. Mass Spectrom. Ion Processes **128**, 31 (1993)
- [80] Witzel, B.; Schröder, H.; Kaesdorf, S.:  
Int. J. Mass Spectrom. Ion Processes **172**, 229 (1998)
- [81] Witte, S.; Zinkstok, R. T.; Hogervorst, W.:  
Appl. Phys. B **78**, 37 (2004)
- [82] T. Kobayashi, T. Okada, K. A. Nelson and S. De Silvestri:  
*Ultrafast Phenomena XIV, Proceedings of the 14th International Conference, Niigata*,  
Springer, Japan, 2005
- [83] Holland, D. M. P.; Codling, K.; West, J. B.:  
J. Phys. B: At., Mol. Opt. Phys. **12**, 2465 (1979)
- [84] David R. Lide, ed.:  
*CRC Handbook of Chemistry and Physics (87th Edition)*,  
Taylor and Francis, Boca Raton, FL., 2006
- [85] Christov, Ivan P.:  
Opt. Lett. **24**, 1425 (1999)
- [86] Uiberacker, M. *et al.*:  
Nature *submitted*, (2006)
- [87] Armen, G. B.; Larkins, F. P.:  
J. Phys. B: At., Mol. Opt. Phys. **24**, 741 (1991)
- [88] Körber, H.; Mehlhorn, W.:  
Zeitschrift für Physik **191**, 217 (1966)
-

- 
- [89] Yudin, G. L.; Ivanov, M. Y.:  
Phys. Rev. A **64**, 013409 (2001)
- [90] Smirnova, O.; Spanner, M.; Ivanov, M. Y.:  
J. Phys. B: At., Mol. Opt. Phys. **B39**, S323 (2006)
- [91] Brünken, S. *et al.*:  
Phys. Rev. A **65**, 042708 (2002)
- [92] Lablanquie, P.; Morin, P.:  
J. Phys. B: At., Mol. Opt. Phys. **24**, 4349 (1991)
- [93] Mursu, J.; Jauhainen, J.; Aksela, H.:  
J. Phys. B: At., Mol. Opt. Phys. **31**, 1973 (1998)
- [94] Kikas, A. *et al.*:  
J. Electron Spectrosc. Relat. Phenom. **77**, 241 (1996)
- [95] Kitajima, M. *et al.*:  
J. Phys. B: At., Mol. Opt. Phys. **34**, 3829 (2001)
- [96] Viefhaus, J. *et al.*:  
J. Phys. B: At., Mol. Opt. Phys. **38**, 2005 (2005)
- [97] Kabachnik, N. M.:  
*private communication*
- [98] Kämmerling, B.; Krässig, B.; Schmidt, V.:  
J. Phys. B: At., Mol. Opt. Phys. **25**, 3621 (1992)
- [99] Penent, F.; Paladoux, J.; Lablanquie, P.:  
Phys. Rev. Lett. **95**, 083002 (2005)
- [100] Lablanquie, P. *et al.*:  
J. Phys. B: At., Mol. Opt. Phys. **35**, 3265 (2002)
- [101] Hayaishi, T. *et al.*:  
Phys. Rev. A **44**, R2771 (1991)
- [102] Kazansky, A. K.; Kabachnik, N. M.:  
ArXiv Physics e-prints **physics/0609242**,  
<http://arxiv.org/abs/physics/0609242> (2006)
- [103] Zerbs, J.:  
*Thesis*,  
PhD Thesis, Universität Göttingen, 2005
-

- [i01] internet source: <http://physics.nist.gov/PhysRefData/ASD/>, 2006  
NIST Atomic Spectra Database
  - [i02] internet source: <http://www.femtolasers.com>, 2006  
Compact Power Pro CEPase
  - [i03] internet source: <http://www-cxro.lbl.gov/>, 2006  
Center for X-ray optics
  - [i04] internet source: <http://www.kaesdorf.de/>, 2006  
Stefan Kaesdorf - Geräte für Forschung und Industrie
-

## CURRICULUM VITAE

---

### Curriculum vitae

Thorsten Uphues,

Date of birth: 06.05.1976

Place of birth: Verl, Germany

Nationality: German

Family status: single

#### Education

---

since 10/2003	PhD student at the <i>Department of Molecular and Surface Science,</i> Prof. Dr. U. Heinzmann, University Bielefeld, Germany
07/2003	Diploma in physics at the <i>Department of Molecular and Surface Science,</i> Prof. Dr. U. Heinzmann, University Bielefeld, Germany <i>"Adaptive fs-laserpulse shaping for optimization of High Harmonic Generation"</i>
1998 - 2003	Studies of physics at University of Bielefeld, Germany
1994 - 1998	Oberstufenkolleg an der Universität Bielefeld
1986 - 1994	Gymnasium Verl
1982 - 1986	Grundschule "Am Bühlbusch", Verl

Bielefeld, November 2006

---

---

Hiermit versichere ich an Eides statt, daß die vorliegende Arbeit bis auf die dem Aufgabensteller bekannten Hilfen selbständig angefertigt und alle benutzten Hilfsmittel unter Angabe der Literaturstellen kenntlich gemacht sind.

27. November 2006

Thorsten Uphues

---